EXPLORING SYNERGIES AT THE INTERFACE OF THE AMYLOID AND SIGNALING FIELDS

Exploring Synergies at the Interface of the Amyloid and Signaling Fields

BY NAEIMEH JAFARI, B.Sc.

A Thesis Submitted to the School of Graduate Studies in Partial Fulfilment
of the Requirements for the Degree

Doctor of Philosophy

Doctor of Philosophy (2020)	**McMaster University**
(Chemistry)	**Hamilton, Ontario**

Thesis Title: Exploring Synergies at the Interface of the Amyloid and Signaling Fields

Author: Naeimeh Jafari, B.Sc. (Shahid Beheshti University, Iran)

Supervisor: Professor Giuseppe Melacini

Number of Pages: xv, 172

Thesis Abstract

The fields of amyloid and signaling have traditionally developed through largely separate routes. However, several intersections and synergies exist between these two research areas. For example, kinase catalyzed phosphorylation is known to affect self-association in several amyloidogenic proteins. Here, we explore further instances for how methods and concepts originally pioneered in one field may benefit the other. We show how allosteric conformational transitions at the basis of signaling regulation can also serve as a basis to design sensors for binding of ligands to amyloid inhibitory chaperones. Conversely, we also illustrate how signaling benefits from the amyloid field. For example, we show that amyloid formation may serve as a non-classical mechanism for protein kinase A (PKA) activation. This is in contrast to the classical mechanism for PKA activation, which relies on cAMP-dependent conformational changes of the regulatory subunits. However, the classical cAMP-dependent activation of PKA alone may not suffice to rationalize the phenotype of enhanced PKA activation observed for known disease related mutations in the regulatory subunits of PKA, such as the Carney Complex (CNC), which is a generalized tumor predisposition. Several CNC mutants exhibit reduced affinity for cAMP, which appears incompatible with the overactivation of PKA in the context of a PKA regulation that is dependent on cAMP alone. The activation of PKA by CNC mutation-induced polymerization of inhibitory regulatory subunits and consequent amyloid formation offers a simple but effective solution to solve this apparent paradox and explain CNC phenotypes. Overall, this dissertation highlights several reciprocally beneficial opportunities at the interface between amyloids and signalling.

Acknowledgment

This thesis could never have done without the help and support of incredible people who encouraged and inspired me throughout the process. First of all, I would like to express my sincere gratitude to Dr. Giuseppe Melacini, who has been very patient and understanding with me. He kindly guided, supported, and motivated me through these years. I learned a lot from him, even beyond scientific concepts, and I much appreciate his supervision. Also, I would like to thank my supervisory committee members, Dr. Gillian Goward and Dr. Philip Britz-McKibbin, who made my committee meetings very productive with their advice, suggestions, and feedback. I also appreciate Dr. Susan S. Taylor's insight, suggestions, and discussion on my project.

Next, I would like to thank Dr. Melacini's past and present lab members, including Bryan, Stephen, Kody, Moustafa, Rajeevan, Rashik, Karla, Heba, Katherine, Yousif, Jimmy, Melanie, Maryam, Hongzhao, and Evelyn. It was an honour to know them and work beside them. I have learned from each one of them, even those that I had shortly met. I want to express my special gratitude towards Madoka. She was way more than an excellent scientist mentor; her support and company made my life in Melacini's lab very pleasurable. I also would like to thank Olivia and Jinfeng for their kind support that always touched my heart.

Moreover, I would like to thank the NMR facility staff of McMaster University, Dr. Berno, Dr. Jenkins, Megan Fair, and Dr. Kornic. Besides supporting us by taking care of the NMR facility, I am grateful that they always came to my help when I needed guidance. I would also like to thank McMaster's electron microscopy facility staff, especially Marcia, who trained me and kindly supported me. I am also very grateful to the Biointerface Institute staff, especially Marta, and the staff of the Centre for Microbial Chemical Biology, particularly Susan. Finally, I

would like to thank the Mobix lab staff, which I have never met in person, but I always benefited from their work.

Most importantly, thanks to my Family. I am deeply thankful to my parents, Akram Taherian and Mojtaba Jafari. Their unlimited love and support from the overseas felt very close, warmed me, and lighted my way. Also, I would like to thank my brothers, Mohammad and Hamed, for their heartwarming support and thoughtful advice. I want to thank my nephew, Mohammad Hossain, and my niece, Narges, who patiently cope with the long-distance relationship. I want to thank my husband, Adel Hashemi. His everyday love, company, and support are blessings of my life. He knows the best way to encourage me and cheer me up in difficulty. And above all, many thanks to Noora, my lovely daughter. Her patience and cooperation are beyond her age's expectations. Noora has been my constant source of energy, hope, love, and happiness. Without her warm hugs and cheerful character, I cannot imagine how I would cope with the many difficulties and obstacles of studies and research.

Table of Contents

List of Main Figures

List of Supplementary Figures

List of Tables

List of Abbreviations

(trimethylsilyl)trifluoroacetamide (MSTFA)

^{13}C-Oleic acid for the NMR-based assessment of albumin-bound LCFA concentration (CONFA)

3',5'-cyclic adenosine monophosphate (cAMP)

3',5'-cyclic guanosine monophosphate (cGMP)

8-anilinonaphthalene-1-sulfonate (ANS)

Acrodysostosis (ACRO)

Acrodysostosis type 1 (ACRDYS1)

adenosine triphosphate (ATP)

Albumin-cobalt-binding (ACB)

Alpha synuclein (αS)

Alzheimer’s disease (AD)

Amyloid beta (Aβ)

Aβ oligomers ($A\beta_n$)

Bovine serum albumin (BSA)

cAMP-binding domain (CBD)

chemical shift covariance analysis (CHESCA)

Compounded chemical shift (CCS)

Corney complex (CNC)

cyclic nucleotide monophosphate (cNMP)

Dansyl phenylalanine (Dan F)

Dimeric R1α (R_2)

Dimethyl sulfoxide (DMSO)

Disease related mutation (DRM)

Dithiothreitol (DTT)

Dynamic light scattering (DLS)

ensemble of unfolded and partially unfolded states of R (U)

Exchange protein directly activated by cAMP (EPAC)

Fatty acid (FA)

Fatty acid and globulin free human serum albumin (rHSA)

Folded native structure (F)

Generic G-protein coupled receptor (GPCR)

Globulin free human serum albumin (gHSA)

Glycated HSA (glyHSA)

Heteronuclear single quantum coherence (HSQC)

human PKG (hPKG)

Human serum albumin (HSA)

hydrogen/deuterium exchange (HDX)

Hyperpolarization-activated cyclic nucleotide-gated channel (HCN)

Ischemia-modified albumin (IMA)

Linoleic acid (LA)

liquid-liquid phase separation (LLPS)

Long-chain fatty acid (LCFA)

Molecular weight (MW)

Myristic acid (MA)

Nuclear Magnetic Resonance (NMR)

Octanoic acid (C8)

Oleic acid (OA)

Parkinson’s disease (PD)

Phosphate binding cassette (PBC)

Phosphodiesterase (PDE)

PKA catalytic subunit (C)

PKA regulatory subunit (R)

PKA regulatory subunit R1α (R1α)

Polymerized R1α (R_n)

Protein Kinase A (PKA)

Root mean square deviation (RMSD)

Size exclusion chromatography (SEC)

Size exclusion chromatography coupled with multi-angle light scattering (SEC-MALS)

Thioflavin T (ThT)

Transmission electron microscopy (TEM)

α-linoleic acid (α-LA)

Chapter 1 Introduction

1.1.1 Introduction

This thesis explores the interface between the amyloid and signaling fields. These two areas of research have traditionally developed quite independently of each other. However, here we show that multiple synergies are starting to emerge between approaches and concepts developed for understanding amyloids that are useful and novel in the signaling field and vice-versa. In order to illustrate such synergies, we will first review recent contributions to both fields from our group and we will then provide an outline of specific examples for the constructive ‘cross-talk’ between the two fields, which is the focus of this dissertation. Such examples have arisen primarily from the amyloid and signaling research programs ongoing in our own laboratory. This is why the relevant review of these fields presented here does not claim to be exhaustive and centers mainly on the work from our laboratory. Specifically, within the amyloid field, we are interested in understanding how plasma proteins, such as human serum albumin (HSA), functions as extracellular chaperone and inhibits amyloid plaque formation. Within the signaling field, our primary interest is on the cyclic-AMP (cAMP) second messenger and how it controls downstream receptors, including Protein Kinase A. In this thesis we will show how these two apparently distinct fields have more in common than previously anticipated.

1.2 Recent Advances on the Interactions of Plasma Proteins with Amyloidogenic Peptides

Plasma proteins serve as carriers of serum solutes, and as extracellular chaperones (1–6). Protein homeostasis in plasma is maintained by plasma's chaperones since plasma proteins bind selectively to unfolded polypeptides and prevent them from further growth and aggregation (1, 6). Human serum albumin (HSA) is one of the main extracellular chaperones. HSA serves as the main ligand carrier and also as inhibitor of polypeptide self-association that leads to cytotoxic oligomers, such as those formed by the amyloidogenic Aβ peptide (1–5). The molecular mechanisms underlying plasma proteins chaperone function have been studied in our group and our Progress on this field is reported here.

Capitalizing on Nuclear Magnetic Resonance (NMR) approaches pioneered in our laboratory (7–10), we have mapped with single-residue resolution the self-association of the Aβ peptide and have probed how Aβ interacts with amyloid inhibiting proteins, such HSA (10–16). Specifically, we have shown how to exploit the dynamic nature of the monomer *vs*. oligomer equilibrium to indirectly observe the NMR-invisible ('dark') oligomers through the NMR-visible monomers (7–10). This NMR approach was then combined with fluorescence, dynamic light scattering (DLS) and electron microscopy (EM) to reveal that HSA selectively binds to oligomeric Aβ ($A\beta_n$) rather than monomeric Aβ ($A\beta_1$) and that HSA and $A\beta_1$ compete for overlapping binding sites within $A\beta_n$ (11, 12, 15). We then determined the stoichiometries and affinities of the $A\beta_n$ – HSA complexes through the comparative analysis of domain deletion mutants of recombinant HSA, for which the amyloid inhibitory potencies (IC_{50}) were quantified by NMR using a Scatchard-like model (12). We showed that, while only a single HSA molecule is bound per Aβ oligomer, multiple binding sites with sub-mM affinities for $A\beta_n$ are present in HSA and are evenly partitioned across the three albumin domains (12). More recently, we have been able to localize one of the binding loci for high molecular weight (MW) $A\beta_n$ to a 20-residue peptide spanning a flexible loop of HSA with partial sequence homology to Aβ (14).

Our $A\beta_n$ – HSA model rationalizes how HSA inhibits the growth of Aβ oligomers into mature fibrils and represents an *unexpected paradigm shift* relative to earlier hypotheses in the field positing that the amyloid inhibitory function of HSA was due to direct binding of Aβ monomers (17). We subsequently found that other proteins with anti-amyloid function, such as the plasma protein transferrin, conform to the new monomer competition paradigm we proposed originally for HSA (13), proving that HSA serves as a general prototype of aggregation inhibition by extracellular chaperones. This finding was particularly significant because transferrin was previously thought to inhibit amyloid formation only through iron sequestration. Our work was the *first* to demonstrate that transferrin inhibits self-association also through an iron-independent mechanism (13). Furthermore, the NMR-based experimental strategy we proposed for the Aβ - HSA interactions was applied to other systems (18–22) and, given its unique reproducibility, it was adopted as a standard to measure the amyloid inhibitory potency of industrial albumin preparations (16). Overall, our work proves the efficacy of comparative NMR analyses to map otherwise elusive interactions with high MW species (*e.g.* $A\beta_n$).

Taking advantage of similar NMR approaches (7–10, 23, 24), we also mapped with single-residue resolution how the amyloidogenic Aβ interacts not only with HSA but also with another plasma amyloid inhibitor, *i.e.* epigallocatechin gallate (EGCG) (13, 14, 16, 23, 25–27). Specifically, we combined NMR methods sensitive to monomer *vs*. oligomer equilibria with fluorescence, dynamic light scattering (DLS) and electron microscopy (EM) to show that both HSA and EGCG bind to oligomeric Aβ ($A\beta_n$) with higher affinity than monomeric Aβ ($A\beta_1$), that they coat $A\beta_n$, and inhibit its recognition by $A\beta_1$ (23–26). We then discovered that the $A\beta_n$ *vs.* $A\beta_1$ selectivity of HSA is more pronounced for Aβ(1-42) than Aβ(1-40), the two main Aβ isoforms. This unexpected finding is due to transient intra-molecular contacts in Aβ(1-42) that shield it from inter-molecular interactions with HSA (23, 26). We also established that the weak $A\beta_1$ – HSA binding is physiologically relevant in plasma, where the HSA concentration is high (~0.6 mM) (23). However, in the cerebrospinal fluid (CSF), where HSA is dilute (~μM), only the $A\beta_n$ – HSA binding is relevant. We also localized a key binding site for $A\beta_n$ to a flexible HSA loop that is allosterically dependent on fatty acid saturation (14, 24). Overall, our Aβ – HSA model rationalizes how HSA inhibits the growth of Aβ oligomers into mature fibrils and represents an *unexpected paradigm shift* relative to earlier hypotheses positing that the amyloid inhibitory function of HSA was due only to Aβ monomer binding (17).

Within this context, this dissertation aims at addressing outstanding fundamental questions on how the function of prototypical plasma proteins is controlled by their native physiological environment through modulations of dynamics. Addressing these questions is essential to: (a) understand the *in vivo* functional response to a plethora of mutations and post-translational modifications, *e.g.* oxidation, phosphorylation, nitration, glycation and acetylation; (b) design new technologies for industrial plasma fractionation and formulation; (c) develop new blood-based assays. Specially, a key goal of this thesis is to develop methods to establish the fatty acid content of HSA. Fatty acids (FAs) bound to HSA are a key determinant of the HSA inhibitory potency (14, 24), but traditional methods to establish FA content in HSA are rather indirect as they rely on chemical extraction as well as gas chromatography coupled with mass spectrometry. We sought to develop spectroscopy methods to assess the amount of long chain FA bound to HSA without the need of chemical extraction. To this end, we took advantage of concepts initially mastered in context of signalling projects, such allosteric conformational switch and how they can serve as effective ligand binding sensors. Hence, in the next sections we will review our recent advances in the field of cyclic nucleotide monophosphate (cNMP) signaling and we will outline how such advancements proved an effective means to assess the saturation of HSA by FAs.

1.3 Recent Advances on the Allosteric Mechanisms Regulating cNMP-Dependent Signaling

1.3.1 General Background on cAMP

Extracellular stimuli are transduced into controlled intracellular responses in order to enable cell-to-cell communication. For this purpose, external signals are relayed by second messengers, including cAMP.* cAMP acts by binding to regulatory proteins and causing conformational changes that modulate specific cellular functions, but the conformational switches controlled by cAMP are only partially understood despite their critical relevance for the treatment of cardiovascular, hormonal and neuronal disorders (28–31). Increased intracellular cAMP concentrations are generated in response to hormones stimulating numerous G-protein-coupled receptors that activate adenylyl cyclase (28–30)(Fig. 1.1). In mammals, a pivotal receptor for cAMP is the archetypical cAMP-dependent protein kinase (PKA) (28). However, cAMP also functions independently of PKA by activating two other major and more recently discovered cAMP-receptors, *i.e.* the hyperpolarization-activated and cyclic nucleotide-gated ion channels (HCN), which generate cardiac and neuronal electrical rhythmicity (32), and the exchange protein activated by cAMP (EPAC) (30, 32, 33), which is a guanine-nucleotide-exchange factor (Fig. 1.1). PKA,

---

***Abbreviations*: C – catalytic subunit of PKA; cAMP – 3'5' cyclic ester of adenosine monophosphate; cAMPS – phosphorothioate cAMP analog; CBD – cAMP-binding domain; cGMP – cyclic guanosine 5'-monophosphate; EPAC – exchange protein activated by cAMP; HCN – hyperpolarization-activated and cyclic nucleotide-gated channels; H/D – hydrogen/deuterium exchange; H/H – hydrogen/hydrogen exchange; HSQC – heteronuclear single-quantum coherence spectrum; IR – intracellular region; NTHB – N-terminal helical bundle; PBC - phosphate binding cassette; PKA - cAMP-dependent protein kinase; PRE – paramagnetic relaxation enhancement; R – regulatory subunit of PKA; RIα – R type Iα.

HCN and EPAC mediate the majority of cAMP responses (31, 34) and regulate multiple cellular processes ranging from ion-channel gating to cell growth and adhesion (Fig. 1.1) (30–32, 35).

1.3.2 Medical Relevance

PKA Is a Cancer Driver. Under physiological resting conditions the PKA catalytic subunit (C) is inhibited by the PKA regulatory subunit (R) (28). When this inhibition is impaired, multiple tumours are observed (36–39). For example, deletion of the gene for the isoform 1a of the R-subunit (R1α) causes PKA over-activation and a wide spectrum of neoplasias, including breast cancer, osteosarcomas, pancreatic, pituitary and thyroid tumours (36–43). In addition, PKA R1α down-regulation in cancer patients enhances the resistance of cancer cells to glucose starvation and correlates with tumour progression and poor clinical prognosis (36, 37, 40). The onco-genomic and onco-proteomic evidence indicates that PKA R1α is an essential tumour suppressor in multiple tissues (36–40).

PKA Disease-Related Mutations (DRMs). Inherited autosomal dominant R1α mutations that impair PKA inhibition cause a cancer predisposition condition known as Carney complex (CNC) (38, 44–49). CNC leads to pancreatic, endocrine and cardiac tumours (38, 44–49). In addition, R1α mutations that decrease the sensitivity of PKA R1α to cAMP lead to acrodysostosis (ACRDYS1), a severe pediatric syndrome associated with hormone resistance, intellectual disability and abnormal bone growth (50–52).

Role of cAMP in Cardiovascular Physiology and Pathology. cAMP plays a key role in the chain of reactions by which the β-adrenergic agonists affect the rate of the heart beat (29, 53, 54). Cardiac pacemaker activity is controlled by the intracellular Ca^{2+} clock and the surface membrane voltage clock (55). PKA is a key regulator of the former, while HCN is part of the latter. For instance, the cAMP-mediated activation of PKA by epinephrine results in the phosphorylation of troponin-I, which alters the cardiac relaxation, and of phospholamban (PLB), which shortens the contraction period (29, 56–58). However, cAMP also binds to HCN, promoting the opening of these channels and accelerating the cardiac rhythm (32). Incorrect cAMP signal translation by PKA has been linked to acute ischemic stress and cardiac tumors (59–61), while several HCN mutations are known to cause arrhythmias (31, 62, 63).

HCN as a Drug Target for Arrhythmias and Neuronal Disorders**.** HCN is the target of ivabradine, a clinically approved drug for the treatment of angina pectoris (31, 64). In addition, given the key role of HCN in neuronal excitability, HCN is an ideal target also for anticonvulsant and analgesic drugs (31). A promising avenue to selectively target HCN relies on allosteric modulators that bind to the cAMP-binding domain (CBD) of HCN, *e.g.* cAMP analogs acting as *HCN-selective agonists are drug leads for bradycardia and epilepsy caused by HCN mutations favoring channel closure* (31, 62, 65–67).

Allosteric Kinase Inhibition. Allosteric modulation is a promising approach also for selective kinase inhibition (66). Kinase inhibitors are effective anti-cancer agents (*e.g.* Gleevec) (68), but they are typically poorly selective (68). For instance, the competitive inhibitor H89, which binds directly the highly conserved catalytic site of PKA, inhibits several other kinases causing multiple side-effects that are absent when PKA inhibition is obtained through allosteric inhibitors (69). These include cAMP analogs that target more selectively less conserved sites of PKA, such as the CBDs (68). As a result, hundreds of cAMP analogs have been screened for PKA antagonism (70), but to date the only known cAMP antagonist in PKA is Rp-cAMPS (or Rp). *Hence, it is essential to understand the mechanism of action of Rp, which does not bind the PKA catalytic* *subunit (C) but only the C-bound regulatory subunit (R).*

The elucidation of the molecular basis for disorders that range from cardiac tumors and arrhythmias to epilepsy requires the full clarification at a structural and dynamical level of how the cAMP signal is translated by HCN, PKA and EPAC. Each protein alone would not be able to fully account for the complex regulatory effects of cAMP. Our laboratory has focused on PKA, EPAC and HCN (Fig. 1.1) for the purpose of developing comprehensive models of cAMP-dependent allosteric activation, agonism and antagonism. The comparative analysis of these molecular mechanisms in PKA, EPAC and HCN is required for the development of selective CBD effectors that may serve as drug leads for the treatment of cardiovascular, metabolic and neurological diseases.

Despite the clinical relevance of cAMP-signaling, the molecular basis of pathological cNMP-signaling and of therapeutic inhibition of the cNMP-signal are poorly understood. Hence, a key long-term goal is to understand the structural and dynamical mechanisms for the CNC- and ACRDYS1-causing mutations in PKA R1α and for the allosteric inhibition of the PKA (36, 39, 40, 71–74). Deciphering the molecular basis of PKA DRMs and elucidating the mechanisms of action of cNMP analogs that function as allosteric inhibitors of PKA is essential to fully exploit the translational potential of cNMP-signaling (71–74). In the next sections we will review our progress towards this long-term goal.

1.3.3. Allosteric Regulation of Eukaryotic cAMP-Binding Domains

<u>Dynamically Driven Allostery and Cyclic Nucleotide Selectivity in EPAC</u>. We have focused on the EPAC1 CBD with the goal of understanding the structural and dynamical basis of

allostery in this domain. We have met this aim by developing an NMR-based model positing that when cAMP docks in the phosphate binding cassette (PBC), the remote N-terminal helical bundle (NTHB), which mediates critical inhibitory interactions, experiences a major enhancement of ps-ns and ms-ms dynamics without significant structural changes. As a result, cAMP introduces an entropic penalty and weakens the inhibitory interactions mediated by the NTHB ("*dynamically driven allostery or DDA"*) (75–80). We have also shown that DDA is a key determinant of cAMP *vs.* cGMP selectivity (81). While EPAC selects the *syn* conformation of cAMP, EPAC binds cGMP in an *anti* conformation (81). As a result of this *syn*-to-*anti* transition, cGMP does not elicit the NTHB dynamic enhancement and functions as an antagonist (81).

Mapping the EPAC Allosteric Networks. Another key question we addressed pertains to the allosteric networks underlying the changes in structure and dynamics that control EPAC function. The comparative analysis of structure and dynamics in the apo and allosteric effector-bound states often reveals only the start and end points of an allosteric network, but not the other critical sites that relay a signal from the binding pocket to distal functional loci. To address this problem we have proposed a general NMR method based on the CHEmical Shift Covariance Analysis (CHESCA) (82). Chemical shifts are exquisite probes of dynamics and linear inter-residue chemical shift correlations reflect concerted responses to a common set of perturbations (82–84). When such perturbations include cAMP analogs that modulate the activation equilibrium, CHESCA provides a residue-specific dissection of binding *vs.* allosteric contributions and identifies otherwise elusive allosteric networks (82–84). Similar analyses are useful for evaluating how mutations perturb the activation equilibria (83–86).

Dynamically Driven Ion Channel Gating in HCN. HCN drives the cNMP-dependent pacemaker activity in the heart, and its malfunction causes arrhythmias. For example, the S672R mutation in the HCN CBD results in familial sinus bradycardia (87). We determined the mechanism for both the pacemaker activity of HCN (88) and the bradycardia mutation (86). Despite intense competition, we solved the first structure of the apo HCN CBD (88) and showed that it modulates HCN ion channel opening by destabilizing a tetrameric gating ring (88–91). We also showed that HCN dynamics shapes the free-energy landscape of HCN activation by gating cAMP binding and by enabling the pre-sampling of activation competent states prior to cAMP binding (88–90). Finally, our NMR analyses revealed that, although no appreciable differences are observed between the wt and S672R structures, S672R causes faster cAMP off rates and a constitutive shift of the auto-inhibitory equilibria towards inactive states, explaining the molecular basis of bradycardia (86).

Unique Features of HCN Allostery. Another key result was that the allosteric networks of HCN are markedly distinct from those of the homologous CBD of another human cAMP receptor, i.e. the exchange protein activated by cAMP (EPAC; Fig. 1.1) (85, 88–96). For example, the C-terminal lid is indispensable for HCN activation, but dispensable in EPAC (88, 89, 96). These differences are critical to selectively target specific eukaryotic CBDs and were identified utilizing the chemical shift covariance analysis (CHESCA) (82) and related methods (84, 85, 94, 96, 97) developed by us to map allostery through NMR chemical shifts. Chemical shifts are exquisite probes of dynamics and linear inter-residue chemical shift correlations reflect concerted responses to a common set of perturbations (82). When such a perturbation set is a small targeted library of cNMP analogs or mutations that modulate the activation equilibrium, CHESCA provides a new way to dissect residue-specific contributions to binding and allostery, identifying otherwise elusive functional allosteric networks (82, 84, 98). There examples illustrate of how dynamics mapped at atomic resolution are critical to dissect the mechanisms of action of allosteric inhibitors and disease-related mutations. Similar approaches can be extended to PKA.

The PKA System. In the PKA holoenzyme, two catalytic subunit (C) molecules are bound to a dimeric regulatory subunit (R_2) (Fig. 1.2). Upon binding to cAMP, each R-subunit undergoes a conformational change, releasing the C-subunit that phosphorylates target proteins (Fig. 1.2) (99, 100). The R-subunit is composed of an N-terminal dimerization/docking domain, followed by a linker that includes an auto-inhibitory segment and is C-terminally connected to two tandem CBDs (CBD-A and B, Fig. 1.2b) (101). While CBD-B regulates the access of cAMP to CBD-A, the linker and CBD-A mediate the key inhibitory interactions with C (101–104). When C-bound, CBD-A adopts the 'H' conformation (*i.e.* Fig. 1.3b, but switches to the 'B' state when cAMP-bound (Fig. 1.3c) (70, 102).

Our Previous Work on PKA. We focused on the structural basis of cAMP-dependent allostery in the globular CBDs of PKA in the absence of the linker and C. As explained in our publications (105–109), we have met this aim by formulating an atomistic three-shell allosteric model for the activation of PKA, revealing a cAMP-dependent signaling pathway (i.e. R209-D170-R226) (106, 108, 109) that is obligatory for CBD-A but is not conserved in CBD-B (105) or in EPAC (110). One of the most notable PKA *vs.* EPAC differences is in the N-terminal a-subdomain, which mediates critical inhibitory interactions in both systems, but undergoes a dramatic cAMP-dependent conformational change only in PKA (Fig. 1.3a)(76). These results highlight how seemingly subtle differences in sequence and structure among CBDs can result in major variations in the allosteric mechanisms through which cAMP controls enzymatic activity in eukaryotes.

We also have shown that the apo CBDs of PKA, unlike those of EPAC and HCN, sample comparable populations of non-inhibitory and inhibitory states, explaining the high (nM) affinity of the R-subunit for cAMP (97, 111). We also showed that cAMP activates PKA through a double-conformational selection mechanism, in which cAMP couples intra- and inter-CBD dynamics by controlling not only the ON/OFF equilibria in each CBD, but also the relative CBD orientation (Fig. 1.4) (112). To understand the cross-talk between cAMP and cGMP-signaling pathways, we extended our PKA studies to the close homolog human PKG (hPKG) and showed that cAMP acts as a partial agonist for hPKG by stabilizing a mixed CBD state with N- and C-terminal helices in ON and OFF conformations, respectively (113). These results highlight how even seemingly subtle differences in sequence and structure among CBDs can result in major variations in the allosteric mechanisms through which cNMPs control enzymatic activity. However, the molecular basis for allosteric PKA antagonism and for the CNC- and ACRDYS1-disease related mutations in PKA R1α is at present only poorly understood.

1.3.4. Open Questions about Disease Related PKA R1a Mutants.

Understanding allosteric regulation of PKA R1α is necessary also to rationalize PKA R1α mutations linked to CNC and ACRDYS1 diseases (38, 44–52). CNC and ACRDYS1 exhibit opposite molecular phenotypes (46, 47, 50, 51). CNC is caused by gain-of-function R1α mutations that enhance PKA activation (46, 47), while ACRDYS1 is linked to loss-of-function R1α mutations that impair the ability of cAMP to activate PKA (Fig. 1.5) (50–52). To date 8 CNC- and 14 ACRDYS1-related PKA R1α mutations (Fig. 1.6) are known to produce functionally impaired R1α protein (38, 44–52). However, the underlying mechanisms are still elusive.

Most CNC mutations are confined to CBD-A (Fig. 1.6a) and, although not at the inhibitory C:R interface, they have been hypothesized to weaken the C:R complex and promote PKA activation by modulating the inhibitory allosteric equilibria of R (47, 51). For example, MD simulations suggest that the CNC mutant A211D rewires the regulatory networks of PKA R1α by mimicking the cAMP phosphate and forming a salt bridge with the allosteric hub residue R209 (51). This stabilizes the ON state of CBD-A and facilitates PKA activation (51). Similarly, other CNC mutations result in PKA activation at lower cAMP concentrations than wt (Fig. 1.5a), consistent with a constitutive CBD-A shift to the ON state (47). Allosteric alterations are critical also to rationalize the resistance to cAMP activation observed for ACRDYS1 mutations (Fig. 1.5b), which are located primarily in CBD-B (Fig. 1.6b) (50–52). The ACRDYS1 vs. wt cAMP resistance may arise either from cAMP-affinity losses and/or from disruptions in the cAMP-dependent allosteric networks of R. An example of the latter scenario is provided by the ACRDYS1 R1α(R366X) nonsense mutant (52). The R366X and wt R1α:C crystal structures are virtually identical (RMSD = 0.6 Å), but significant R366X *vs.* wt losses in electron density are observed far from the mutation site, pointing to long-range enhancements in dynamics affecting inter-CBD communication networks (52). Similarly, another ACRDYS1 mutant, G287E in CBD-B (Fig. 1.6b), results in long-range perturbations in CBD-A that reduce its cAMP-affinity (51).

In summary, we hypothesize that: (a) gains of kinase function in CNC mutants are due to constitutive shifts of the regulatory CBD equilibria towards states with compromised C-inhibition competence, including the ON conformation and/or other states structurally and/or dynamically distinct from the OFF state; (b) losses of kinase function in ACRDYS1 mutants arise not only from reduced cAMP-affinities, but also from alterations in the cAMP-dependent regulation of the R-subunit, including (i) constitutive shifts of CBD equilibria to OFF states; (ii) compromised couplings between the ON/OFF equilibria of CBD-A and -B or between the ON/OFF equilibrium of each CBD and cAMP-binding. These hypotheses address long outstanding questions on CNC and ACRDYS1 diseases and this thesis represent a first steps towards testing them. Once we reveal the molecular mechanisms underlying genetic mutations linked to CNC and ACRDYS1 diseases, we will be in a unique position to fully exploit the translational potential of cNMP-signaling. The comparative analysis of cAMP-allostery and antagonism in PKA vs. other eukaryotic cAMP receptors we investigated previously (HCN and EPAC) will enable the design of highly selective PKA inhibitors with major potential as leads for drugs against a wide spectrum of cancers.

1.4 Thesis Outlook

As mentioned in section 1.1, this thesis explores the interface between the amyloid inhibition and the cAMP-allostery fields. Although apparently divergent, these two areas of research offer several opportunities for constructive ‘cross-contamination’. The overarching goal of this dissertation is to explore such synergies. Specifically, chapter two shows how methods and concepts originally developed to understand allosteric conformational switches are also useful to gauge the long-chain FA-content of the most potent plasma amyloid inhibitor, HSA. The extent of HSA saturation by FA is a critical modulator of the HSA potency as amyloid inhibitor. Hence, this is a clear example illustrating how transfer of signalling allosteric concepts to the amyloid field is beneficial. The inverse transfer is also a very productive exercise, as shown in chapters three and four.

In chapter three we articulate how importing concepts from the amyloid field can resolve an apparent paradox about CNC related mutations. Such mutations are primarily located in CBD-A, which is essential for PKA C inhibition, and typically result in cAMP-affinity losses. Such decreased binding is challenging to reconcile with the increase PKA activation phenotype of CNC, if these results are interpreted within the context of the classical cAMP-dependent allostery. However, this apparent paradox can be easily solved if we hypothesize that CNC mutations cause misfolding and aggregation and we assume such polymeric aggregates are PKA inhibition incompetent. In chapter three, we test this hypothesis focusing on the A211D PKA R1α CNC mutant as well as the cognate A211T ACRDYS1 mutant as an internal term of comparison devoid of positional bias. As expected, the extent of unfolding and aggregation increases in the order A211D > A211T > WT, providing an initial confirmation of our amyloid based hypotheses on the overactivation of CNC mutants.

In chapter four, we show that a similar pattern is observed for the G287W PKA R1α CNC mutant and its G287E ACRDYS1 counterpart, providing further corroboration to the proposed CNC mechanism of PKA activation by polymerization-induced losses of inhibitory PKA R1α function. The investigation of the CNC PKA R1α mutants in chapters three and four clearly illustrates the benefits of importing concepts from the amyloid field into the signaling arena. In the concluding chapter (five), we further discuss the implications of such synergies arising at the interface between the amyloid and signaling research areas.

1.5 Other Milestones at the Signaling – Amyloid Interface

The work presented in this thesis is part of a developing field aimed at exploring the cAMP-signaling – amyloid interface. Here, we will briefly review previous milestones in this interdisciplinary research area. Aβ (1-42), whose aggregated deposits are one of the hallmarks of Alzheimer's disease, modifies the PKA activity (114) and PKA activation causes synaptic resistance to Aβ (115). Furthermore, PDE4 inhibitors improve memory, long term potentiation (LTP), and contextual learning (114, 115). Also, traumatic brain injury (TBI), which is characterized by external sedimentation of β-amyloid precursor protein, leads to changes in the cAMP signaling pathway (116). Another example of the interplay between cAMP-dependent signaling and neurosciences comes from neurofibrillary tangles formed by the hyperphosphorylated tau protein, which is another hallmark of AD. The hyperphosphorylation of tau protein is catalyzed by multiple kinases, including PKA, glycogen synthase kinase (GSK-3), cyclin dependant kinase 5 (Cdk-5), MAPK family members, casein kinase, calcium calmodulin dependant kinase II (CaMK-II), microtubule affinity regulating kinase (MARK), and others (117). Taken together, these examples show both the pathophysiological significance of focusing on the cAMP-signaling – amyloid interface as well as its multifaceted and complex nature. While it is virtually impossible to fully recapitulate such complexity in a single doctoral dissertation, here we try to show how *in vitro* biophysical experiments can reveal new aspects of the synergetic and reciprocal relationships between the signaling and amyloid fields.

1.6 References

1. T. E. Finn, A. C. Nunez, M. Sunde, S. B. Easterbrook-Smith, Serum albumin prevents protein aggregation and amyloid formation and retains chaperone-like activity in the presence of physiological ligands. *J. Biol. Chem.* **287**, 21530–21540 (2012).
2. A. L. Biere, *et al.*, Amyloid β-peptide is transported on lipoproteins and albumin in human plasma. *J. Biol. Chem.* **271**, 32916–32922 (1996).
3. B. Bohrmann, *et al.*, Endogenous proteins controlling amyloid β-peptide polymerization possible implications for β-amyloid formation in the central nervous system and in peripheral tissues. *J. Biol. Chem.* **274**, 15990–15995 (1999).
4. T. Kugimiya, *et al.*, Loss of functional albumin triggers acceleration of transthyretin amyloid fibril formation in familial amyloidotic polyneuropathy. *Lab. Investig.* **91**, 1219–1228 (2011).
5. C. J. Rosenthal, E. C. Franklin, Serum amyloid A (SAA) protein—interaction with itself and serum albumin. *J. Immunol.* **119**, 630–634 (1977).
6. A. R. Wyatt, J. J. Yerbury, R. A. Dabbs, M. R. Wilson, Roles of extracellular chaperones in amyloidosis. *J. Mol. Biol.* **421**, 499–516 (2012).
7. J. Milojevic, V. Esposito, R. Das, G. Melacini, Understanding the molecular basis for the inhibition of the Alzheimer's Aβ-peptide oligomerization by human serum albumin using saturation transfer difference and off-resonance relaxation NMR spectroscopy. *J. Am. Chem. Soc.* **129**, 4282–4290 (2007).
8. V. Esposito, R. Das, G. Melacini, Mapping polypeptide self-recognition through 1H off-resonance relaxation. *J. Am. Chem. Soc.* **127**, 9358–9359 (2005).
9. J. Milojevic, V. Esposito, R. Das, G. Melacini, Analysis and parametric optimization of 1H off-resonance relaxation NMR experiments designed to map polypeptide self-recognition and other noncovalent interactions. *J. Phys. Chem. B* **110**, 20664–20670 (2006).
10. H. Huang, J. Milojevic, G. Melacini, Analysis and optimization of saturation transfer difference NMR experiments designed to map early self-association events in amyloidogenic peptides. *J. Phys. Chem. B* **112**, 5795–5802 (2008).
11. J. Milojevic, A. Raditsis, G. Melacini, Human serum albumin inhibits Aβ fibrillization through a "monomer-competitor" mechanism. *Biophys. J.* **97**, 2585–2594 (2009).
12. J. Milojevic, G. Melacini, Stoichiometry and affinity of the human serum albumin-Alzheimer's Aβ peptide interactions. *Biophys. J.* **100**, 183–192 (2011).
13. A. V Raditsis, J. Milojevic, G. Melacini, Aβ association inhibition by transferrin. *Biophys. J.* **105**, 473–480 (2013).
14. M. Algamal, J. Milojevic, N. Jafari, W. Zhang, G. Melacini, Mapping the Interactions between the Alzheimer's Aβ-peptide and human serum albumin beyond domain resolution. *Biophys. J.* **105**, 1700–1709 (2013).

15. J. Kooistra, J. Milojevic, G. Melacini, J. Ortega, A new function of human HtrA2 as an amyloid-β oligomerization inhibitor. *J. Alzheimer's Dis.* **17**, 281–294 (2009).

16. J. Milojevic, M. Costa, A. M. Ortiz, J. I. Jorquera, G. Melacini, In vitro amyloid-β binding and inhibition of amyloid-β self-association by therapeutic albumin. *J. Alzheimer's Dis.* **38**, 753–765 (2014).

17. Y.-M. Kuo, *et al.*, Amyloid-β peptides interact with plasma proteins and erythrocytes: implications for their quantitation in plasma. *Biochem. Biophys. Res. Commun.* **268**, 750–756 (2000).

18. K. Hasegawa, D. Ozawa, T. Ookoshi, H. Naiki, Surface-bound basement membrane components accelerate amyloid-β peptide nucleation in air-free wells: An in vitro model of cerebral amyloid angiopathy. *Biochim. Biophys. Acta (BBA)-Proteins Proteomics* **1834**, 1624–1631 (2013).

19. K. Ono, *et al.*, Phenolic compounds prevent amyloid β-protein oligomerization and synaptic dysfunction by site-specific binding. *J. Biol. Chem.* **287**, 14631–14643 (2012).

20. Y. Liang, M. O. Ore, S. Morin, D. J. Wilson, Specific Disruption of Transthyretin (105–115) Fibrilization Using "Stabilizing" Inhibitors of Transthyretin Amyloidogenesis. *Biochemistry* **51**, 3523–3530 (2012).

21. S. Laurent, M. R. Ejtehadi, M. Rezaei, P. G. Kehoe, M. Mahmoudi, Interdisciplinary challenges and promising theranostic effects of nanoscience in Alzheimer's disease. *RSC Adv.* **2**, 5008–5033 (2012).

22. S. Il Yoo, *et al.*, Inhibition of amyloid peptide fibrillation by inorganic nanoparticles: functional similarities with proteins. *Angew. Chemie Int. Ed.* **50**, 5110–5115 (2011).

23. R. Ahmed, G. Melacini, A solution NMR toolset to probe the molecular mechanisms of amyloid inhibitors. *Chem. Commun.* **54**, 4644–4652 (2018).

24. B. VanSchouwen, R. Ahmed, J. Milojevic, G. Melacini, Functional dynamics in cyclic nucleotide signaling and amyloid inhibition. *Biochim. Biophys. Acta (BBA)-Proteins Proteomics* **1865**, 1529–1543 (2017).

25. R. Ahmed, *et al.*, Molecular mechanism for the (−)-epigallocatechin gallate-induced toxic to nontoxic remodeling of Aβ oligomers. *J. Am. Chem. Soc.* **139**, 13720–13734 (2017).

26. M. Algamal, *et al.*, Atomic-resolution map of the interactions between an amyloid inhibitor protein and amyloid β (Aβ) peptides in the monomer and protofibril states. *J. Biol. Chem.* **292**, 17158–17168 (2017).

27. N. Jafari, *et al.*, Allosteric sensing of fatty acid binding by NMR: Application to human serum albumin. *J. Med. Chem.* **59**, 7457–7465 (2016).

28. E. G. Krebs, Protein phosphorylation and cellular regulation I. *Biosci. Rep.* **13**, 127–142 (1993).

29. J. R. Levick, *An introduction to cardiovascular physiology* (Butterworth-Heinemann, 1995).

30. J. L. Bos, Epac proteins: multi-purpose cAMP targets. *Trends Biochem. Sci.* **31**, 680–686 (2006).

31. O. Postea, M. Biel, Exploring HCN channels as novel drug targets. *Nat. Rev. Drug Discov.* **10**,

903–914 (2011).

32. B. J. Wainger, M. DeGennaro, B. Santoro, S. A. Siegelbaum, G. R. Tibbs, Molecular mechanism of cAMP modulation of HCN pacemaker channels. *Nature* **411**, 805–810 (2001).
33. J. De Rooij, *et al.*, Epac is a Rap1 guanine-nucleotide-exchange factor directly activated by cyclic AMP. *Nature* **396**, 474–477 (1998).
34. I. McPhee, *et al.*, Cyclic nucleotide signalling: a molecular approach to drug discovery for Alzheimer's disease (2005).
35. J. L. Bos, Epac: a new cAMP target and new avenues in cAMP research. *Nat. Rev. Mol. cell Biol.* **4**, 733–738 (2003).
36. A. G. Beristain, *et al.*, PKA signaling drives mammary tumorigenesis through Src. *Oncogene* **34**, 1160–1173 (2015).
37. R. Palorini, *et al.*, Protein kinase A activation promotes cancer cell resistance to glucose starvation and anoikis. *PLoS Genet.* **12**, e1005931 (2016).
38. E. Saloustros, *et al.*, Prkar1a gene knockout in the pancreas leads to neuroendocrine tumorigenesis. *Endocr. Relat. Cancer* **24**, 31–40 (2017).
39. S. D. Molyneux, *et al.*, Prkar1a is an osteosarcoma tumor suppressor that defines a molecular subclass in mice. *J. Clin. Invest.* **120**, 3310–3325 (2010).
40. S. A. Boikos, C. A. Stratakis, Carney complex: the first 20 years. *Curr. Opin. Oncol.* **19**, 24–29 (2007).
41. M. Q. Almeida, *et al.*, Mouse Prkar1a haploinsufficiency leads to an increase in tumors in the Trp53+/− or Rb1+/− backgrounds and chemically induced skin papillomas by dysregulation of the cell cycle and Wnt signaling. *Hum. Mol. Genet.* **19**, 1387–1398 (2010).
42. G. R. Wilson, *et al.*, Activated c-SRC in ductal carcinoma in situ correlates with high tumour grade, high proliferation and HER2 positivity. *Br. J. Cancer* **95**, 1410–1414 (2006).
43. B. Elsberger, *et al.*, Is expression or activation of Src kinase associated with cancer-specific survival in ER-, PR-and HER2-negative breast cancer patients? *Am. J. Pathol.* **175**, 1389–1397 (2009).
44. A. Horvath, *et al.*, Mutations and polymorphisms in the gene encoding regulatory subunit type 1-alpha of protein kinase A (PRKAR1A): an update. *Hum. Mutat.* **31**, 369–379 (2010).
45. M. Veugelers, *et al.*, Comparative PRKAR1A genotype–phenotype analyses in humans with Carney complex and prkar1a haploinsufficient mice. *Proc. Natl. Acad. Sci.* **101**, 14222–14227 (2004).
46. E. L. Greene, *et al.*, In vitro functional studies of naturally occurring pathogenic PRKAR1A mutations that are not subject to nonsense mRNA decay. *Hum. Mutat.* **29**, 633–639 (2008).
47. J. G. H. Bruystens, *et al.*, PKA RIα homodimer structure reveals an intermolecular interface with implications for cooperative cAMP binding and Carney complex disease. *Structure* **22**, 59–69 (2014).

48. L. S. Kirschner, *et al.*, A mouse model for the Carney complex tumor syndrome develops neoplasia in cyclic AMP–responsive tissues. *Cancer Res.* **65**, 4506–4514 (2005).

49. K. J. Griffin, *et al.*, A transgenic mouse bearing an antisense construct of regulatory subunit type 1A of protein kinase A develops endocrine and other tumours: comparison with Carney complex and other PRKAR1A induced lesions. *J. Med. Genet.* **41**, 923–931 (2004).

50. A. Linglart, *et al.*, Recurrent PRKAR1A mutation in acrodysostosis with hormone resistance. *N. Engl. J. Med.* **364**, 2218–2226 (2011).

51. Y. Rhayem, *et al.*, Functional characterization of PRKAR1A mutations reveals a unique molecular mechanism causing acrodysostosis but multiple mechanisms causing Carney complex. *J. Biol. Chem.* **290**, 27816–27828 (2015).

52. J. G. H. Bruystens, *et al.*, Structure of a PKA RIα recurrent acrodysostosis mutant explains defective cAMP-dependent activation. *J. Mol. Biol.* **428**, 4890–4904 (2016).

53. M. Kuschel, *et al.*, β2-adrenergic cAMP signaling is uncoupled from phosphorylation of cytoplasmic proteins in canine heart. *Circulation* **99**, 2458–2465 (1999).

54. A. Lochner, S. Genade, E. Tromp, T. Podzuweit, J. A. Moolman, Ischemic preconditioning and the β-adrenergic signal transduction pathway. *Circulation* **100**, 958–966 (1999).

55. E. G. Lakatta, V. A. Maltsev, T. M. Vinogradova, A coupled SYSTEM of intracellular Ca2+ clocks and surface membrane voltage clocks controls the timekeeping mechanism of the heart's pacemaker. *Circ. Res.* **106**, 659–673 (2010).

56. A. M. Katz, B. H. Lorell, Regulation of cardiac contraction and relaxation. *Circulation* **102**, Iv–69 (2000).

57. V. Fuster, R. W. Alexander, R. A. O'Rourke, Hurst's the Heart (2011).

58. D. R. Zakhary, C. S. Moravec, R. W. Stewart, M. Bond, Protein kinase A (PKA)-dependent troponin-I phosphorylation and PKA regulatory subunits are decreased in human dilated cardiomyopathy. *Circulation* **99**, 505–510 (1999).

59. L. S. Kirschner, *et al.*, Mutations of the gene encoding the protein kinase A type I-α regulatory subunit in patients with the Carney complex. *Nat. Genet.* **26**, 89–92 (2000).

60. M. Casey, *et al.*, Mutations in the protein kinase A R1α regulatory subunit cause familial cardiac myxomas and Carney complex. *J. Clin. Invest.* **106**, R31–R38 (2000).

61. K. Tanaka, Alteration of second messengers during acute cerebral ischemia–adenylate cyclase, cyclic AMP-dependent protein kinase, and cyclic AMP response element binding protein. *Prog. Neurobiol.* **65**, 173–207 (2001).

62. R. Milanesi, M. Baruscotti, T. Gnecchi-Ruscone, D. DiFrancesco, Familial sinus bradycardia associated with a mutation in the cardiac pacemaker channel. *N. Engl. J. Med.* **354**, 151–157 (2006).

63. N. Duhme, *et al.*, Altered HCN4 channel C-linker interaction is associated with familial tachycardia–bradycardia syndrome and atrial fibrillation. *Eur. Heart J.* **34**, 2768–2775 (2013).

64. D. DiFrancesco, The role of the funny current in pacemaker activity. *Circ. Res.* **106**, 434–446 (2010).

65. B. Tang, T. Sander, K. B. Craven, A. Hempelmann, A. Escayg, Mutation analysis of the hyperpolarization-activated cyclic nucleotide-gated channels HCN1 and HCN2 in idiopathic generalized epilepsy. *Neurobiol. Dis.* **29**, 59–70 (2008).

66. P. J. Conn, A. Christopoulos, C. W. Lindsley, Allosteric modulators of GPCRs: a novel approach for the treatment of CNS disorders. *Nat. Rev. Drug Discov.* **8**, 41–54 (2009).

67. J. C. DiFrancesco, *et al.*, Recessive loss-of-function mutation in the pacemaker HCN2 channel causing increased neuronal excitability in a patient with idiopathic generalized epilepsy. *J. Neurosci.* **31**, 17327–17337 (2011).

68. P. Cohen, Protein kinases—the major drug targets of the twenty-first century? *Nat. Rev. Drug Discov.* **1**, 309–315 (2002).

69. S. P. Davies, H. Reddy, M. Caivano, P. Cohen, Specificity and mechanism of action of some commonly used protein kinase inhibitors. *Biochem. J.* **351**, 95–105 (2000).

70. Y. Su, *et al.*, Regulatory subunit of protein kinase A: structure of deletion mutant with cAMP binding domains. *Science (80-.).* **269**, 807–813 (1995).

71. R. Soni, D. Sharma, P. Rai, B. Sharma, T. K. Bhatt, Signaling Strategies of Malaria Parasite for its Survival, Proliferation, and infection during erythrocytic Stage. *Front. Immunol.* **8**, 349 (2017).

72. W. Deng, D. A. Baker, A novel cyclic GMP-dependent protein kinase is expressed in the ring stage of the Plasmodium falciparum life cycle. *Mol. Microbiol.* **44**, 1141–1151 (2002).

73. L. Sapio, *et al.*, Targeting protein kinase A in cancer therapy: an update. *EXCLI J.* **13**, 843 (2014).

74. S. Naviglio, *et al.*, Protein kinase A as a biological target in cancer therapy. *Expert Opin. Ther. Targets* **13**, 83–92 (2009).

75. R. Das, *et al.*, Entropy-driven cAMP-dependent allosteric control of inhibitory interactions in exchange proteins directly activated by cAMP. *J. Biol. Chem.* **283**, 19691–19703 (2008).

76. R. Selvaratnam, M. Akimoto, B. VanSchouwen, G. Melacini, cAMP-dependent allostery and dynamics in Epac: an NMR view (2012).

77. B. VanSchouwen, R. Selvaratnam, F. Fogolari, G. Melacini, Role of dynamics in the autoinhibition and activation of the exchange protein directly activated by cyclic AMP (EPAC). *J. Biol. Chem.* **286**, 42655–42669 (2011).

78. N. Popovych, S. Sun, R. H. Ebright, C. G. Kalodimos, Dynamically driven protein allostery. *Nat. Struct. Mol. Biol.* **13**, 831–838 (2006).

79. S.-R. Tzeng, C. G. Kalodimos, Dynamic activation of an allosteric regulatory protein. *Nature* **462**, 368–372 (2009).

80. A. Cooper, D. T. F. Dryden, Allostery without conformational change. *Eur. Biophys. J.* **11**, 103–109 (1984).

81. R. Das, *et al.*, Dynamically driven ligand selectivity in cyclic nucleotide binding domains. *J. Biol.*

Chem. **284**, 23682–23696 (2009).

82. R. Selvaratnam, S. Chowdhury, B. VanSchouwen, G. Melacini, Mapping allostery through the covariance analysis of NMR chemical shifts. *Proc. Natl. Acad. Sci.* **108**, 6133–6138 (2011).
83. J. A. Byun, G. Melacini, NMR methods to dissect the molecular mechanisms of disease-related mutations (DRMs): Understanding how DRMs remodel functional free energy landscapes. *Methods* **148**, 19–27 (2018).
84. S. Boulton, G. Melacini, Advances in NMR methods to map allosteric sites: from models to translation. *Chem. Rev.* **116**, 6267–6304 (2016).
85. R. Selvaratnam, *et al.*, The projection analysis of NMR chemical shifts reveals extended EPAC autoinhibition determinants. *Biophys. J.* **102**, 630–639 (2012).
86. S. Boulton, M. Akimoto, S. Akbarizadeh, G. Melacini, Free energy landscape remodeling of the cardiac pacemaker channel explains the molecular basis of familial sinus bradycardia. *J. Biol. Chem.* **292**, 6414–6428 (2017).
87. X. Xu, *et al.*, Local and global interpretations of a disease-causing mutation near the ligand entry path in hyperpolarization-activated cAMP-gated channel. *Structure* **20**, 2116–2123 (2012).
88. M. Akimoto, *et al.*, A mechanism for the auto-inhibition of hyperpolarization-activated cyclic nucleotide-gated (HCN) channel opening and its relief by cAMP. *J. Biol. Chem.* **289**, 22205–22220 (2014).
89. B. VanSchouwen, G. Melacini, "Regulation of HCN ion channels by non-canonical cyclic nucleotides" in *Non-Canonical Cyclic Nucleotides*, (Springer, 2016), pp. 123–133.
90. B. VanSchouwen, M. Akimoto, M. Sayadi, F. Fogolari, G. Melacini, Role of dynamics in the autoinhibition and activation of the hyperpolarization-activated cyclic nucleotide-modulated (HCN) ion channels. *J. Biol. Chem.* **290**, 17642–17654 (2015).
91. B. VanSchouwen, G. Melacini, Structural basis of tonic inhibition by dimers of dimers in hyperpolarization-activated cyclic-nucleotide-modulated (HCN) ion channels. *J. Phys. Chem. B* **120**, 10936–10950 (2016).
92. F. Fogolari, *et al.*, Distance-based configurational entropy of proteins from molecular dynamics simulations. *PLoS One* **10**, e0132356 (2015).
93. Y. Zhu, *et al.*, Biochemical and pharmacological characterizations of ESI-09 based EPAC inhibitors: defining the ESI-09 "therapeutic window." *Sci. Rep.* **5**, 9344 (2015).
94. S. Boulton, M. Akimoto, R. Selvaratnam, A. Bashiri, G. Melacini, A tool set to map allosteric networks through the NMR chemical shift covariance analysis. *Sci. Rep.* **4**, 7306 (2014).
95. I. Son, R. Selvaratnam, D. N. Dubins, G. Melacini, T. V Chalikian, Ultrasonic and densimetric characterization of the association of cyclic AMP with the cAMP-binding domain of the exchange protein EPAC1. *J. Phys. Chem. B* **117**, 10779–10784 (2013).
96. R. Selvaratnam, M. T. Mazhab-Jafari, R. Das, G. Melacini, The auto-inhibitory role of the EPAC hinge helix as mapped by NMR. *PLoS One* **7**, e48707 (2012).

97. K. J. Moleschi, M. Akimoto, G. Melacini, Measurement of state-specific association constants in allosteric sensors through molecular stapling and NMR. *J. Am. Chem. Soc.* **137**, 10777–10785 (2015).

98. M. Vendruscolo, The statistical theory of allostery. *Nat. Chem. Biol.* **7**, 411–412 (2011).

99. S. K. Hanks, T. Hunter, The eukaryotic protein kinase superfamily: kinase (catalytic) domain structure and classification 1. *FASEB J.* **9**, 576–596 (1995).

100. S. J. Beebe, J. D. Corbin, The Enzymes: Control by Phosphorylation. *Acad. New York* **17**, 43–111 (1986).

101. D. A. Johnson, P. Akamine, E. Radzio-Andzelm, ‡ and Madhusudan, S. S. Taylor, Dynamics of cAMP-dependent protein kinase. *Chem. Rev.* **101**, 2243–2270 (2001).

102. C. Kim, N.-H. Xuong, S. S. Taylor, Crystal structure of a complex between the catalytic and regulatory (RIα) subunits of PKA. *Science (80-.).* **307**, 690–696 (2005).

103. F. Schwede, *et al.*, 8-Substituted cAMP analogues reveal marked differences in adaptability, hydrogen bonding, and charge accommodation between homologous binding sites (AI/AII and BI/BII) in cAMP kinase I and II. *Biochemistry* **39**, 8803–8812 (2000).

104. D. Øgreid, S. O. Døskeland, The kinetics of association of cyclic AMP to the two types of binding sites associated with protein kinase II from bovine myocardium. *FEBS Lett.* **129**, 287–292 (1981).

105. E. T. McNicholl, R. Das, S. SilDas, S. S. Taylor, G. Melacini, Communication between tandem cAMP binding domains in the regulatory subunit of protein kinase A-Iα as revealed by domain-silencing mutations. *J. Biol. Chem.* **285**, 15523–15537 (2010).

106. R. Das, *et al.*, cAMP activation of PKA defines an ancient signaling mechanism. *Proc. Natl. Acad. Sci.* **104**, 93–98 (2007).

107. R. Das, G. Melacini, A model for agonism and antagonism in an ancient and ubiquitous cAMP-binding domain. *J. Biol. Chem.* **282**, 581–593 (2007).

108. M. Abu-Abed, R. Das, L. Wang, G. Melacini, Definition of an electrostatic relay switch critical for the cAMP-dependent activation of protein kinase A as revealed by the D170A mutant of RIα. *Proteins Struct. Funct. Bioinforma.* **69**, 112–124 (2007).

109. R. Das, M. Abu-Abed, G. Melacini, Mapping allostery through equilibrium perturbation NMR spectroscopy. *J. Am. Chem. Soc.* **128**, 8406–8407 (2006).

110. M. T. Mazhab-Jafari, *et al.*, Understanding cAMP-dependent allostery by NMR spectroscopy: comparative analysis of the EPAC1 cAMP-binding domain in its apo and cAMP-bound states. *J. Am. Chem. Soc.* **129**, 14482–14492 (2007).

111. M. Akimoto, *et al.*, Signaling through dynamic linkers as revealed by PKA. *Proc. Natl. Acad. Sci.* **110**, 14231–14236 (2013).

112. M. Akimoto, *et al.*, Mapping the free energy landscape of PKA inhibition and activation: A double-conformational selection model for the tandem cAMP-binding domains of PKA RIα. *PLoS Biol.* **13**, e1002305 (2015).

113. B. VanSchouwen, *et al.*, Mechanism of cAMP partial agonism in protein kinase G (PKG). *J. Biol. Chem.* **290**, 28631–28641 (2015).

114. O. V Vitolo, Sant′ Angelo A, Costanzo V, Battaglia F, Arancio O, Shelanski M. Amyloid beta-peptide inhibition of the PKA/CREB pathway and long-term potentiation: reversibility by drugs that enhance cAMP signaling. *Proc Natl Acad Sci USA* **99**, 13217–13221 (2002).

115. B. Gong, *et al.*, Persistent improvement in synaptic and cognitive functions in an Alzheimer mouse model after rolipram treatment. *J. Clin. Invest.* **114**, 1624–1634 (2004).

116. C. M. Atkins, *et al.*, Modulation of the cAMP signaling pathway after traumatic brain injury. *Exp. Neurol.* **208**, 145–158 (2007).

117. I. Churcher, Tau therapeutic strategies for the treatment of Alzheimer’s disease. *Curr. Top. Med. Chem.* **6**, 579–595 (2006).

1.7 Figures

Figure 1.1

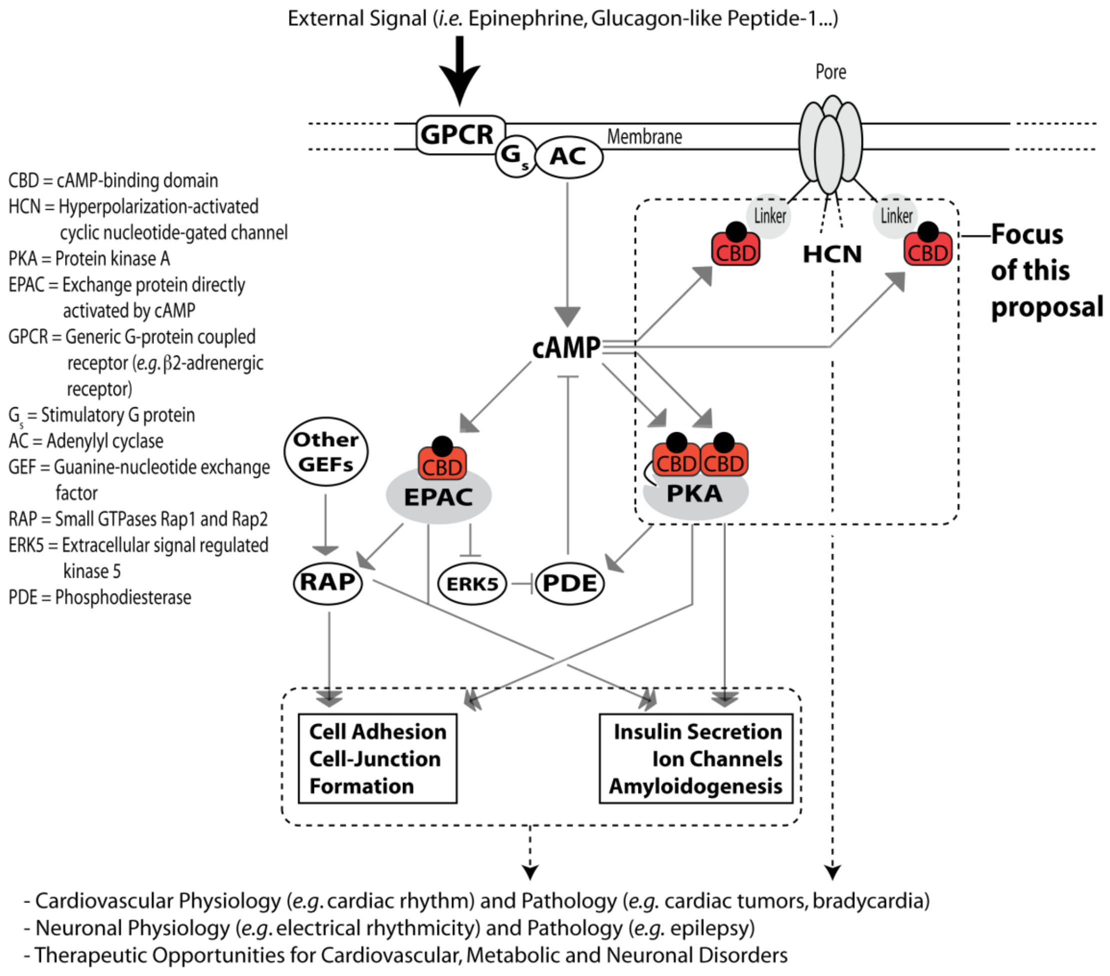

Figure 1.1 HCN, PKA and EPAC mediated cAMP-dependent signaling pathways *(30). HCN, PKA and EPAC are receptors for the cAMP second messenger (filled black circles). The functional cAMP binding domains (CBDs) are shown as red rectangles. Single arrowheads indicate activation, whereas T-shapes denote inhibition. Double arrowheads indicate general (negative or positive) regulation of the processes listed.*

Figure 1.2

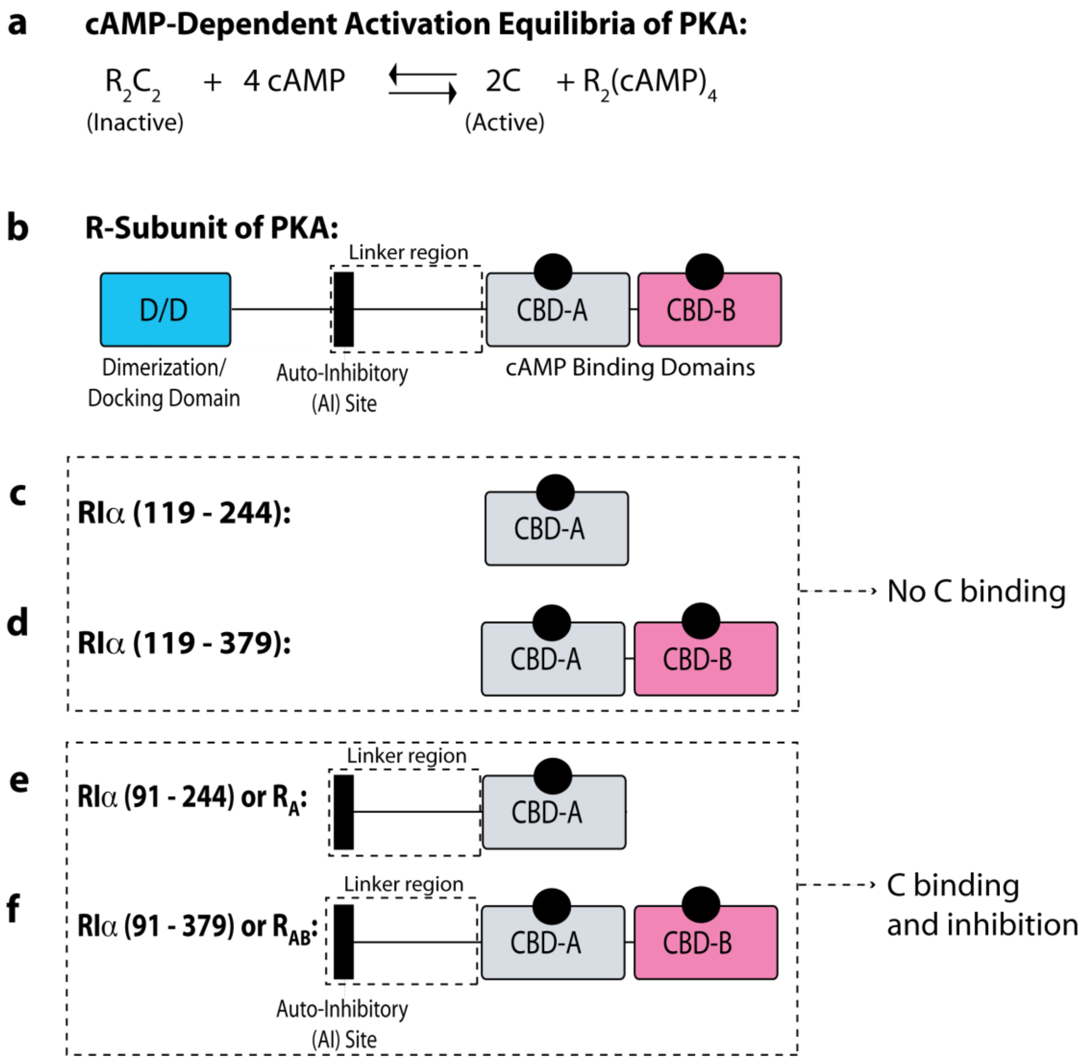

Figure 1.2 ***(a)*** *Inhibitory control of the cAMP-dependent Protein Kinase (PKA). R and C denote the regulatory and catalytic subunits, respectively.* ***(b)*** Domain organization in R. *The line connecting the Dimerization/Docking domain to the cAMP-Binding Domain A schematically represents the linker region and the filled black circles indicate cAMP ligands.* ***(c, d)*** Fragments of RIα studied in the previous CIHR granting period. ***(e, f)*** Constructs of RIα that we now plan to study, i.e. RIα (91-244), also denoted as R_A, and RIα (91-379), also denoted as R_{AB}. *The new constructs span the linker, including the auto-inhibitory site (AI), and therefore they bind and inhibit the C subunit of PKA.*

Figure 1.3

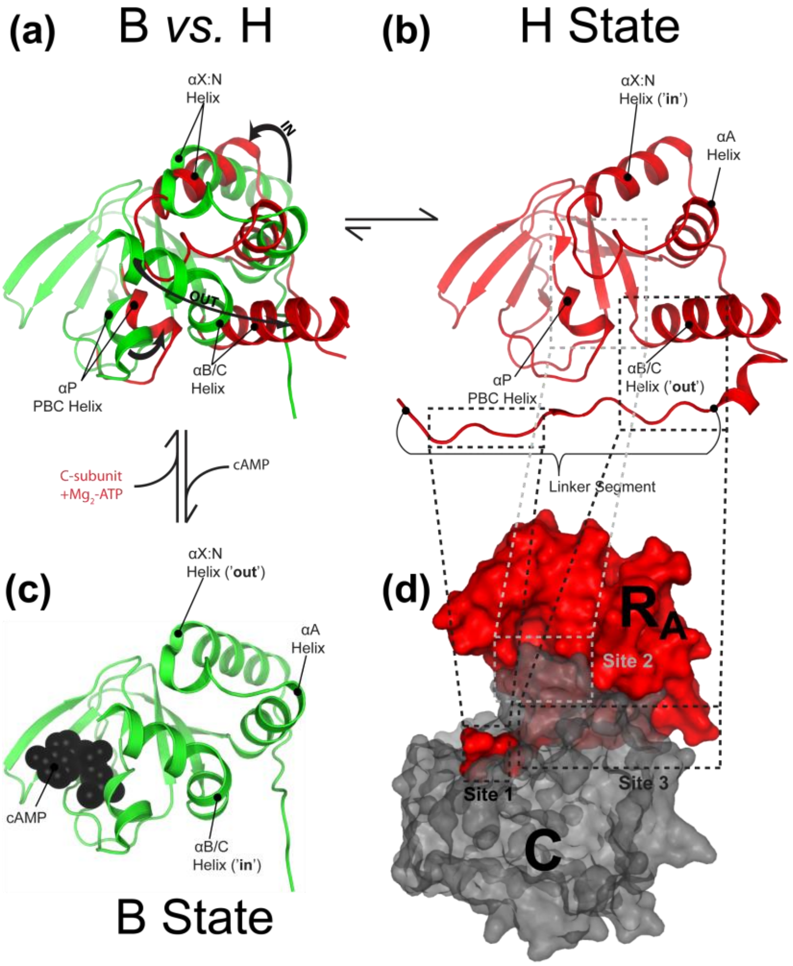

Figure 1.3 Structures of R1α (91-244) *of PKA (R_A) bound to either the C-subunit* **(b,d)** *or cAMP* **(c)** *(70, 102).* **(a)** *Overlap of* **(b)** *and* **(c)**. *These structures define the B (active) and H (inactive) conformations of CBD-A.* **(d)** *Key sites of the R_A:C interface. Site 1 includes the auto-inhibitory sequence (AI). Site 2 comprises the PBC and the central loop of the N-terminal helical bundle of CBD-A, while site 3 involves both the C-terminal helix of CBD-A and the linker segment between the AI site and CBD-A. Adopted from ref (111).*

Figure 1.4

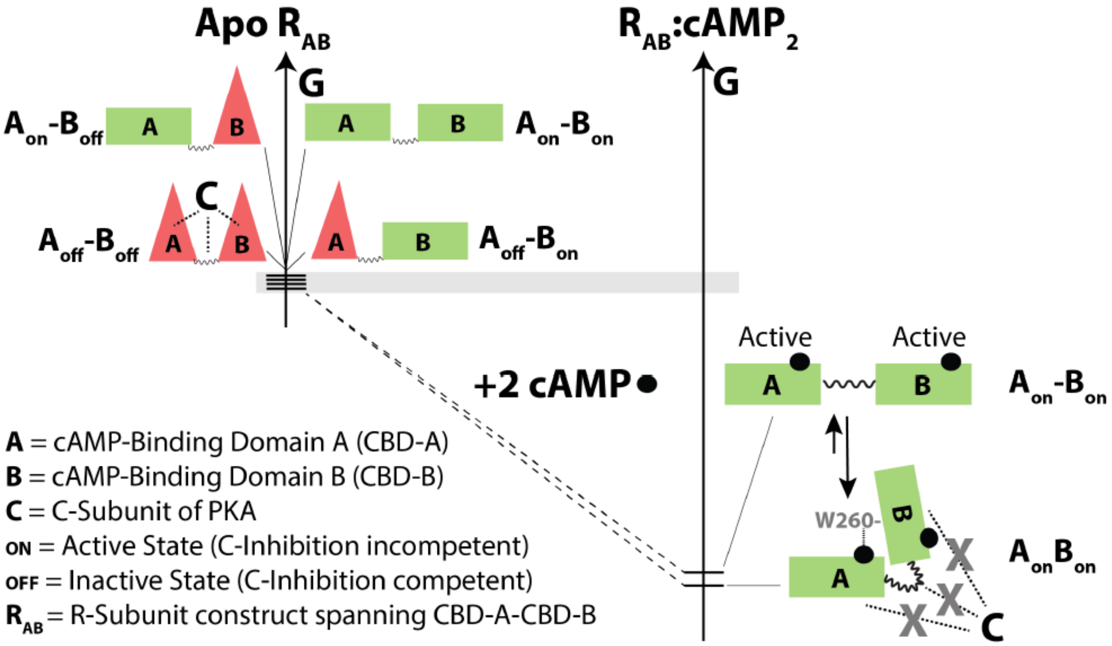

Figure 1.4 *"Double Conformational Selection" model proposed for PKA-RIα activation* (112). R_{AB} denotes the PKA R1α-subunit construct (91-379) spanning the two tandem cAMP-binding domains (CBD-A and –B) and competent to bind and inhibit the PKA C-subunit with nM affinity in the absence of cAMP. "G" stands for free energy. The inactive (OFF) and active states (ON) of each CBD are represented through red triangles and green rectangles, respectively. The hyphen between A and B means that CBD-A and CBD-B do not interact with one another. For example, the notation A_{off}-B_{on} means that when CBD-A and B adopt the OFF and ON states, respectively, they don't interact. The absence of hyphen (*e.g.* $A_{on}B_{on}$ for R_{AB}:cAMP2) means that the two CBDs interact with one another. The grey bar indicates that free energy differences among the states accessible to apo RAB are minimal (*i.e.* of the order of ~RT). Dotted lines denote interactions with the C-subunit of PKA. cAMP is shown as solid black circles. Adapted from reference (112).

Figure 1.5

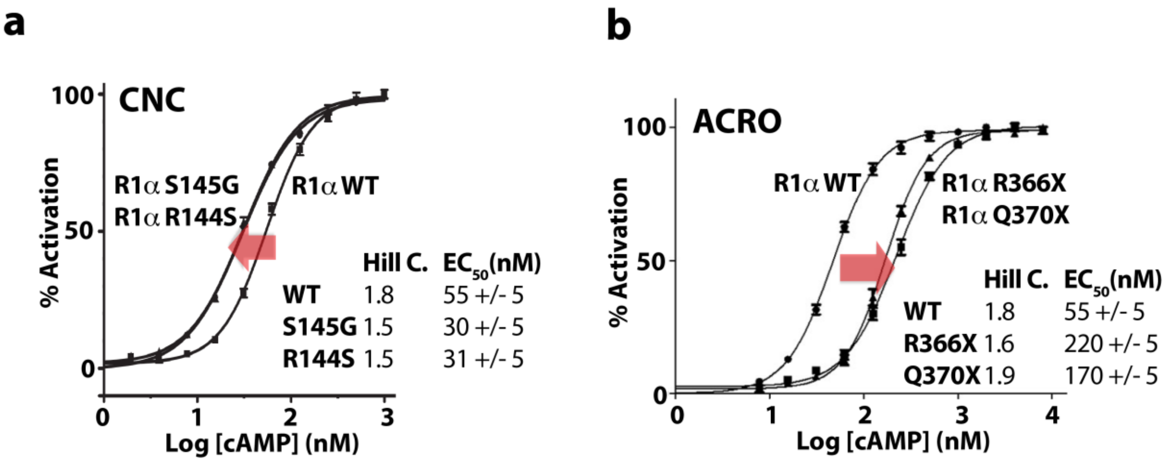

Figure 1.5 *cAMP-Dependent activation of representative PKA R1α Disease Related Mutants (DRMs).* **(a)** Carney Complex (CNC)-causing mutations. **(b)** *Acrodysostosis (ACRO)*-causing mutations (47, 52). These kinase assays illustrate that the CNC and ACRDYS1 mutants exhibit opposite molecular phenotypes: CNC R1α mutations are more easily activated by cAMP than wt, resulting in enhanced PKA activation (*i.e.* gain-of-function), while ACRDYS1 R1α mutations display resistance to cAMP-induced activation relative to wt, causing reduced PKA activation (*i.e.* loss-of-function) (46, 47, 50–52).

Figure 1.6

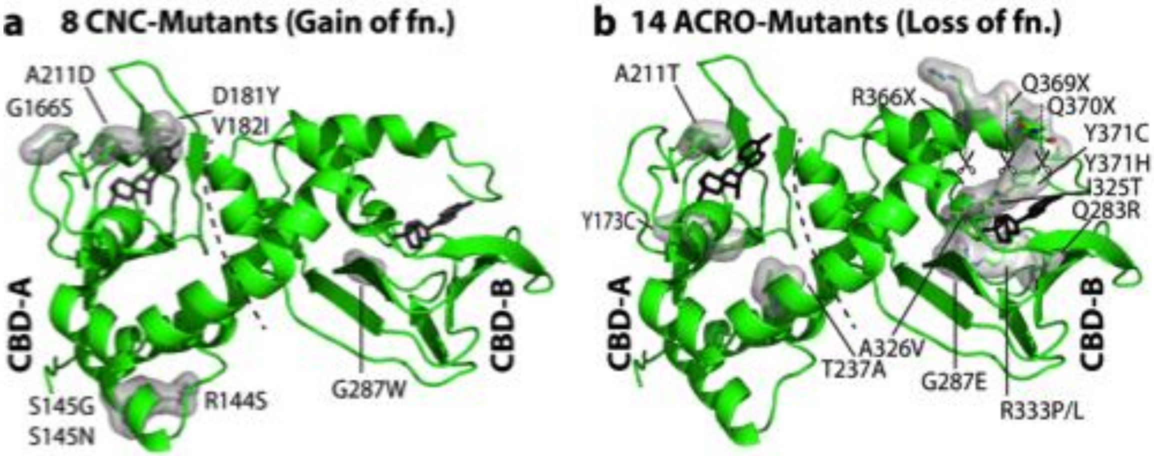

Figure 1.6 (a) Carney Complex (CNC) (47) and **(b)** R1α Acrodysos-tosis (ACRO) (52) mutations mapped as grey surface on the structure of R_{AB}:$cAMP_2$.Dashed line is at the CBD interface.

Chapter 2 Allosteric Sensing of Fatty Acid Binding by NMR: Application to Human Serum Albumin

2.1 Author's Preface

The presented work in this chapter published on July 18, 2016 and inserted here with permission from the Journal of Medicinal Chemistry. Full citation is "Jafari, Naeimeh, Rashik Ahmed, Melanie Gloyd, Jonathon Bloomfield, Philip Britz-McKibbin, and Giuseppe Melacini. "Allosteric sensing of fatty acid binding by NMR: Application to human serum albumin." *Journal of medicinal chemistry* 59, no. 16 (2016): 7457-7465."

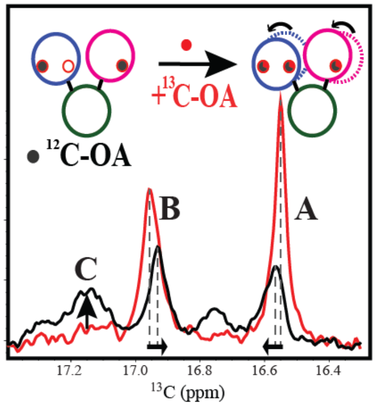

I acquired most of the experiments of the manuscript and analyzed the data. Dr. Rashik Ahmed supported me for revision of the manuscript. Melanie Gloyd acquired some of the preliminary data which help the development of manuscript. Jonathon Bloomfield acquired and analyzed the GCMS data with support from Dr. Philip Britz-McKibbin. Dr. Giuseppe Melacini acquired computational data. I co-wrote the manuscript and designed the research with Dr. Giuseppe Melacini.

2.1.1 Acknowledgments

We thank Prof. Dr. M. Akimoto, S. Boulton, J.A. Byun, T. Lazarou and K. Moleschi for helpful discussions. This project was funded by a grant to G.M. from the Natural Sciences and Engineering Research Council of Canada (NSERC; RGPIN-2014−04514).

2.2 Abstract

Human serum albumin (HSA) serves not only as a physiological oncotic pressure regulator and a ligand carrier, but also as a biomarker for pathologies ranging from ischemia to diabetes. Moreover, HSA is a biopharmaceutical with a growing repertoire of putative clinical applications from hypovolemia to Alzheimer’s disease. A key determinant of the physiological, diagnostic and therapeutic functions of HSA is the amount of long chain fatty acids (LCFAs) bound to HSA. Here, we propose to utilize ^{13}C-Oleic acid for the NMR-based assessment of albumin-bound LCFA concentration (CONFA). ^{13}C-oleic acid primes HSA for a LCFA-dependent allosteric transition that modulates the frequency separation between the two main ^{13}C NMR peaks of HSA-bound oleic acid ($\Delta\nu_{AB}$). Based on $\Delta\nu_{AB}$, the overall $[^{12}\text{C-LCFA}]_{Tot}/[\text{HSA}]_{Tot}$ ratio is reproducibly estimated in a manner that is only minimally sensitive to glycation, albumin concentration or redox potential, unlike other methods to quantify HSA-bound LCFAs such as the albumin-cobalt-binding assay.

2.3 Introduction

Human serum albumin (HSA) is a physiological carrier of a broad spectrum of both exogenous compounds, such as anionic or neutral drugs, and endogenous ligands, such as non-esterified fatty acids (FAs).[1] HSA serves also as a diagnostic biomarker for several diseases, ranging from diabetes to ischemia.[1] For example, the Food-and-Drug Administration approved the ischemia-modified albumin (IMA) as an early biomarker for myocardial ischemia.[2,3] In addition, HSA is an established biopharmaceutical with clinical applications that extend well beyond the treatment of hypovolemia, hemorrhage and hypoalbuminemia.[1] For instance, a new therapeutic opportunity for Alzheimer's disease is based on the ability of albumin to bind the Aβ-peptide, inhibit its self-association and promote its uptake into brain microglia.[4-8]

The three functions of HSA, physiological, diagnostic and therapeutic, are all significantly affected by the content of long-chain fatty acids (LCFAs), which bind albumin with high affinity.[1, 2, 9] HSA includes seven FA binding sites that are distributed over three domains and sequentially occupied by FAs, starting from the higher affinity sites (FA2, 4 and 5) at low FA:HSA stoichiometric ratios (1-2:1) and progressing to the lower affinity loci (FA1, 3, 6 and 7) at higher FA:HSA stoichiometric ratios (≥ 3:1) (Fig. 2.1A).[1, 10] In physiological conditions, up to ~two FA binding sites are occupied by LCFAs.[11] However, in pathological conditions, such as myocardial ischemia, FAs bound to albumin exceed the physiological stoichiometric ratios, resulting in the IMA biomarker.[2, 10] Moreover, the Aβ-self association inhibitory potency is markedly decreased by LCFA binding.[9] Last but not least, LCFAs affect also the physiological carrier function of HSA either through direct ligand competition, as two of the seven FA binding sites overlap with the main drug binding sites in HSA, *i.e.* Sudlow's sites I and II (Fig. 2.1A),[1, 12] or through allosteric conformational changes arising from the reorientation of the N- and C-terminal domains relative to the central domain (Fig. 2.1B).[1] Given the relevance of LCFAs in controlling the diagnostic, therapeutic and physiological functions of HSA, the development of accurate and precise analytical methods to determine the content of LCFAs bound to albumin has attracted considerable interest.[2]

A previously proposed and relatively inexpensive assay for assessing the content of FAs bound to HSA with minimal sample manipulations is the albumin-cobalt-binding (ACB) method.[2] This approach relies on the decreased affinity of albumin for Co(II) ions in the presence of increasing amounts of bound FAs.[2] Enhanced FA binding increases the concentration of free Co(II), which is quantified spectrophotometrically by complex formation with dithiothreitol (DTT).[1,2,13] However, Co(II) ions are vulnerable to air-oxidation to Co(III) in the presence of nitrogen rich compounds including proteins, which in turn influence the result of the ACB assay.[2,14] As a result, the ACB outcomes depend on multiple factors, such as reduction potential and albumin concentration, often compromising the accuracy and reproducibility of the ACB results.[13, 14] Hence, although the ACB approach is highly convenient as it circumvents the need for FA extraction, it is critical to complement the ACB assay with independent methodologies to accurately and reproducibly quantify the amount of FAs bound to albumin, while still preserving the ACB convenience.

Here, we propose an alternative method to reproducibly quantify the amount of FAs bound to albumin. The proposed approach preserves the convenience of the ACB assay, as it avoids FA extraction through the addition of a reporter compound. However, rather than relying on Co(II)/DTT and a colorimetric read out, it simply relies on ^{13}C-methyl-labelled oleic acid (OA) as a reporter molecule and NMR spectroscopy for detection. We show that the ^{13}C-NMR spectra of the added ^{13}C-OA report on the amount of LCFAs bound to albumin prior to addition of ^{13}C-OA, thanks to the FA-dependent allosteric conformational change of HSA. Furthermore, the proposed

^{13}C-OA NMR based assessment of bound-FAs, or CONFA in short, does not significantly depend on physiological variations of albumin concentration or redox potential, unlike the ACB approach. Hence, the proposed NMR strategy complements the ACB assay, providing a precise and independent benchmark assessment of the LCFA-load in HSA.

2.4 Results and Discussion

General CONFA Hypothesis. The hypothesis underlying the CONFA method is that addition of ^{13}C-OA to a solution of albumin at near physiological concentrations (~0.5 mM) and at a 1:1 stoichiometric ratio results in significant allosteric conformational changes in HSA, provided that LCFAs are already bound to albumin prior to addition of ^{13}C-OA. This hypothesis is based on the observation that the allosteric re-orientation of domains one and three relative to domain two is driven primarily by the occupancy of the third highest affinity FA binding site.[1] Such site is only marginally occupied when ^{13}C-OA is added at a 1:1 stoichiometric ratio to albumin devoid of pre-bound FAs, *e.g.* defatted albumin. At this stoichiometric ratio ^{13}C-OA binds primarily at the first two highest affinity sites.[10] Hence, no significant domain re-orientation is expected (Fig. 2.1C, left). However, if ^{13}C-OA is added at the same 1:1 stoichiometric ratio to an albumin that is pre-bound to LCFAs with affinity comparable to that of OA, the occupancy of the third highest affinity FA binding site increases due to the higher total FA load and domain re-orientation is predicted (Fig. 2.1C, right). Such allosteric re-arrangements are expected to result in changes in the spatial environments of the OA methyl groups, which in turn lead to NMR chemical shift changes. Therefore, the ^{13}C-OA added at the 1:1 stoichiometric ratio serves a dual reporter role, as a selective spectroscopic handle distinct from the HSA background and as a primer for the conformational transition, which is triggered primarily by the pre-bound unlabeled LCFAs.

Experimental Test of the CONFA Hypothesis. In order to test the CONFA hypothesis, we acquired the spectra of ^{13}C-OA added at a 1:1 stoichiometric ratio to 0.5 mM defatted HSA either in the absence or presence of 1.5 mM ^{12}C-OA added (Fig. 2.2). Oleic acid was chosen as FA pre-bound to albumin, because it is one of the most abundant FAs in plasma.[10, 15] In the absence of pre-bound ^{12}C-OA, only two peaks are observed, labeled as A and B (Fig. 2.2), which have been assigned to the two highest affinity binding sites in HSA.[10] In the presence of ^{12}C-OA, the intensity of peaks A and B decreases and a third peak is detected, denoted as C (Fig. 2.2), which corresponds to the third highest affinity binding site.[10] One of the factors contributing to the intensity loss of peaks A and B is the isotopic dilution caused by ^{12}C-OA, as the binding sites corresponding to peaks A and B are occupied by both ^{13}C- and ^{12}C-OA (Fig. 2.1C). The appearance of peak C in the presence of ^{12}C-OA confirms that the third highest affinity site is starting to be occupied, as required to drive the re-orientation of HSA domains one and three relative to domain two. Such allosteric conformational transition leads to changes in the positions of peaks A and B (Fig. 2.2). Due to the weak intensity of peak C, the most reproducible spectral change caused by the pre-bound ^{12}C-OA is the frequency separation between peaks A and B, denoted as $\Delta\nu_{AB}$ (Fig. 2.2). Furthermore, $\Delta\nu_{AB}$ is independent of the ^{13}C ppm referencing, circumventing the need of ppm standards or indirect referencing, and is readily measured through 1D ^{13}C NMR spectra (Fig. 2.2). In principle, $\Delta\nu_{AB}$ is also accessible through 2D HSQC spectra,[10] however 1D ^{13}C NMR provides a faster means of obtaining high ^{13}C digital resolution. The sensitivity losses due to the lack of ^{1}H detection are still tolerable if cryoprobes with cold ^{13}C coils, such as the one utilized here, are available. Hence, here we measured $\Delta\nu_{AB}$ primarily though 1D ^{13}C NMR.

In order to confirm that $\Delta\nu_{AB}$ reports on the inter-domain conformational transition of HSA, we acquired negative and positive control spectra (Fig. 2.3). The negative control is provided by the binding of ^{12}C-octanoate (or C8), which is known to bind HSA but it is too short to result in domain re-orientation.[1, 16] As expected, addition of 1:1 ^{13}C-OA to defatted HSA in the presence of ^{12}C-C8 up to a 1:4 HSA:C8 ratio (Fig. 2.3A) did not result in the significant $\Delta\nu_{AB}$ reduction observed instead in the presence of ^{12}C-OA (Fig. 2.2). Consistently with this observation, no peak C was observed either, indicating that the added ^{13}C-OA is confined to the high affinity sites corresponding to peaks A and B. The positive control is obtained by acquiring spectra of the 1:1 defatted HSA:^{13}C-OA complex at increasing pH values (Fig. 2.3B). When the pH is increased above the physiological range up to a value of ~9, HSA is subject to a transition from the normal or native ("N") to the basic ("B") form, which has been hypothesized to mimic the domain re-orientation driven by FAs.[1,16,17] Hence, as anticipated, the $\Delta\nu_{AB}$ separation is progressively reduced as the pH is increased (Fig. 2.3B), similarly to what observed at near physiological pH in the presence of pre-bound ^{12}C-OA (Fig. 2.2). In addition, a weak peak C appears at the high pH values (Fig. 2.3B), consistent with the coupling between site C occupancy and the allosteric transition. Overall, the positive and negative controls of Fig. 2.3 confirm that the $\Delta\nu_{AB}$ frequency difference reports on the re-orientations of domains one and three relative to domain two. Since such allosteric transition is driven by medium and long chain FAs, we expected that $\Delta\nu_{AB}$ is a function of the FAs bound to HSA. In order to explore how $\Delta\nu_{AB}$ depends on the content of bound FAs, we measured $\Delta\nu_{AB}$ in the presence of different amounts of pre-bound ^{12}C-FAs (Fig. 2.4).

Fig. 2.4 reports the $\Delta\nu_{AB}$ separation for ^{13}C-OA added at a 1:1 stoichiometric ratio to albumin pre-bound to different amounts of representative ^{12}C-FAs typically found in the albumin from human serum.[18] Fig. 2.4a shows the $\Delta\nu_{AB}$ measured when HSA is bound to ^{12}C-OA, which is one of the most abundant HSA-bound FAs and the one exhibiting the highest affinity for HSA among the unsaturated FAs, which represent the majority of FAs bound to albumin *in vivo* under normal conditions.[15,18,19] Fig. 2.4a shows that, as the $[^{12}\text{C-OA}]_{\text{Tot.}}/[\text{HSA}]_{\text{Tot.}}$ ratio increases, the $\Delta\nu_{AB}$ values decrease linearly (correlation coefficient of -0.99), as also expected on theoretical grounds (SI Text, pages S3 and S4). A similar linear correlation is observed also for another common unsaturated FA bound to albumin, *i.e.* the doubly unsaturated linoleic acid, which accounts for

~20% of HSA-bound FAs[18] (Fig. 2.4B), and for the triply unsaturated α-linoleic acid (Fig. S2.1B). Linearity is observed also for the dependence of $\Delta\nu_{AB}$ on the amount of the saturated C14:0 FA myristic acid (MA; Fig. 2.4C). MA was chosen because its binding properties resemble those of physiologically common FAs, including the less soluble C16:0, which is a common HSA-bound saturated FA.[2,18] Together the ^{12}C-FAs in Fig. 2.4A-C account for the large majority of FAs that are bound to albumin in human serum and when the $\Delta\nu_{AB}$ values from different ^{12}C-FAs are combined in a single plot (Fig. 2.4d), the linear correlation between $\Delta\nu_{AB}$ and the $[^{12}\text{C-FA}]_{\text{Tot.}}/[\text{HSA}]_{\text{Tot.}}$ ratio (r) is still preserved:

$$\Delta\nu_{AB} = \alpha - \beta\, r \qquad (1)$$

with $\alpha = 71.287$ +/- 0.235 and $\beta = 1.8697$ +/- 0.1057 (correlation coefficient of -0.97). Equation (1) provides a means to estimate the stoichiometric ratio (r) for the total amount of LCFAs bound to HSA prior to addition of the probe ^{13}C-OA, as:

$$r = (\alpha - \Delta\nu_{AB}) / \beta \qquad (2)$$

For example, when ^{13}C-OA is added at a 1:1 stoichiometric ratio to non-defatted albumin fractionated from human serum (Cohn's fraction V), the measured value of $\Delta\nu_{AB}$ is 69.2 +/- 0.5 Hz (Fig. 2.5A), which based on equation (2) leads to an r value of 1.12 +/- 0.30. This CONFA-based prediction is reproducible given the same gHSA batch (Fig. S2.2B), falls in the expected physiological range of r values[11] and is also within error in agreement with the r value measured through solvent extraction and GCMS (Table S2.1), suggesting that the CONFA method based on $\Delta\nu_{AB}$ measurements is a viable approach to estimate the total amount of LCFAs bound to albumins with only minimal sample manipulation.

$\Delta\nu_{AB}$ *vs. Peak Intensities as Proxys for the Amount of HSA-Bound FAs.* The differences in the ^{13}C NMR spectra measured for ^{13}C-OA bound to defatted *vs.* non-defatted albumin are not limited only to the $\Delta\nu_{AB}$ frequency separation, but they extend also to the peak intensities (*e.g.* peaks A and C in Fig. 2.5A). As expected, the intensity of peak C increases in the non-defatted sample, as the presence of ^{12}C-FAs at the high-affinity sites of peaks A and B forces ^{13}C-OA to partially occupy the site of peak C. As a first approximation, the increase in the peak C intensity appears to be linearly correlated with the reduction in $\Delta\nu_{AB}$ values occurring as the amount of ^{12}C-FA is incremented (Fig. 2.5B). However, the signal-to-noise ratio for peak C is relatively low, resulting in an error margin for the peak C intensity that is typically larger than that obtained for the $\Delta\nu_{AB}$ values (Fig. 2.5B). Peak A exhibits a better signal-to-noise ratio than peak C and its relative intensity tends to decrease linearly as the amount of typical ^{12}C-LCFAs increases (Fig. 2.5C). Hence, in principle the relative intensity of peak A provides an additional means to measure the r ratio by utilizing a modified version of equation (2), in which $\Delta\nu_{AB}$ is replaced by the relative intensity of peak A and the α and β parameters are set to 0.972 +/- 0.021 and 0.2091 +/- 0.0094, respectively. However, a reliable determination of the r ratio through the relative intensity of peak A requires excellent signal to noise ratios as well as the defatting of albumin and the acquisition of an additional ^{13}C NMR spectrum for the defatted albumin, which is needed for the normalization of the peak A intensity. In contrast, when the r ratio is measured through the $\Delta\nu_{AB}$ values, a single

^{13}C NMR spectrum is sufficient, excellent signal-to-noise is less critical and no defatting is necessary. Furthermore, the intensity of peak A may be affected by other factors, different from LCFA load, more than the $\Delta\nu_{AB}$ values. For example, aging and glycation affect the peak A intensity in the presence of FAs (Fig.S2.3) more than in the absence (*vide infra*), suggesting that the slope of the linear interpolation in Fig. 2.5C might depend on glycation, unlike the case of $\Delta\nu_{AB}$.

Overall, under our experimental conditions the $\Delta\nu_{AB}$ values appear to provide a more robust, precise and quantitative proxy of the amount of FAs bound to HSA than the peak intensities. Nevertheless, peak intensities are still useful for a more qualitative estimation of the HSA-bound FAs. For example, the 2D ^{1}H-^{13}C HSQC spectra of 0.5 mM ^{13}C-OA added to defatted albumin in the presence of increasing amounts of ^{12}C-OA reveal the progressive occupation of binding sites with decreasing affinities corresponding to peaks C-E (Fig. 2.6). While peak C appears already at a 1:1 $[^{12}\text{C-OA}]_{\text{Tot.}}/ [\text{HSA}]_{\text{Tot}}$ ratio (Fig. 2.4A,B), peaks D and E are observed only at higher $[^{12}\text{C-OA}]_{\text{Tot.}}/ [\text{HSA}]_{\text{Tot}}$ ratios (Fig. 2.4C). Hence, the appearance of HSQC cross-peaks corresponding to lower affinity FA binding sites provides a qualitative proxy to gauge the amount of FAs bound to HSA, although not as quantitatively as the $\Delta\nu_{AB}$ frequency separation.

Robustness of the $\Delta\nu_{AB}$ *as a Quantitative Proxy for the Amount of HSA-Bound LCFAs.* In order to evaluate how $\Delta\nu_{AB}$ is affected by physiological variations in the concentration of albumin in human serum, we acquired 1D ^{13}C spectra for 0.5 mM ^{13}C-OA added to HSA at 0.5-0.7 mM concentrations.[20-22] The resulting $\Delta\nu_{AB}$ values are shown in Fig. 2.7A, illustrating that changes in $\Delta\nu_{AB}$ observed as the HSA concentration changes within the physiological range are either within error or minimal relative to the variations induced by ^{12}C-FA binding (Fig. 2.4). This scenario is in contrast to what observed for other methods of FA quantification, such as the ACB assay, which is known to be biased by physiological variations in the HSA concentration.[13, 14] Furthermore, the ACB assay is also sensitive to the presence of oxidizing agents, whereas the $\Delta\nu_{AB}$ changes observed for albumin under either oxidizing or reducing conditions appear negligible (Fig. 2.7B). In addition, no significant variations in the $\Delta\nu_{AB}$ separation were observed upon albumin glycation for either defatted HSA (Fig. 2.7C) or non-defatted HSA (Fig. S2.3). Overall, the $\Delta\nu_{AB}$ values emerge as a robust proxy for quantitatively assessing the amount of FAs bound to albumins fractionated from human serum.

2.5 Conclusions

We have proposed a method (CONFA) to quantify the amount of LCFAs bound to albumin based on the addition of ^{13}C-OA as a probe molecule and the measurement of the frequency separation between the two main peaks observed in 1D ^{13}C NMR spectra ($\Delta\nu_{AB}$). When ^{13}C-OA is added to HSA at a 1:1 stoichiometric ratio, it functions as a dual reporter probe. It not only serves as a source of NMR signal distinct from the HSA background, but it also primes HSA for an inter-domain reorientation allosterically promoted by the pre-bound unlabeled LCFAs. Such LCFA-driven conformational transition is sensed by the $\Delta\nu_{AB}$ values, which decrease linearly with increasing [^{12}C-LCFA]$_{Tot.}$/[HSA]$_{Tot.}$ ratios. In addition, as the [^{12}C-LCFA]$_{Tot.}$/[HSA]$_{Tot.}$ ratios increase, low-affinity FA-binding sites are progressively occupied, as shown by the appearance of 2D ^{1}H-^{13}C HSQC cross-peaks different from those corresponding to the high-affinity sites. However, the relative errors in the measurement of cross-peak intensities are typically larger than those measured for the $\Delta\nu_{AB}$ values. Hence, peak intensities provide a primarily qualitative proxy of the amount of LCFAs bound to HSA, while the $\Delta\nu_{AB}$ values offer a more quantitative assessment of the [^{12}C-LCFA]$_{Tot.}$/[HSA]$_{Tot.}$ ratios. Similarly to the ACB assay, the $\Delta\nu_{AB}$-based CONFA implementation requires only minimal sample manipulations, but, unlike the ACB assay[13,21], it is only minimally affected by variations in redox potential and in HSA concentration within the physiological range.

Overall, the CONFA method emerges as a robust approach to reproducibly quantify the amount of HSA-bound LCFAs, which is a key determinant of the diagnostic and therapeutic properties of albumins purified from human serum. Hence, the proposed approach is expected to be applicable to and facilitate primarily biopharmaceutical applications of albumin, for example as therapeutic amyloid Aβ inhibitor[4-8]. While the CONFA method can in principle be applied also to plasma (Fig. S2.5), the latter is a complex medium and calibrations obtained in solutions of pure albumin may not be fully transferable to plasma, as previously observed for the ACB assay.[2] Hence, at the current stage, the primary application of the CONFA approach is expected to be for solutions of purified albumins under controlled conditions in a biopharmaceutical rather than a clinical context.

2.6 Experimental Section

Sample Preparation: Human serum albumin (HSA) solutions were prepared using fatty acid and globulin free HSA, denoted here as rHSA (Sigma product number: A3782; ≥99% pure as gauged based on agarose gel electrophoresis), essentially globulin free non-defatted HSA, denoted here as gHSA (Sigma product number: A8763; ≥99% pure as gauged based on agarose gel electrophoresis), and glycated HSA, denoted here as glyHSA (Sigma product number: A8301, 90-100% protein as assessed by the Biuret test). The buffer used for the NMR experiments is 50 mM sodium phosphate, 50 mM sodium chloride, pH 7.4, 99 % deuterium oxide, 0.05 % sodium azide. Albumin was dissolved in the NMR buffer and its concentration was checked by UV absorbance and confirmed by 1D ^{1}H NMR. Defatting of rHSA and glyHSA was carried out by lowering the pH to 3 and incubating for 1.5 hours at room temperature in the presence of a hydroxyalkoxy propyl-dextran VI resin (Sigma product number: H6258). The resin was then removed by filtration (0.2 μm). Fatty acids (FAs) were purchased from Sigma (OA: O1008, ≥ 99% pure based on TLC and GC; LA: L1376, ≥ 99% pure based on GC; α-LA: L2376, ≥ 99% pure based on GC; MA: M3128, ≥ 99% pure based on GC; Octanoic acid, ≥ 99.5% pure as specified by supplier), except ^{13}C-oleic acid, which was from Cambridge Isotope Laboratories (CLM2492, 98% chemical purity and 99% isotopic enrichment as specified by supplier). 100 mM stock FA solutions were prepared in 100 % d_6-dimethyl sulfoxide (DMSO, Cambridge Isotope Laboratories). Samples were prepared by adding stock FA solutions pre-incubated at 50 °C for 5 minutes to a 0.5 mM albumin solution, which was incubated in advance at 37 °C for half an hour. The FA/HSA mixtures were then incubated at 37 °C for two additional hours and their pH adjusted to 7.4 by addition of 1 mM sodium hydroxide before acquiring 1D ^{1}H and ^{13}C NMR spectra. For the redox potential dependence tests, rHSA solutions were incubated at room temperature in the presence of 0.5 mM DTT (from Amresco). For mild oxidation, rHSA solutions were incubated in the presence of 0.004% (v/v) hydrogen peroxide (from Caledon Laboratory Chemicals) for 1.5 hours at room temperature and then stored at 4 °C. Less mild oxidizing conditions were mimicked using a 0.04 % (v/v) concentration of hydrogen peroxide and an incubation time of 3 hours at room temperature. Further information is available as Supplementary Information.

NMR Data Acquisition and Processing: All NMR data were acquired at a Bruker AV700 MHz spectrometer at 298 K with a 5 mm TCI CryoProbe. Unless otherwise specified, the pH was adjusted to 7.4 prior to data acquisition. The 1D-^{13}C NMR data were acquired with ^{1}H decoupling and with a spectral width of 42372.88 Hz and 64K points. The relaxation delay was 1s. The number of scans ranged from 512 to 2048, preceded by 32 dummy scans, resulting in a total experimental time of ~16 min to ~64 min, respectively. Typically, signal-to-noise ratios of at least ~10 for peaks A and B and NMR data acquisition within a day of sample preparation are advisable in the context of the CONFA approach. The 2D ^{13}C-^{1}H correlation spectra (HSQCs)[10,22] were recorded with gradient and sensitivity enhancement, 16 scans and 16 dummy scans, a 1.4-second relaxation delay, and spectra widths of 9765.625 Hz (^{1}H) and 5603.555 Hz (^{13}C) digitized with 2048 (^{1}H) and 256 (^{13}C) points, respectively. Each 2D ^{13}C-^{1}H HSQC experiment was recorded in one hour and ~45 minutes. The ^{13}C-OA not bound to HSA is at a concentration below the NMR detection threshold, since the total concentrations of HSA and OA are orders of magnitude higher that the K_D for LCFA binding.[22] The HSQC and 1D ^{13}C NMR[23-25] peaks observed for HSA-bound ^{13}C-OA were labeled A-E as previously described.[10] Errors in the peak A-B separation in Hz were estimated by recording replicate 1D ^{13}C spectra obtained by repeating both the sample preparation protocol and the NMR data acquisition. The 1D ^{13}C spectra were processed using an exponential multiplication (em) window function with a line-broadening (lb) of 3 Hz, while the 2D ^{13}C-^{1}H HSQC data sets were processed using a 60^{o} shifted squared sine window function and zero filling to 512 points for the t_1 dimension. The measured differences between the ^{13}C resonance frequencies of peaks A and B ($\Delta\nu_{AB}$) were corrected for the effect of DMSO (Fig. S1A). The uncertainty in the estimation of the [^{12}C-FA]$_{Tot.}$/[HSA]$_{Tot}$ ratios (r) through equation (2) was evaluated through error propagation as:

$$\varepsilon_r = r \sqrt{\ } [(\varepsilon_\alpha^2 + \varepsilon_{\Delta\nu}^2)/(\alpha - \Delta\nu_{AB})^2 + (\varepsilon_\beta / \beta)^2] \qquad (3)$$

where ε_α is the error on α (*i.e.* 0.235), ε_β is the error on β (*i.e.* 0.1057) and $\varepsilon_{\Delta\nu}$ is the error on $\Delta\nu_{AB}$. Assuming an error on $\Delta\nu_{AB}$ of ~0.5 Hz, ε_r is 0.3, which indicates that the lowest r ratio measurable through the proposed CONFA method is > 0.3. Equation (3) applies also when r is measured through the relative intensity of peak A. In that case, $\Delta\nu_{AB}$ is replaced by the intensity of peak A relative to defatted albumin and $\varepsilon_{\Delta\nu}$ by the error for the relative intensity of peak A. ε_α and ε_β are then 0.021 and 0.0094, respectively.

Sample Preparation for GCMS Data Acquisition: Fatty acid standards, including myristic acid, C14:0 (≥ 98%, GC), palmitic acid, C16:0 (≥ 99%), stearic acid, C18:0 (approx. 99%, GC), oleic acid, C18:1 (cis) (≥99%) and linoleic acid, C18:3 (all cis) (≥99%) were purchased from Sigma-Aldrich Inc. (Oakville, ON, Canada). The derivatization agent for long-chain fatty acids, N-methyl-N-(trimethylsilyl)trifluoroacetamide (MSTFA) (≥ 98.5%, GC) was also purchased from Sigma Aldrich. Isotopically-labelled myristic acid-D27 (98%), stearic acid-D35 (98%) and pyrene-

D10 (98%) were obtained from Cambridge Isotope Laboratories (Tewksbury, MA, USA). HPLC grade chloroform (≥ 99.5%, GC), methanol (99.8%, GC), hexanes (≥ 99.5%, GC) and Ultra LC-MS grade water were purchased from Caledon Laboratories Ltd. (Georgetown, ON, Canada). Protein-bound non-esterified fatty acids were extracted from human serum albumin (HSA) using a modified version of the classic Folch and Bligh Dyer methods.[29,30] Briefly, to 20 μL of HSA or blank aqueous samples, 10 μL of myristic acid-D27 and stearic acid-D35 in chloroform, serving as recovery standards, were added at 50 ng/μL. Also added were 130 μL 0.9% (w/v) sodium chloride in water, 150 μL methanol and 280 μL chloroform. The solution was vortexed for 3 min and centrifuged for 5 min at 4,000 g for phase separation. The lower organic phase was removed and stored in a separate vial, while the aqueous phase was washed twice with 300 μL chloroform to maximize fatty acid recovery. The three lipid containing chloroform extracts were pooled together and dried under a gentle stream of nitrogen. The dry lipid extracts were then reconstituted in 60 μL hexane. Free fatty acids from the lipid extract were derivatized by adding 30 μL MSTFA to the hexane solution and incubating at 40 °C for 30 min. Prior to GC-MS analysis of the fatty acid trimethylsilyl esters, 10 μL of 10 ng/μL pyrene-D10 was added as an internal standard.

GCMS Data Acquisition: Samples were analyzed in selected ion monitoring (SIM) mode using an Agilent 6890 gas chromatograph (GC) equipped with an Agilent DB17-ht column coupled to an Agilent 5973 single quadrupole mass spectrometer with electron impact ionization (EI-MS). Derivatized non-esterified fatty acids were quantified based on the relative response of their fragment ions (*i.e.* mostly [M-15]+) to that of our internal standard, pyrene-D10 (Table S2). The temperature program used for resolution of major trimethylsilylated fatty acids began at 80 °C held for 2 minutes followed by a 20 °C/min temperature ramp to 160 °C that was further increased to

190 °C and held for 4 minutes to resolve the major C18 species. The temperature was then increased at a rate of 22°C/min until reaching 300 °C at which point the temperature was held for 5 minutes for a total run time of 28 minutes. In all cases, blank-corrected concentrations for total fatty acids non-covalently bound to HSA were measured using external calibration curves with good linearity ($R^2 > 0.980$). The total concentration of major long chain free fatty acids non-covalently bound to HSA was normalized to the ^{13}C-oleic acid (0.5 mM) added during the initial sample preparation for NMR (Table S1). The recovery of the fatty acids was assessed by comparing the relative ion responses of the two deuterated standards spiked into each sample prior to extraction with average recoveries of (83 ± 5)% and (81 ± 9)% for myristic acid-D27 and stearic acid-D35, respectively.

Allosteric Modeling: Details about the allosteric thermodynamic linkage[31-34] model supporting the linearity observed in Figure 4 are available as Supplementary Information.

2.7 References

1. Fanali, G.; di Masi, A.; Trezza, V.; Marino, M.; Fasano, M.; Ascenzi, P. Human serum albumin: from bench to bedside. *Mol. Asp. Med.* **2012,** *33*, 209-290.

2. Lu, J.; Stewart, A. J.; Sadler, P. J.; Pinheiro, T. J.; Blindauer, C. A. Allosteric inhibition of cobalt binding to albumin by fatty acids: implications for the detection of myocardial ischemia. *J. Med. Chem.* **2012,** *55*, 4425-4430.

3. Sbarouni, E.; Georgiadou, P.; Voudris, V. Ischemia modified albumin changes–review and clinical implications. *Clin. Chem. and Lab. Med.* **2011,** *49*, 177-184.

4. Milojevic, J.; Costa, M.; Ortiz, A. M.; Jorquera, J. I.; Melacini, G. In vitro amyloid-β binding and inhibition of amyloid-β self-association by therapeutic albumin. *J. of Alzh. Dis.* **2014,** *38*, 753-765.

5. Milojevic, J.; Esposito, V.; Das, R.; Melacini, G. Understanding the molecular basis for the inhibition of the Alzheimer's Aβ-peptide oligomerization by human serum albumin using saturation transfer difference and off-resonance relaxation NMR spectroscopy. *J. Am. Chem. Soc.* **2007,** *129*, 4282-4290.

6. Milojevic, J.; Melacini, G. Stoichiometry and affinity of the human serum albumin-Alzheimer's Aβ peptide interactions. *Biophys. J.* **2011,** *100*, 183-192.

7. Raditsis, A. V.; Milojevic, J.; Melacini, G. Aβ association inhibition by transferrin. *Biophys. J.* **2013,** *105*, 473-480.

8. Leinenga, G.; Götz, J. Scanning ultrasound removes amyloid-β and restores memory in an Alzheimer's disease mouse model *Science Trans. Med.* **2015,** *278*ra33.

9. Algamal, M.; Milojevic, J.; Jafari, N.; Zhang, W.; Melacini, G. Mapping the Interactions between the Alzheimer's Aβ-Peptide and Human Serum Albumin beyond Domain Resolution. *Biophy. J.* **2013,** *105*, 1700-1709.

10. Krenzel, E. S.; Chen, Z.; Hamilton, J. A. Correspondence of fatty acid and drug binding sites on human serum albumin: a two-dimensional nuclear magnetic resonance study. *Biochemistry* **2013,** *52*, 1559-1567.

11. Peters Jr, T. *All about albumin: biochemistry, genetics, and medical applications*. Academic Press: 1995.

12. Curry, S.; Mandelkow, H.; Brick, P.; Franks, N. Crystal structure of human serum albumin complexed with fatty acid reveals an asymmetric distribution of binding sites. *Nature Struct. Mol. Biol.* **1998,** *5*, 827-835.

13. Hakligor, A.; Kosem, A.; Senes, M.; Yucel, D. Effect of albumin concentration and serum matrix on ischemia-modified albumin *Clin. Biochem.* **2010**, *43* (3), 345-348.

14. Mothes, E.; Faller, P. Evidence that the principal CoII-binding site in human serum albumin is not at the N-terminus: implication on the albumin cobalt binding test for detecting myocardial ischemia. *Biochemistry* **2007,** *46*, 2267-2274.

15. Petitpas, I.; Grüne, T.; Bhattacharya, A. A.; Curry, S. Crystal structures of human serum albumin complexed with monounsaturated and polyunsaturated fatty acids. *J. Mol. Biol.* **2001,** *314*, 955-960.

16. Ascenzi, P.; Fasano, M. Allostery in a monomeric protein: the case of human serum albumin. *Biophys. Chem.* **2010,** *148*, 16-22.

17. van der Vusse, G. J. Albumin as fatty acid transporter. *Drug Metab. and Pharmacok.* **2009,** *24*, 300-307.

18. Saifer, A. and Goldman, L. The free fatty acids bound to human serum albumin. *J. Lipid Res.* **1961,** *2*(3), 268-270.

19. Hamilton, J. A. NMR reveals molecular interactions and dynamics of fatty acid binding to albumin. *BBA-Gen. Subj.* **2013,** *1830*, 5418-5426.

20. Burtis, C. A.; Ashwood, E. R.; Bruns, D. E. *Tietz Textbook of Clinical Chemistry and Molecular Diagnostics*. Elsevier Health Sciences: 2012.

21. Lippi, G.; Plesbiani, M. False myths and legends in laboratory diagnostics. *Clin. Chem. Lab. Med.* **2013,** *51*, 2087-2097.

22. Sarver, R.W.; Gao, H.; Tian, F. Determining molecular binding sites on human serum albumin by displacement of oleic acid *Anal.l Biochem.* **2005**, *347*, 297–302.

23. Simard, J.R.; Zunszain, P.A.; Hamilton, J.A.; Curry S. Location of high and low affinity fatty acid binding sites on human serum albumin revealed by NMR drug-competition analysis *J. Mol. Biol.* **2006**, *361*, 336-51.

24. Simard, J.R.; Zunszain, P.A.; Ha, C.E.; Yang, J.S.; Bhagavan, N.V.; Petitpas, I.; Curry S.; Hamilton, J.A. Locating high-affinity fatty acid-binding sites on albumin by x-ray crystallography and NMR spectroscopy *Proc Natl Acad Sci U S A.* **2005,** *102,* 17958-63.

25. Choi, J.K.; Ho, J.; Curry, S.; Qin, D.; Bittman, R.; Hamilton, J.A. Interactions of very long-chain saturated fatty acids with serum albumin. *J. Lipid Res.* **2002,** *43*, 1000-1010.

26. Lu, J.; Stewart, A.J.; Sleep, D.; Sadler, P.J.; Pinheiro, T.J.; Blindauer, C.A. A molecular mechanism for modulating plasma Zn speciation by fatty acids. *J Am Chem Soc.* **2012,** *134*:1454-1457.

27. Bhattacharya, A.A.; Grüne, T.; Curry, S. Crystallographic analysis reveals common modes of binding of medium and long-chain fatty acids to human serum albumin. *J Mol Biol.* **2000**, *303*:721-32.

28. Hamilton, J.A. Fatty acid interactions with proteins: what X-ray crystal and NMR solution structures tell us *Progr. Lip. Res.* **2004,** *43*, 177-199

29. Folch , J. ; Lees, M. ; Sloane Stanley, G. H. A simple method for the isolation and purification of total lipides from animal tissues. *J. Biol. Chem.* **1957**, *226*:497 – 509.

30. Bligh, E. G. ; Dyer, W. J. A rapid method of total lipid extraction and purification. *Can. J. Biochem. Physiol.* **1959,** *37***:** 911 – 917.

31. Boulton, S.; Melacini, G. Advances in NMR Methods To Map Allosteric Sites: From Models to Translation. *Chem. Rev.* **2016**, *116(11)*:6267-6304.

32. Moleschi, K.J.; Akimoto, M.; Melacini, G. Measurement of State-Specific Association Constants in Allosteric Sensors through Molecular Stapling and NMR. *J. Am. Chem. Soc.* **2015**, *137(33)*: 10777-85.

33. Selvaratnam, R.; Chowdhury, S.; VanSchouwen, B.; Melacini, G. Mapping allostery through the covariance analysis of NMR chemical shifts. *Proc Natl Acad Sci U S A*. **2011**, *108(15)*:6133-8.

34. Boulton, S.; Akimoto, M.; Selvaratnam, R.; Bashiri, A.; Melacini, G. A tool set to map allosteric networks through the NMR chemical shift covariance analysis. *Sci Rep.* **2014**;*4*:7306.

2.8 Figure legends

Figure 2.1: *Location of oleic acid (OA) binding sites in HSA and the basic hypothesis underlying the ^{13}C-OA NMR based assessment of bound-FAs, or CONFA method.* **(A)** Crystal structure of OA-bound HSA (PDB code: 1GNI). Domains one, two and three are shown in pink, green, and blue, respectively. Binding sites two, four, and five (red) exhibit the highest affinities for FAs. Of note is that binding site two (FA2) is close to the interface of domains 1 and 2. Binding site seven overlaps with the drug-binding site known as Sudlow's site I. A second drug-binding site (Sudlow's site II) is located in subdomain 3A and at least partially overlaps with FA binding sites three and four. **(B)** Apo *vs.* OA-bound overlay of HSA structures (PDB codes: 1AO6 and 1GNI, respectively). Domain 2 of the two structures was superimposed. Upon OA-saturation domains one and three rotate relative to domain two, as shown by the arrows. **(C)** Scheme illustrating the FA-dependent inter-domain rearrangement underlying the CONFA method. ^{13}C-OA is added with a ~1:1 stoichiometry to both defatted HSA (left) and non-defatted HSA (right). Solid black circles represent ^{12}C-FAs pre-bound to albumin, while solid red circles denote ^{13}C-OA that serves as the reporter molecule. If HSA is fully defatted (left), ^{13}C-OA binds primarily to the high-affinity binding sites, while the third highest affinity site remains largely unoccupied (note that although such third highest affinity site is shown in domain 3, its exact location is currently not known and it might be located in domain 1. This uncertainty does not affect the interpretation of the CONFA results presented here). If HSA is bound to ^{12}C-OAs (right), ^{13}C-OA binds to the third highest as well as the first two high affinity binding sites and each occupied binding site includes a mixture of ^{12}C- and ^{13}C-OA (right). The occupancy of the third highest affinity site drives the allosteric re-orientation of the N- and C-terminal domains relative to the central domain. Therefore, the NMR properties of ^{13}C-OA, including the chemical shifts, are influenced by the pre-bound ^{12}C-FAs.

Figure 2.2: *1D-^{13}C spectra of ^{13}C-OA added to HSA in the absence and presence of ^{12}C-OA.* 0.5 mM ^{13}C-OA was added to 0.5 mM of defatted HSA in the absence (red) or presence (black and blue) of 1.5 mM ^{12}C-OA. Peaks A and B have been previously assigned to the two highest affinity binding sites in HSA, while peak C corresponds to the third highest affinity site.[10] The ^{12}C-OA pre-bound to HSA influences the frequencies and/or intensities of peaks A-C. Specifically, the separation between peaks A and B as well as their intensities decrease, while peak C appears in the presence of ^{12}C-OA, as expected based on the scheme of Figure 1C. The most reproducible change is the A-B frequency separation, as shown by the black and blue replicas. Only signals from HSA-bound ^{13}C-OA are observed, as the concentration of free ^{13}C-OA is expected to fall below the NMR detection limit.

Figure 2.3: *Control spectra confirm that the A-B frequency separation reports on the allosteric re-orientation of HSA domains.* **(A)** Negative control: octanoic acid (C8) is too short to trigger the conformational transition of HSA[16,26-28] and therefore the separation between peaks A-B is largely independent of the amount of pre-bound C8. No peak C is observed either, consistently with the absence of ^{13}C-OA at this site and the lack of domain re-orientation. **(B)** Positive control: increasing pH above the physiological range up to ~9 is known to result in a transition from the "N" to the "B" forms of HSA.[1, 16, 17] Such N-to-B transition has been hypothesized to resemble that caused by FA binding,[1, 16, 17] shown in Figure 1B, and, as expected, leads to a decrease in A-B frequency separation even in the absence of pre-bound ^{12}C-OA. A weak peak C is detectable at the higher pH values, further confirming the coupling between the third highest affinity binding site occupancy and domain re-orientation.

Figure 2.4: *Correlation between the peak A-B frequency separation ($\Delta\nu_{AB}$) and the HSA occupancy by ^{12}C-FAs.* Correlations were measured for FAs representative of the most abundant HSA-bound LCFAs, *i.e.* ^{12}C-oleic **(A),** ^{12}C-linoleic **(B)** and ^{12}C-myristic acids **(C)**. Panel **(D)** shows the overlay of all the data in the (A-C) using the same symbols as in panels (A-C). Linear regressions using the data displayed in each panel are shown as red solid lines. In (D) the red dashed lines were computed based on the errors in the intercept and slope estimated from the linear regression. The correlation coefficient for the $\Delta\nu_{AB}$ *vs.* ratio of [^{12}C-FA]$_{Tot.}$:[HSA]$_{Tot.}$ plots are reported in the figure. The $\Delta\upsilon_{AB}$ values in this figure are corrected for the effect of DMSO (Fig. S1A), which was needed for FA dissolution. The $\Delta\nu_{AB}$ value measured for rHSA was assigned a [^{12}C-FA]$_{Tot.}$:[HSA]$_{Tot.}$ ratio of zero, because further defatting of rHSA did not result in any significant $\Delta\nu_{AB}$ variation (Fig. S2A).

Figure 2.5: *Application of the CONFA method to non-defatted albumin (gHSA) fractionated from human serum (Cohn's fraction V) and use of relative peak intensities.* **(A)** 1D-^{13}C spectrum of 0.5 mM ^{13}C-OA added to 0.5 mM of gHSA (black). The corresponding spectrum for defatted HSA (rHSA) is included as a reference (red). **(B)** Correlation of the relative intensity of peak C with $\Delta\nu_{AB}$ for 0.5 mM ^{13}C-OA added to 0.5 mM rHSA in the presence of different amounts of ^{12}C-OA. **(C)** Correlation of the relative intensity of peak A with the total concentration of ^{12}C-LCFAs added to 0.5 mM rHSA. Symbols and color-codes are as in Figure 4. Peak intensities were measured though 1D-^{13}C NMR spectra acquired in replicate for error estimation.

Figure 2.6: *Use of 2D ^{1}H-^{13}C HSQC Peak Intensities as a Qualitative Proxy of the Amount of ^{12}C-FA Bound to HSA.* ^{1}H-^{13}C HSQC spectra of 0.5 mM ^{13}C-OA added to 0.5 mM of defatted human serum albumin (rHSA) in the absence **(A)** or presence of 0.5 mM **(B)** and 1.5 mM ^{12}C-OA **(C)**. As the total concentration of added ^{12}C-OA increases, the third highest and low affinity binding sites corresponding to peaks C-E are progressively occupied.

Figure 2.7: *Robustness of the $\Delta\nu_{AB}$ as a Quantitative Proxy for the Amount of HSA-Bound LCFAs.* **(A)** $\Delta\nu_{AB}$ values measured at several concentrations in the physiological range. **(B)** $\Delta\nu_{AB}$ values measured in the presence of reducing or oxidizing agents. Mild oxidation was performed by incubating rHSA with 0.004 % (v/v) H_2O_2 for 1.5 hours. Less mild oxidation was mimicked by increasing the H_2O_2 concentration tenfold and incubating for 3 hours. **(C)** Comparison of 1D ^{13}C NMR spectra for defatted albumins with and without glycation. No significant change in the $\Delta\nu_{AB}$ separation is observed.

2.9 Figures

Figure 2.1

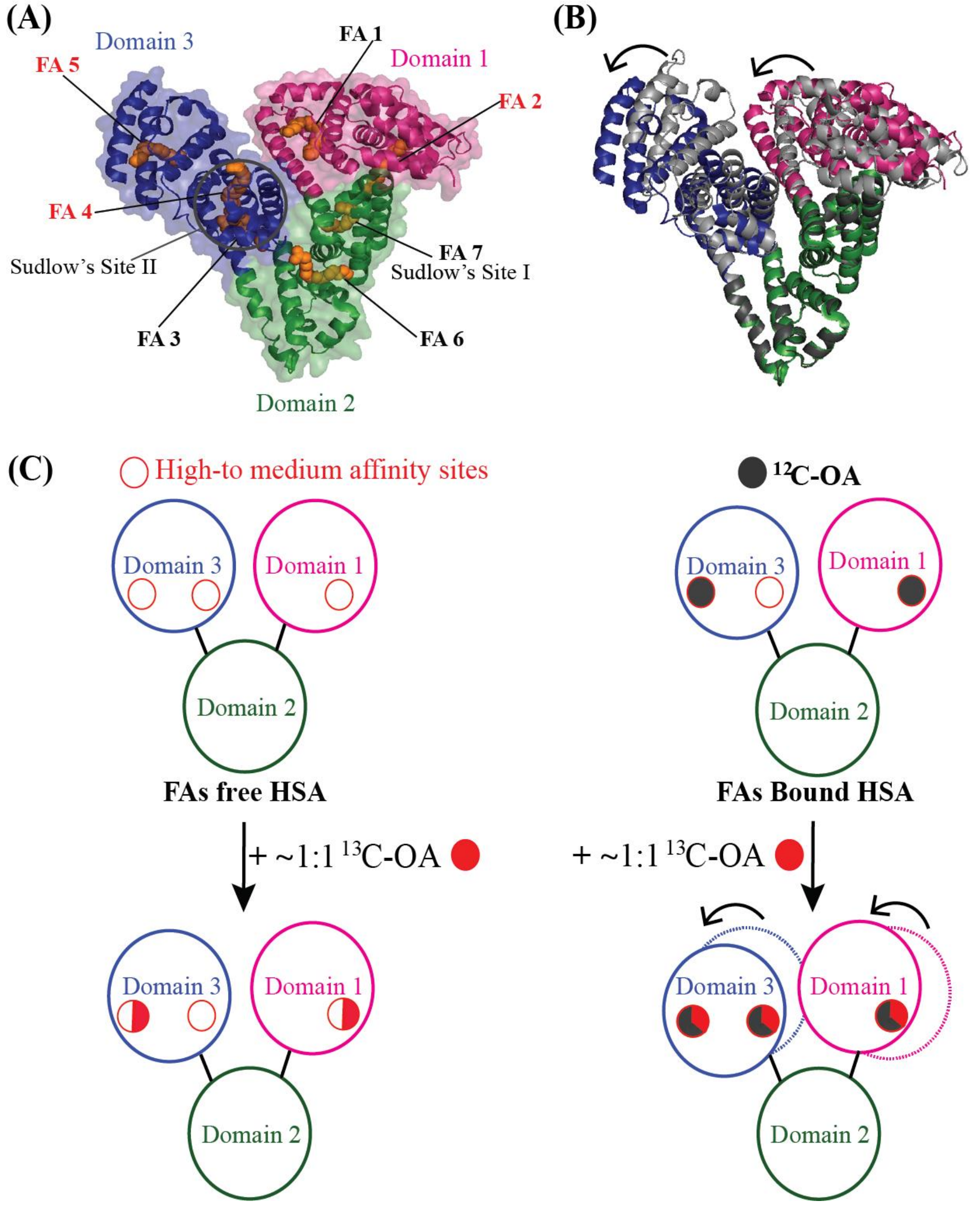

Figure 2.2

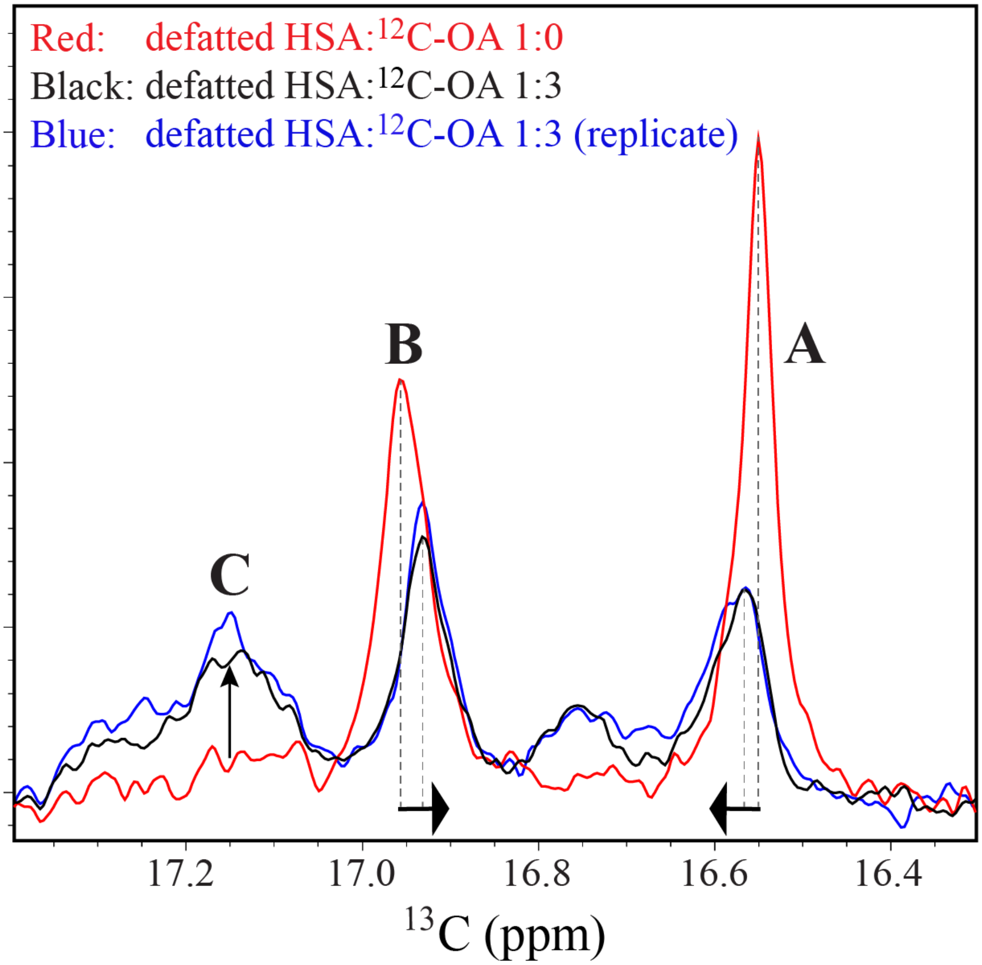
Red: defatted HSA:^{12}C-OA 1:0
Black: defatted HSA:^{12}C-OA 1:3
Blue: defatted HSA:^{12}C-OA 1:3 (replicate)
A
B
C
17.2
17.0
16.8
16.6
16.4
^{13}C (ppm)

Figure 2.3

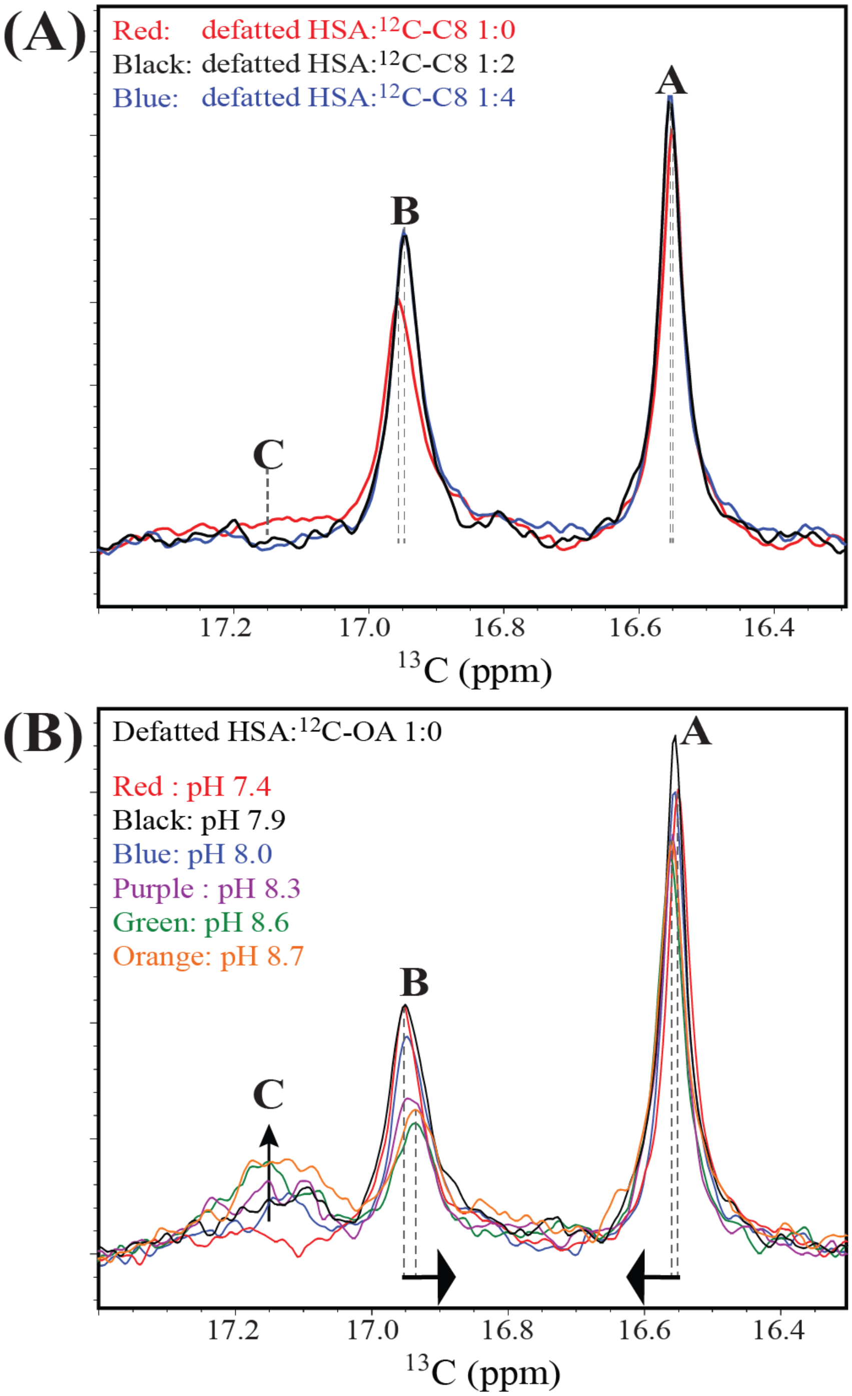
(A)
Red: defatted HSA:^{12}C-C8 1:0
Black: defatted HSA:^{12}C-C8 1:2
Blue: defatted HSA:^{12}C-C8 1:4
A
B
C
17.2
17.0
16.8
16.6
16.4
^{13}C (ppm)
(B)
Defatted HSA:^{12}C-OA 1:0
Red : pH 7.4
Black: pH 7.9
Blue: pH 8.0
Purple : pH 8.3
Green: pH 8.6
Orange: pH 8.7
A
B
C
17.2
17.0
16.8
16.6
16.4
^{13}C (ppm)

Figure 2.4

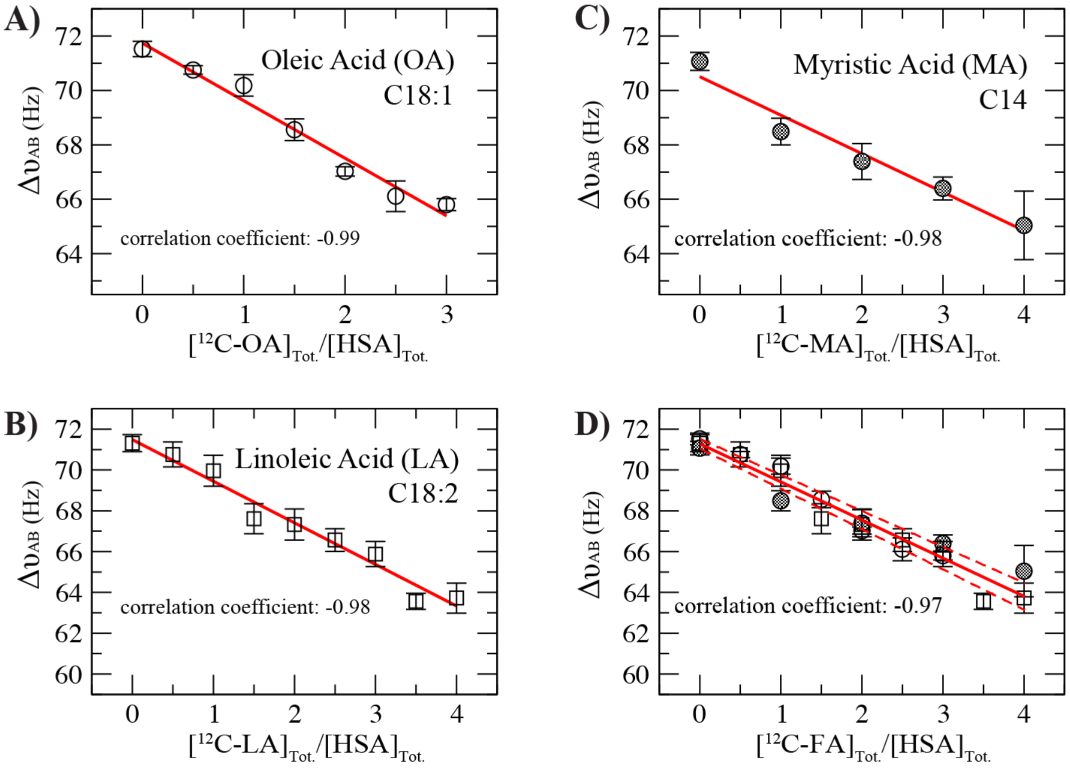
A)
Oleic Acid (OA)
C18:1
correlation coefficient: -0.99
Δυ_AB (Hz)
72
70
68
66
64
0
1
2
3
[12C-OA]Tot./[HSA]Tot.
C)
Myristic Acid (MA)
C14
correlation coefficient: -0.98
Δυ_AB (Hz)
72
70
68
66
64
0
1
2
3
4
[12C-MA]Tot./[HSA]Tot.
B)
Linoleic Acid (LA)
C18:2
correlation coefficient: -0.98
Δυ_AB (Hz)
72
70
68
66
64
62
60
0
1
2
3
4
[12C-LA]Tot./[HSA]Tot.
D)
correlation coefficient: -0.97
Δυ_AB (Hz)
72
70
68
66
64
62
60
0
1
2
3
4
[12C-FA]Tot./[HSA]Tot.

Figure 2.5

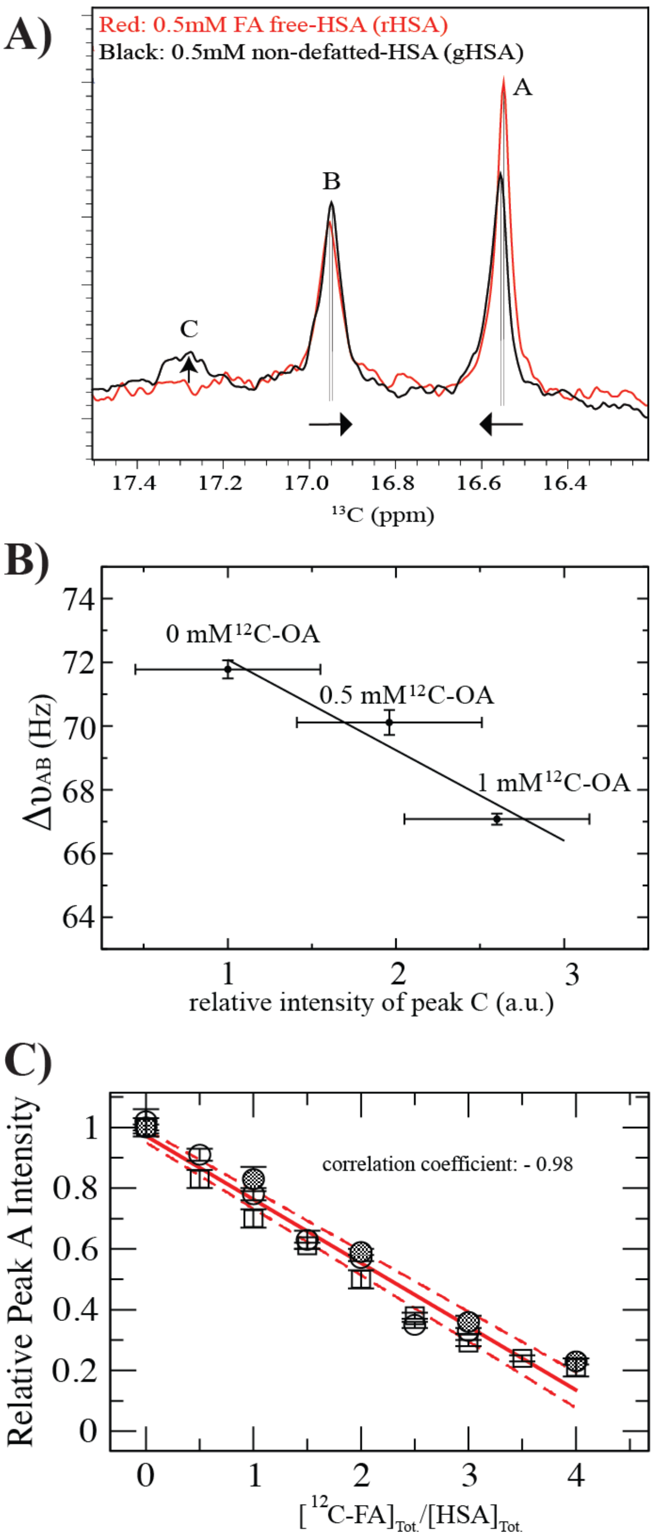
A)
Red: 0.5mM FA free-HSA (rHSA)
Black: 0.5mM non-defatted-HSA (gHSA)
A
B
C
17.4
17.2
17.0
16.8
16.6
16.4
¹³C (ppm)
B)
0 mM¹²C-OA
0.5 mM¹²C-OA
1 mM¹²C-OA
Δυ_AB (Hz)
74
72
70
68
66
64
1
2
3
relative intensity of peak C (a.u.)
C)
correlation coefficient: - 0.98
Relative Peak A Intensity
1
0.8
0.6
0.4
0.2
0
0
1
2
3
4
[¹²C-FA]Tot./[HSA]Tot.

Figure 2.6

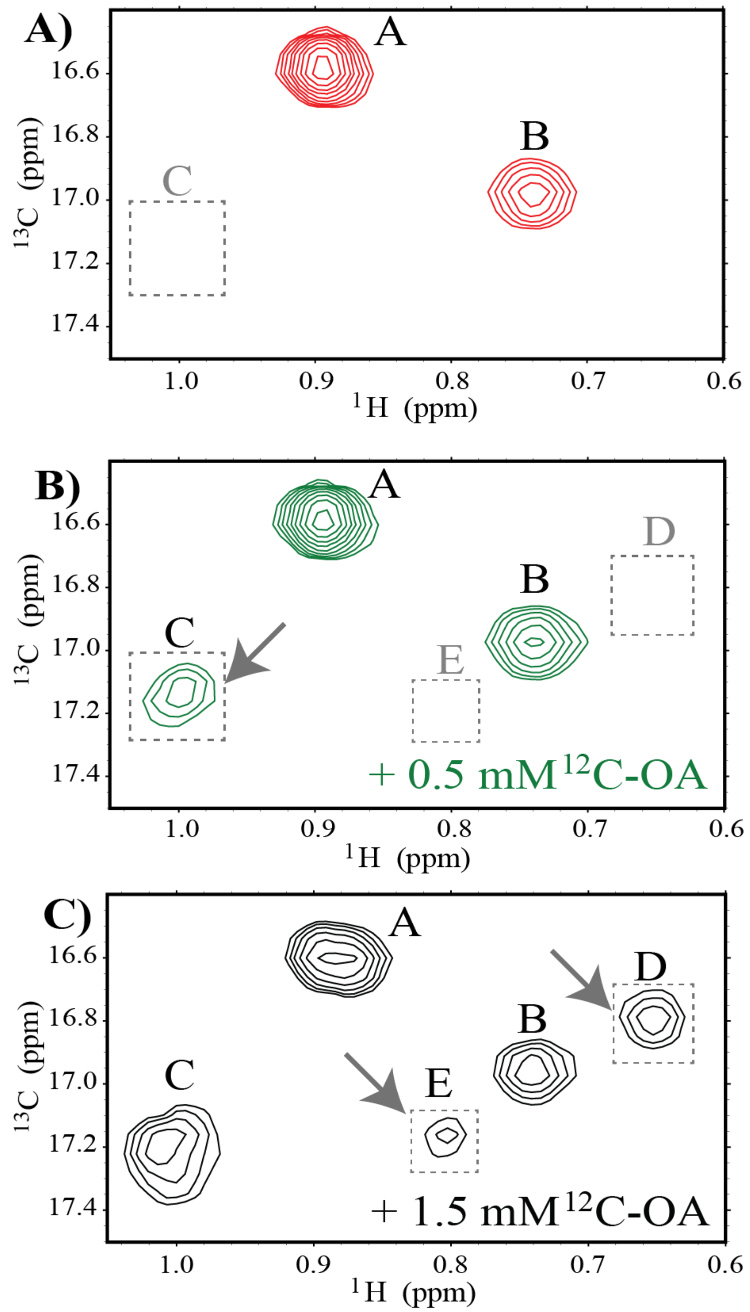
A)
A
B
C
16.6
16.8
17.0
17.2
17.4
13C (ppm)
1.0
0.9
0.8
0.7
0.6
1H (ppm)
B)
A
B
C
D
E
+ 0.5 mM 12C-OA
C)
A
B
C
D
E
+ 1.5 mM 12C-OA

Figure 2.7

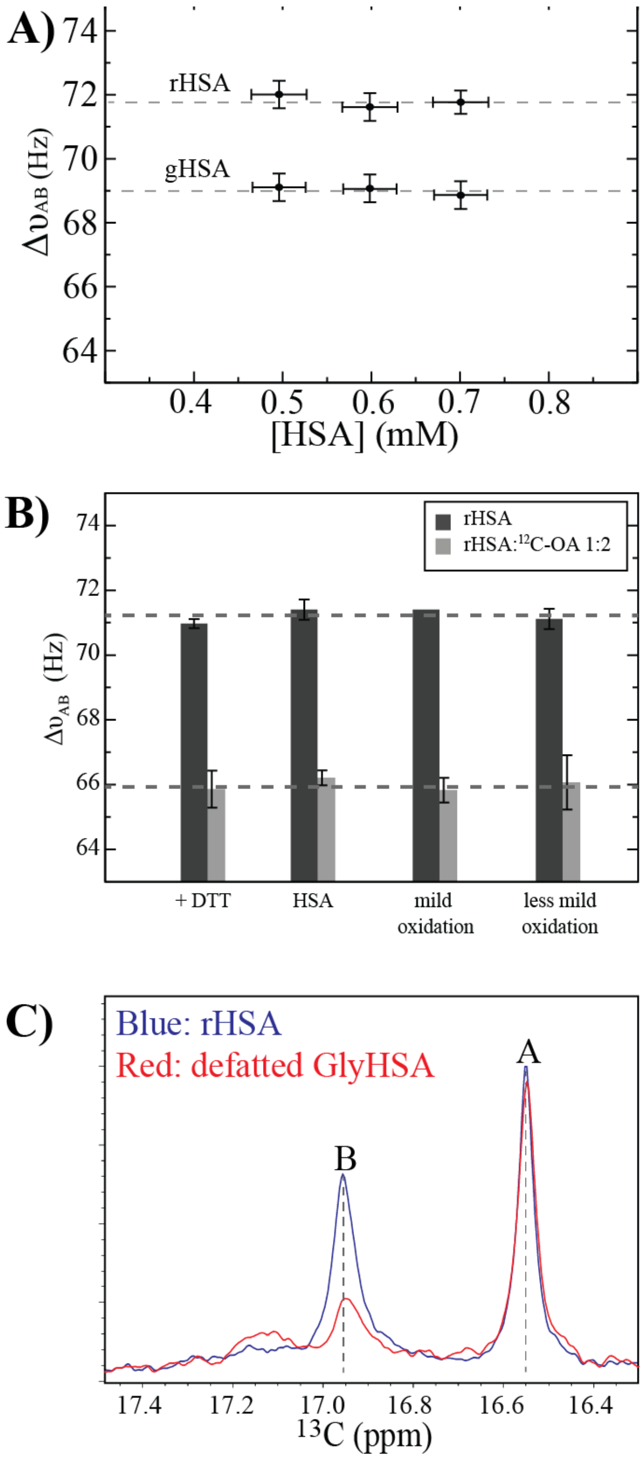
A)
74
72
70
68
66
64
$\Delta\upsilon_{AB}$ (Hz)
rHSA
gHSA
0.4
0.5
0.6
0.7
0.8
[HSA] (mM)
B)
rHSA
rHSA:^{12}C-OA 1:2
74
72
70
68
66
64
$\Delta\upsilon_{AB}$ (Hz)
+ DTT
HSA
mild oxidation
less mild oxidation
C)
Blue: rHSA
Red: defatted GlyHSA
A
B
17.4
17.2
17.0
16.8
16.6
16.4
^{13}C (ppm)

2.10 Supplementary Information for Allosteric Sensing of Fatty Acid Binding by NMR: Application to Human Serum Albumin

2.10.1 Theoretical Derivation of the Linear Relationship between $\Delta\nu_{AB}$ and the r Ratio

Considering that the $\Delta\nu_{AB}$ change as a function of the total amount of LCFAs bound to albumin is the result of variations in the spatial environment of sites A and B occurring during an allosteric transition, let's focus on one of the simplest possible models of allostery, *i.e.* a ligand-dependent equilibrium between two conformations, generally referred to here as T and R (Figure S2.4). For example, the T to R transition could represent the LCFA-driven re-orientation of domains 1 & 3 relative to domain 2 in albumin. Let's define as L the T *vs.* R equilibrium constant in the absence of ligand:

$$L = [T]/[R] \qquad (S1)$$

where [T] and [R] denote the apo concentrations of T and R, respectively. If L > 1, then T is the most populated conformer in the absence of ligand. However, when a ligand "A" that selectively binds the R state is added, the fraction of R is increased. For example, when LCFAs bind to site C the populations of conformers with re-oriented domains 1 & 3 increases. The ligand-dependent increase in the fraction of the R state, *i.e.* x_R, is quantified according to the following equations:

$$x_R = ([R] + [RA]) / ([R] + [T] + [RA]) \qquad (S2)$$

Based on equation (S1) and considering that $K_R = [RA]/[R][A]$ is defined as the association constant for the RA complex (Figure S2.4), then equation (S2) rearranges to:

$$x_R = (1 + K_R[A]) / (1 + L + K_R[A]) \qquad (S3)$$

The concentration of free ligand, *i.e.* [A] appearing in equation (S3), is related to the fractional occupancy (x_C) of the binding site that drives the T to R allosteric transition (*e.g.* site C in the case of albumin relevant here):

$$x_C = [RA] \;/\; ([R] + [T] + [RA]) \quad (S4)$$

which, based on equation (S1) and the definition of K_R, rearranges to:

$$x_C = K_R[A] \;/\; (1 + L + K_R[A]) \quad (S5)$$

or:

$$K_R[A] = x_C (L+1)/(1- x_C) \qquad (S6)$$

Equation (S6) is then combined with equation (S3), to relate x_R to x_C, *i.e.* the fractional occupancy of site C:

$$x_R = (1 + Lx_C) / (1 + L) \qquad (S7)$$

Showing that x_R and x_C are linearly related. Furthermore, x_R is linearly related also to ligand dependent chemical shift changes, because typically only a single peak is observed for each FA binding site pointing to fast exchange between the T and R conformations in the chemical shift NMR time scale. Hence, the observed chemical shifts for ^{13}C-OA at sites A and B are linear averages between those in the T and R states, *i.e.* δ_R and δ_T:

$$\delta_{obs} = x_R\, \delta_R + (1-x_R)\, \delta_T \qquad (S8)$$

or, defining $\Delta\delta = \delta_R - \delta_T$:

$$\delta_{obs} = \delta_T + \Delta\delta\, x_R \quad (S9)$$

Equation S8 shows that d_{obs} depends linearly on x_R, which in turn depends linearly on x_C (equation S7). Hence, d_{obs} and x_C are linearly correlated:

$$\delta_{obs} = \delta_T + \Delta\delta(1 + Lx_C)/(1 + L) \qquad \text{(S10)}$$

Equation S10 applies to both site A and site B (*i.e.* $\delta_{obs,A}$ and $\delta_{obs,B}$). The difference between these two chemical shifts ($\Delta_{AB}\delta_{obs}$) then becomes:

$$\Delta_{AB}\delta_{obs} = \Delta_{AB}\delta_T + \Delta_{AB}\Delta\delta(1 + Lx_C)/(1 + L) \qquad \text{(S11)}$$

Since $\Delta\nu_{AB} = B_o\, \Delta_{AB}\delta_{obs}$, where B_o is the NMR spectrometer field strength in MHz (*i.e.* ~700/4 MHz for ^{13}C in our case), equation S11 becomes:

$$\Delta\nu_{AB} = B_o\Delta_{AB}\delta_T + B_o\Delta_{AB}\Delta\delta(1 + Lx_C)/(1 + L) \quad \text{(S12)}$$

Equation (S12) shows that $\Delta\nu_{AB}$ depends linearly on x_C. Since x_C is defined as the fractional occupancy of site C, x_C is proportional to the intensity of the NMR signal observed for site C (since inter-site exchange is slow in the NMR chemical shift time scale, unlike the T *vs.* R inter-state exchange, which is fast). The intensity of the NMR signal observed for site C has been shown to depend ~linearly on the ratio (r) between the total LCFA and HSA concentrations (10). Such linear dependence of x_C on concentration is expected also on theoretical grounds, considering that the total concentrations of HSA (*i.e.* ~0.5 mM) by far exceeds the dissociation constant for the binding of LCFAs to site C, leading to an essentially linear binding isotherm prior to saturation. We therefore conclude that equation (S12) proves the linear relationship between $\Delta\nu_{AB}$ and the r ratio, as also experimentally observed in Figure 4 for a variety of LCFAs and formalized through equation (1) in the Main Text.

2.10.2 Tables

Table S2.1

Table S2.1: Average concentration of major non-esterified LCFAs bound to gHSA measured by GC-MS[a]

LCFA	**[LCFA] / mM**
Myristic Acid	0.02 ± 0.01
Palmitic Acid	0.14 ± 0.09
Palmitoleic Acid	0.02 ± 0.02
Stearic Acid	0.10 ± 0.08
Oleic Acid	0.16 ± 0.10
Linoleic Acid	0.24 ± 0.18
Arachidonic Acid	0.06 ± 0.05
r ratio	**1.48 ± 0.49**

[a] Concentrations of LCFAs in 0.5 mM gHSA samples were measured through solvent extraction and GCMS. In this context, LCFAs are defined as fatty acids with chain length ≥ C14. Concentrations of the LCFAs listed are relative to 0.5 mM ^{13}C-oleic acid added as control FA to gHSA, as in the preparation of the NMR samples. Errors were estimated as standard deviations from triplicates. The r ratio is defined as in the main text: $r = [LCFA]_{Tot.}/[HSA]_{Tot.}$

Table S2.2

Table S2.2: Summary of retention times and measured ions for major non-esterified LCFAs and recovery/internal standards from human serum albumin extracts as their trimethylsilyl derivatives using GC-MS with selective ion monitoring.

LCFA	**RT (min)**	**Ion (*m/z*)**
Myristic Acid-D27	10.406	312
Myristic Acid	10.796	285
Palmitic Acid	14.137	313
Palmitoleic Acid	14.221	311
Stearic Acid-D35	17.598	376
Stearic Acid	18.515	341
13C Oleic Acid	18.418	340
Oleic Acid	18.419	339
Linoleic Acid	18.882	337
Arachidonic Acid	22.407	117

2.10.3 Supplementary Figures

Figure S 2.1

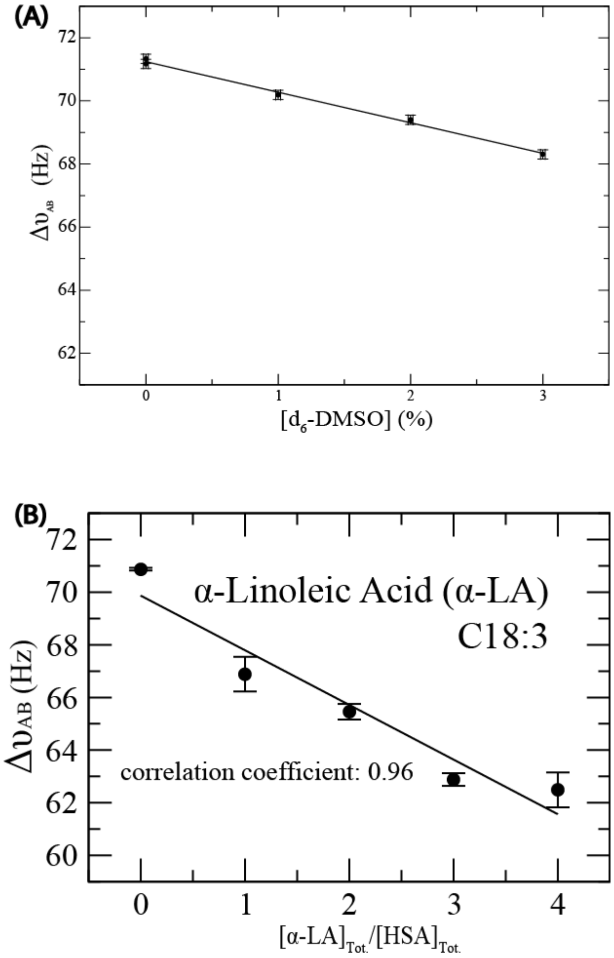

Figure S2.1: (A) *Effect of DMSO on the peak A-B separation ($\Delta\nu_{AB}$).* The highest percentage of d_6-DMSO added to the HSA samples was less than 3 %. Within this range, there is a linear correlation between $\Delta\nu_{AB}$ (Hz) and the concentration of d_6-DMSO. **(B)** As Figure 4B, but for the triply unsaturated ^{12}C-a-linoleic acid.

Figure S 2.2

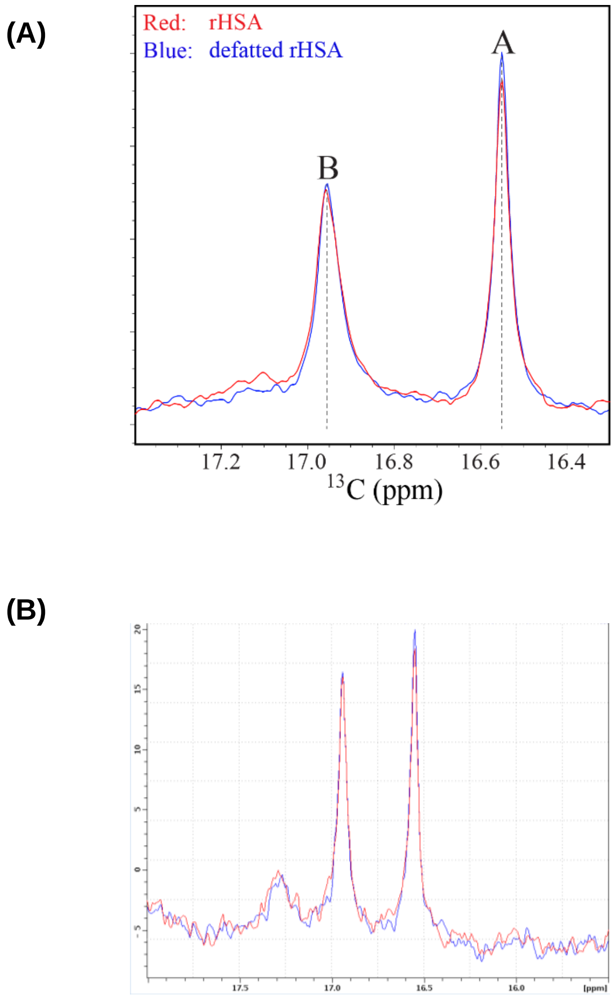

Figure S2.2: (A) 1D ^{13}C NMR spectra of ^{13}C-OA added at a 1:1 stoichiometric ratio to 0.5 mM rHSA either before or after defatting. No significant variation is observed in the separation of peaks A and B, suggesting that rHSA was already quantitatively defatted. **(B)** Replicas of 1D ^{13}C NMR spectra of ^{13}C-OA added at a 1:1 stoichiometric ratio to 0.5 mM gHSA.

Figure S 2.3

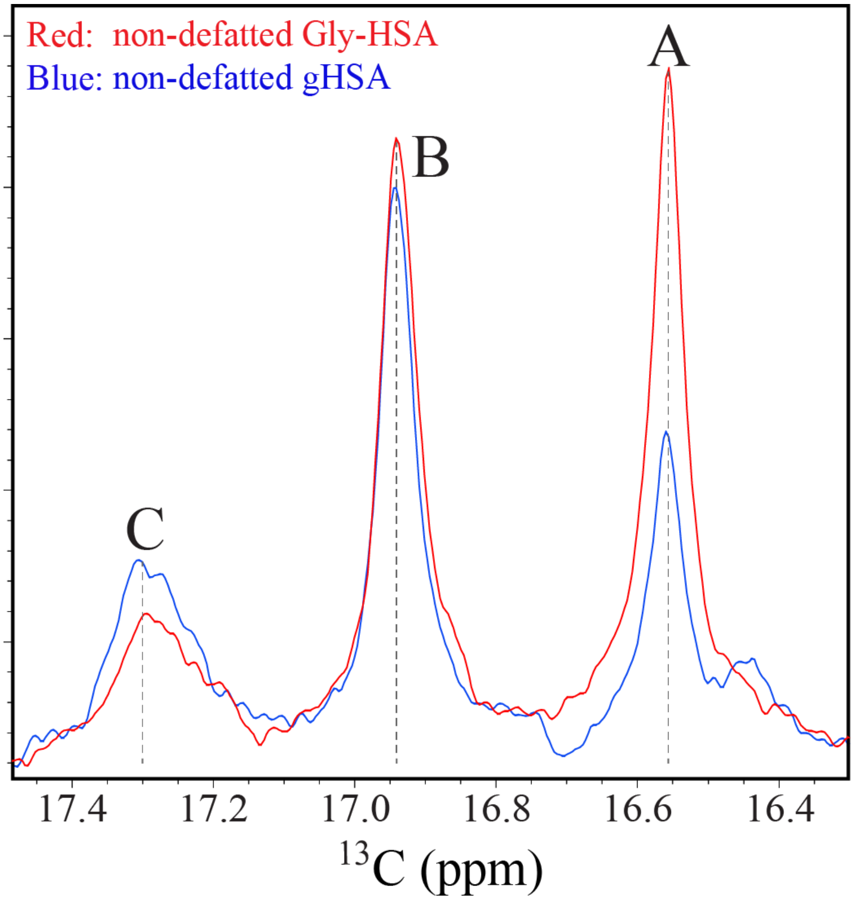

Figure S2.3: 1D ^{13}C NMR spectra of ^{13}C-OA added at a 1:1 stoichiometric ratio to 0.5 mM non-defatted HSA either with or without glycation. No significant variation is observed in the separation of peaks A and B, indicating that glycation does not appreciably alter the $\Delta\nu_{AB}$ value.

Figure S 2.4

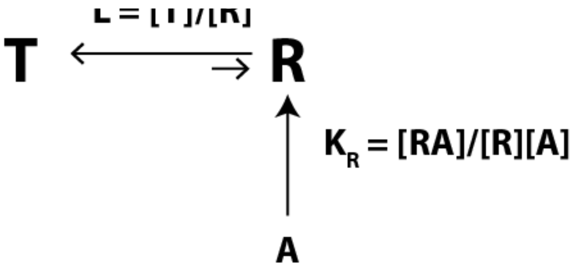

Figure S2.4: Allosteric model for the re-orientation of domains 1 and 3 relative to domain 2 of albumin. In the absence of ligand A, the prevailing conformer is referred to as “T”. Ligand A selectively binds the “R” conformer with re-oriented domains 1 and 3. L is the equilibrium constant for the T *vs.* R conformational inter-conversion, while K_R is the association constant for the binding of A to the R state. It is assumed that the affinity of A for T is negligible (*i.e.* $K_T \sim 0$). In the case of albumin, the T to R transition is driven primarily by the occupancy of site C and therefore K_R refers to the affinity of LCFAs to this site.

Figure S 2.5

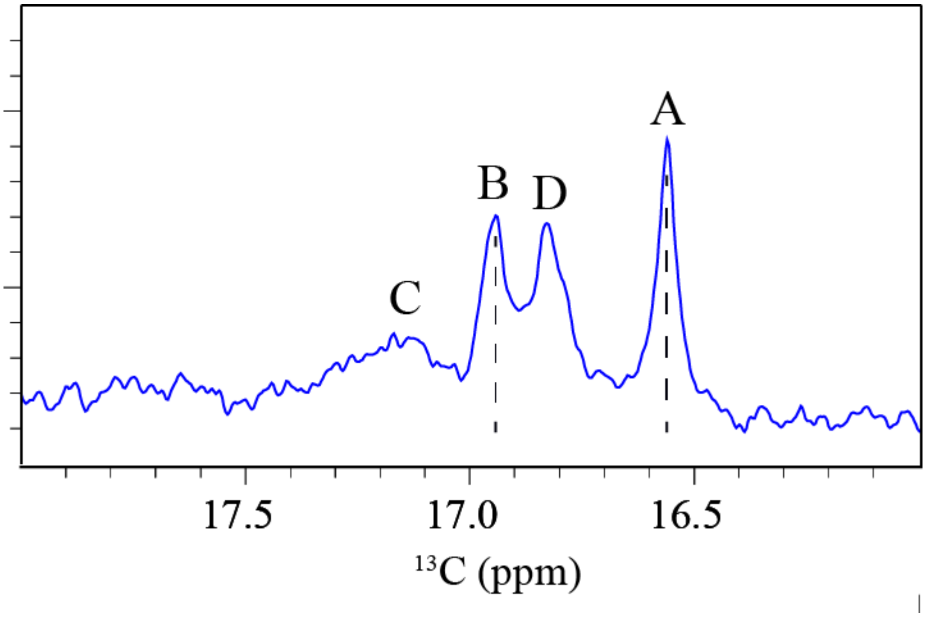

Figure S2.5: 1D ^{13}C NMR spectrum of 0.5 mM ^{13}C-OA added to reconstituted human plasma. Lyophilized Human Plasma purchased from Sigma Aldrich (Lot# SLBL6438V) was reconstituted in 5 mL of 100% D_2O and filtered (0.2 mm). An aliquot of 500 µL was incubated at 37 °C for 30 minutes. To this mixture 2.5 µL of 100 mM ^{13}C-oleic acid stock in DMSO-d_6 was added. The stock solution was pre-incubated at 50 °C for 5 minutes prior to its addition. The resulting sample was further incubated at 37 °C for 2 hours prior to analysis by NMR at 25 °C and pH 7.4. Peaks are labeled based on ppm similarity to 1D ^{13}C NMR spectra of 0.5 mM ^{13}C-OA added to purified human albumin solutions. However, we cannot rule out that additional peaks, unique of plasma, may occur at similar chemical shift values.

Chapter 3 Non-Canonical Protein Kinase A Activation by Polymerization of Regulatory Subunits as Revealed by Inherited Carney Complex Mutations

3.1 Author's Preface

The presented work in this chapter along with the next chapter data is part of an ongoing manuscript. Authors and their affiliation are as follow:

"Naeimeh Jafari[1], Jason Del Rio[2], Madoka Akimoto[1], Jung Ah Byun[3], Stephen Boulton[3], Kody Moleschi[1], Yousif Al Sayyed[1], Pascale Swanson[3], Jinfeng Huang[1], Karla Martinez Pomier[1], Chi Lee, Jian Wu[2], Susan S. Taylor[2,4], Giuseppe Melacini[1,3*]

[1]Department of Chemistry and Chemical Biology, McMaster University, 1280 Main St. W. Hamilton, Canada; [2]Department Pharmacology, University of California San Diego, La Jolla, CA 92093-0653, USA; [3]Department of Biochemistry and Biomedical Sciences, McMaster University, 1280 Main St. W. Hamilton, Canada; [4]Departments of Chemistry and Biochemistry, University of California San Diego, La Jolla, CA 92093-0653, USA"

I acquired most of the experiments of the manuscript and analyzed the data. Jason Del Rio acquired and analyzed the crystal structure of full-length A211D R1α with support from Dr. Jian Wu. Jung Ah Byun acquired one domain urea unfolding data with support from Kody Moleschi. Stephen Boulton, Yousif Al Sayyed, Pascale Swanson, Jinfeng Huang, Karla Martinez Pomier, and Chi Lee helped for plasmid preparation and protein purification and we had useful discussion. I designed the research with Dr. Susan S. Taylor and Dr. Giuseppe Melacini. I co-wrote the manuscript with Dr. Madoka Akimoto, Dr. Susan S. Taylor, and Dr. Giuseppe Melacini.

3.1.1 Acknowledgements

We are grateful to Marcia Reid for assistance with the acquisition of TEM images and, together with Dr. R. Maillard, Dr. G. Veglia, and Dr. Rashik Ahmed for helpful discussions.

3.1.2 Funding

Funding was provided by the Canadian Institutes of Health Research Grant 389522 (to G. M.), the Natural Sciences and Engineering Research Council of Canada Grant RGPIN-2019-05990 (to G. M.) and NIH grant R35-GM130389 (to S.S.T.).

3.1 Abstract

Familial mutations of the PKA R1α regulatory subunit lead to a generalized predisposition for a wide range of tumors, from pituitary adenomas, to pancreatic and liver cancers, commonly referred to as Carney complex (CNC). CNC mutations are known to cause over-activation of PKA, but the molecular mechanisms underlying such kinase over-activity are not fully understood in the context of the canonical cAMP-dependent activation of PKA. Here, we show that polymerization-induced sequestration of R1α from the catalytic subunit of PKA (C) is a viable mechanism of PKA activation and explains the CNC phenotype. Our investigations focused on the comparative analyses at the level of unfolding, aggregation, and kinase inhibition profiles of wt PKA R1α, the A211D and G287W CNC mutants and the cognate acrodysostosis type 1 (ACRDYS1) mutations A211T and G287E. The latter exhibit a phenotype opposite to CNC with sub-optimal PKA activation compared to wt. Overall, our results show that CNC mutations do not perturb only the classical cAMP-dependent allosteric activation pathway of PKA, but they also amplify significantly more than the cognate ACRDYS1 mutations non-classical and previously unappreciated activation pathways, such as polymerization-induced losses of the PKA R1α inhibitory function.

3.2 Significance Statement

Autosomal dominant mutations in one of the most ubiquitous isoforms of the inhibitory subunit (R1α) of Protein Kinase A (PKA) are linked to a generalized tumour predisposition, referred to as Carney Complex (CNC). The molecular phenotype of CNC mutants is PKA over-activation. However, explaining PKA over-activation remains an unmet challenge for some of the most harmful CNC mutants, which are expressed and exhibit significantly reduced affinity for the cAMP activator but not for the PKA catalytic subunit (C). Here, we address this challenge by proposing a new mechanism of PKA activation, distinct from the classical cAMP-dependent dissociation of the R_2:C_2 complex, and based on polymerization of R1α into assemblies which are incompetent to inhibit PKA C.

3.3 Introduction

Protein Kinase A (PKA) plays a central role in how cells respond to multiple G-protein-coupled receptor (GPCR)-binding hormones, such as thyrotropin or the parathyroid hormone (1, 2). The physiological responses controlled by PKA range from metabolic regulation to cellular differentiation and proliferation (3, 4). PKA includes catalytic and regulatory subunits denoted here as C and R, respectively (4). Under resting conditions, C is inhibited by the R_2 dimer through the formation of a stable holoenzyme complex (R_2C_2). Upon cellular stimulation and activation of adenylyl cyclase by GPCRs, cAMP levels increase sufficiently for cAMP to bind the tandem cAMP-binding domains of R (CBD-A and B; Figure 3.1) and release C, which in turn phosphorylates downstream substrate that control a wide array of signaling pathways (4, 5).

Autosomal dominant inherited mutations in the 1α isoform of PKA R have been associated with Type 1 Acrodysostosis (ACRDYS1) or the Carney complex (CNC) (1, 6). ACRDYS1 is a severe skeletal dysplasia leading to defects in the development of facial, finger and toe bones as well as dwarfism (1, 2). CNC refers to a multiple endocrine neoplasia often linked to a generalized predisposition for tumors, including pituitary and breast ductal adenoma, heart and breast myxomas, adrenocortical tumors, pancreatic and liver cancers as well as skin tumors characterized by spotty pigmentation (6–9). ACRDYS1 arises from hormonal resistance caused by an impaired PKA R1α response to cAMP (1, 2). In fact, most ACRDYS1 PKA R1α mutations are found in the vicinity of the cAMP-binding site of CBD-B. Since CBD-B functions as a ‘gate-keeper’ for binding of cAMP also to CBD-A, these ACRDYS1 mutants exhibit elevated activation constants, which explain the decrease sensitivity to cAMP and lower degree of C activation in ACRDYS1 *vs.* wt PKA (1, 10, 11).

Unlike ACRDYS1, the CNC pathology reflects increased PKA activity arising from losses of the tumor-suppressor function of PKA R1α (8). Most CNC PKA R1α mutations incur mRNA nonsense-mediated decay (NMD), resulting in PKA R1α haploinsufficiency and over-activation of the PKA C kinase (12, 13). However, the most harmful CNC PKA R1α mutants often escape NMD and result in the expression of defective PKA R1α (13, 14). The majority of CNC PKA R1α mutations not-subject to NMD cluster in CBD-A (Figure 3.1A) (12), which is essential for binding and inhibiting PKA C. Some of these CNC mutants, such as R144S and S145G are located at the inter-protomer interface of the R1α dimer and have been shown to perturb the allosteric response to cAMP. They result in lowered Hill coefficients and activation constants, thus explaining the hypersensitivity to cAMP and the consequent PKA over-activation in these CNC mutations (15). However, for other CNC mutations, such as A211D and G287W (Figure 3.1), the opposite effect is observed (10). The cAMP activation constants of A211D and G287W are significantly higher than those of wt PKA R, while no significant losses are observed in the ability to inhibit PKA C (10). The A211 and G287 CNC mutant sites are of particular interest because of their unique ability to switch from the CNC to the opposite ACRDYS1 phenotype simply by changing the side chains of these residues. Specifically, A211T and G287E are classified as ACRDYS1 mutations, suggesting that the 211 and 287 sites are critical for understanding PKA-linked pathologies. Taken together, these observations indicate that the molecular mechanisms underlying CNC PKA R1α mutations are currently not fully understood, especially in the context of the classical model of cAMP-dependent PKA activation.

Here, we hypothesize that a viable mechanism to explain the CNC phenotype of the A211D and G287W PKA R1α mutations is the activation of PKA C through polymerization-induced losses of the PKA R inhibitory function. Upon partial denaturation, wt PKA R1α tends to aggregate (16). If a CNC mutant is more prone to unfold than wt, either because of reduced cAMP affinity or intrinsic destabilization of R1α (17), it is more likely to polymerize into open-ended assemblies than wt (18). Bioinformatics analyses indicate that PKA R1α aggregates sequester and shield key loci of the inhibitory R:C interface (16), suggesting that PKA R1α aggregation reduces the inhibitory competency of PKA R, thus explaining the PKA C overactivation typical of CNC mutants. In order to test this hypothesis, here we comparatively analyze the unfolding, aggregation and inhibition profiles of wt PKA R1α and the CNC mutants A211D and G287W. We also extend our comparative analyses to the cognate ACRDYS1 mutations A211T and G287E, which, unlike the corresponding CNC mutants, result in PKA over-inhibition. In addition, the ability to compare CNC *vs.* ACRDYS1 mutations of the same residue eliminates possible positional biases from the comparisons.

Unfolding was investigated at progressive degrees of resolution (*i.e.* full-length, domain and residue-resolution) by combining urea unfolding monitored by intrinsic fluorescence, bioinformatics, and hydrogen/deuterium exchange (HDX) monitored by NMR. Aggregation was probed by size-exclusion chromatography (SEC), extrinsic fluorescence using the ThT and ANS fluorophores, NMR, dynamic light scattering (DLS) and transmission electron microscopy (TEM), while PKA C activation was gauged through luminescence-based kinase assays. Our results show that the A211D and G287W CNC mutations unfold the tandem CBDs of PKA R1α more than wt and the cognate ACRDYS1 mutants, leading to correspondingly higher propensities to polymerizes into open-ended assemblies, which are incompetent to inhibit PKA C. Taken together, our data support the hypothesis that PKA R polymerization sequesters R from C, thus defining a non-canonical, yet viable, mechanism for PKA C activation that was not previously appreciated but is relevant for CNC mutations.

3.4 Results

The CNC Mutation A211D Destabilizes the PKA R1α Fold Significantly More than the Cognate ACRDYS1 Mutation A211T. As a first step towards assessing the impact of the A211 mutations on the stability of PKA R1α, we monitored the urea unfolding of wt, A211D and A211T PKA R1α through intrinsic Trp fluorescence (19, 20) (Figure 3.2A). Figure 3.2A shows that both mutants unfold at lower urea concentrations than wt. While the C_m of wt PKA R1α is ~6.4 M under our conditions, the C_m values of the A211T and A211D mutants decrease to ~5.6 M and ~3.2 M, respectively (Figure 3.2A). The urea unfolding data in Figure 3.2A are in agreement with the changes in mutant *vs.* wt stability ($\Delta\Delta G$) computed through the structure-based Eris software (Table S3.1) (21). Positive or negative $\Delta\Delta G$ values indicate that the mutant destabilizes or stabilizes the structure, respectively (21). As shown in Table S3.1, the $\Delta\Delta G$ values computed for the A211D mutant are consistently higher than those calculated for the A211T mutant. This pattern applies irrespective of whether PKA R1α adopts a cAMP- or a C-binding competent structure and regardless of the specific PKA R1α construct utilized as input (Table S3.1). Overall, our unfolding data and computations, consistently show that the CNC A211 mutation causes a loss of folding stability in PKA R1α significantly larger than the cognate ACRDYS1 A211 mutant. However, Figure 3.2A alone is insufficient to establish whether the major destabilization induced by the A211D mutation arises from losses of cAMP binding affinity and/or from an intrinsic destabilization of the PKA R1α structure. In order to better understand the cause of the A211D instability, we further investigated this mutation in the context of a one domain CBD-A construct, PKA R1α (96-244), which can be easily prepared in the apo form and for which apo *vs.* holo unfolding changes more directly reflect 1:1 cAMP binding affinities to the mutated domain. Figure S3.1 shows the urea unfolding profiles of A211D PKA R1α (96-244) in the presence and absence of cAMP. As a control, Figure S1 also includes the urea unfolding profile for the wt PKA R1α (96-244) construct.

In stark contrast to the wt construct, no appreciable changes in folding stability are observed for the A211D mutant upon addition of 500 μM cAMP (Figure S3.1). This observation indicates that the A211D mutations reduces the cAMP affinity for the isolated CBD-A to > ~sub-mM levels, *i.e.* ~five orders of magnitude weaker than the corresponding wt construct. In addition, the A211D mutation significantly destabilizes also apo PKA R1α (96-244) (Figure S3.1). Hence, the decreased stability of the A211D mutant relative to wt arises from dramatic losses of cAMP affinity at CBD-A as well as from an intrinsic destabilization of the CBD-A fold. In order to gain further insight on the nature of this dual loss of stability, we mapped at residue-resolution the effect of the A211 mutations on the structure and solvent accessibility of the PKA R1α CBDs through NMR chemical shifts (Figure 3.3A-F) and NMR monitored hydrogen-deuterium exchange (HDX; Figure 3.2,B-E), respectively.

The A211 Mutations Cause Primarily Local Perturbations of the PKA R1α Ground Folded State, Confined to CBD-A and the CBD-A/B Interface Without Major Changes in the Global Fold. We acquired $^{1}H^{15}N$-HSQC spectra of the wt as well as A211D and A211T PKA R1α (119-379) construct, which spans both tandem CBDs (Figure 3.3A,B). Both mutations lead to significant intensity losses and chemical shift changes (Figure 3.3A,B). Although intensity losses are more pronounced for A211D than for A211T (Figure 3.3A,B), for both mutations the most significant chemical shift changes are local and confined to CBD-A, where A211 is situated, and part of the CBD-A/B interface (Figure 3.3C,D). However, the chemical shifts of the A211 mutants remain overall quite comparable to those of wt (Figure 3.3E,F), suggesting that the ground state conformation of the ensemble sampled by both A211 mutants preserves a global fold similar to wt PKA R1α, in agreement with our Eris predictions (Table S3.1). However, based on the urea unfolding data (Figure 3.2A; Figure S3.1) and the Eris stability predictions, we expect that the A211 mutations should make the unfolded and/or partially unfolded excited states more accessible to PKA R1α. We therefore anticipate the A211 mutants to display different solvent exposure relative to wt. To test this prediction, we examined the solvent accessibility of PKA R1α (119-379) through HDX monitored in real-time at residue-resolution by NMR (Figure 3.2B-E).

The A211D Mutation Increases the Solvent Exposure of Both CBDs More Than the A211T Mutation Under Native Conditions. Due to the limited signal-to-noise ratio exhibited by several peaks in the mutant A211 HSQC spectra (Figure 3.3A, B), we opted for a semi-quantitative approach to the HDX analysis. We categorized residues in three groups: fully exposed, fully protected residues and those with intermediate exposure, which fall between the extremes of the first two classes (Figure S3.2). Residues without detectable signal beyond the second HSQC acquired after the dead-time of the HDX experiment are defined as fully exposed (Figure S3.2). Fully protected residues are those not subject to appreciable H/D exchange within the HDX experiment time frame ($\leq$ 16 hours; Figure S3.2). The remaining residues were assigned to the intermediate group (Figure S3.2). Based on this categorization (Figure 3.2B), we mapped the results of our HDX experiments for wt, A211D and A211T PKA R1α (119-379) on the structure of the PKA R1α CBDs (Figure 3.2C-E).

Figure 2B-E shows that both A211 mutants results in a loss of fully protected residues (Figure 3.2B), pointing to an overall destabilization of the CBDs with respect to transient global unfolding. However, the changes elicited by the A211T and A211D mutations on the other two HDX classes are clearly distinct (Figure 3.2B). For A211T we observed an increase in the occurrence of residues with intermediate protection (Figure 3.2B), without major changes for the fully exposed category. On the contrary, for A211D we detected a higher frequency of residues with full exposure and losses in the intermediate category (Figure 3.2B). So overall, the solvent exposure appears to increase in the order wt < A211T < A211D, in agreement with the urea unfolding data (Figure 3.2A; Figure S3.1).

The CBD-A domain of the A211D mutant is the main region responsible for the reduction in full and intermediate protection and enhancement in full exposure (Figure 3.2D). However, several CBD-B residues also become more solvent exposed in A211D relative to wt (Figure 3.2D). Hence, the A211D mutation affects solvent exposure in both CBDs. Similarly, in the A211T mutant changes in solvent exposure are observed in both

CBD-A and B (Figure 3.2E). Contrary to A211D, for A211T a mixed pattern is observed (Figure 3.2E), in which changes are not necessarily from more to less protected categories. These results further confirm the increased overall solvent exposure in A211D compared to both A211T and wt PKA R1α. Notably, A211D increases exposure through partial unfolding primarily in CBD-A, including the short αP helix in the Phosphate Binding Cassette (PBC) and the β1 strand (Figure 3.2D), which are aggregation prone motives (Figure S3.3) (16, 22, 23). Therefore, our HDX results suggest that A211D is more likely to aggregate than wt and A211T. To test this hypothesis, we monitored the A211D PKA R1α self-association and amyloid formation through SEC, NMR intensity losses, fluorescence, TEM (Figure 3.4A-F) and DLS (Figure S3.4).

A211D is Significantly More Aggregation Prone than A211T and wt PKA R1α. We monitored the extent of PKA R1α aggregation through multiple techniques. First, the gel filtration elution profiles of wt, A211D and A211T PKA R1α consistently show two distinct peaks at around 44 mL and 68 mL (Figure 3.4A). The first peak corresponds to oligomers larger than 100 kDa, while the second peak corresponds to dimeric PKA R1α (Figure 3.4A). Interestingly, the relative oligomer *vs.* dimer intensity increases ~four-five-fold in A211D *vs.* wt PKA R1α, but remains comparable to wt in A211T (Figure 3.4A). Hence, the A211D mutant is markedly more prone to self-association than wt and A211T even in the absence of heating. To complement this result, we probed the aggregation of PKA R1α through heat induced 1D ^{1}H NMR methyl intensity losses (24–27) (Figure 3.4B). For wt and A211T such losses are limited to ~20 %, but they increase to ~70 % for A211D, confirming the increased aggregation propensity of A211D relative to wt and A211T.

The Probability to Form Cross-β Sheet Containing Oligomers with Exposed Hydrophobic Sites is Higher in A211D Than A211T and wt PKA R1α. To further explore the nature of the aggregates formed by wt, A211D, and A211T PKA R1α, we probed the PKA R1α oligomerization with the ThT and ANS fluorophores, which report on cross-β sheets (24, 28) and hydrophobic exposure (29, 30), respectively (Figure 3.4C,D). ThT fluorescence for wt, A211D, and A211T PKA R1α was recorded during a 14-hour incubation period at 60 ^{o}C (Figure 3.4C), which results in the formation of PKA R1α oligomers with size ≥ 100 nm for both wt and the A211 mutants, as shown by DLS (Figure S3.4B). The dimension of these PKA R1α assemblies is comparable to that of oligomers formed under the same experimental conditions by the prototypical amyloidogenic peptide Aβ (1-40), which serves as positive control (Figure S3.4). In addition, TEM images show that for both wt and the A211 mutants the 14 hours incubation period at 60 °C results in the growth of PKA R1α assemblies (Figure 3.4E-F). It is notable that oligomers are already present prior to heat treatment, as consistently shown by our TEM (Figure 3.4E), DLS (Figure S3.4A) and SEC data (Figure 3.4A). These observations indicate that the ability to polymerize is an intrinsic property of PKA R1α, which is further accelerated through heating.

The comparative analysis of the ThT fluorescence time-profiles for wt, A211D, and A211T PKA R1α reveals that A211D not only exhibits the highest cross-β sheet content, but also the shortest lag time (Figure 3.4C). Wt R1α also showed a rise in ThT signal over time (16), but, contrary to the A211 mutants, only to levels lower than the control peptide Aβ (1-40). Furthermore, wt exhibits the longest lag time among all samples tested (Figure 3.4C). The ThT profile of A211T is intermediate between those of Aβ (1-40) and A211D (Figure 3.4C). Overall, the order of cross-β formation propensity as gauged based on the lag time duration and the maximum ThT fluorescence is A211D > A211T > wt. A similar ranking order is observed also based on the heat-induced ANS fluorescence enhancements (Figure 3.4D), indicating that A211D increases the exposure of hydrophobic surfaces more than A211T. Taken together these results indicate that A211D exhibits a higher propensity than A211T to form cross-β sheet aggregates with exposed hydrophobic sites.

Polymerization of PKA R1α Shields Sites Mediating Inhibitory Interactions with PKA C. Interestingly, some of the most aggregation prone sites in PKA R1α, such as the αP helix in CBD-A (Figure S3.3) (16, 22, 23, 31, 32), are also critical sites in the PKA R:C binding interface (5). Based on this notion, we hypothesize that PKA R polymerization, which is amplified in the CNC mutant, reduces the PKA C inhibition competency of PKA R. To test this hypothesis and gauge the kinase inhibition competency of the assemblies promoted by the CNC mutant, we reverted to kinase assays (Figure 3.4G,H).

The A211D Aggregation Causes a Loss of PKA C Inhibition. PKA C kinase inhibition was probed for both wt and A211D full-length PKA R1α (Figure 3.4G,H). The wt PKA R1α served as our positive control. Prior to polymerization, both wt and A211D

PKA R1α inhibit the kinase activity of PKA C in a dose dependent manner (Figure 3.4G). Similar to wt, the A211D PKA R1α mutant remains competent to inhibit PKA C if incubated at 4 ^{o}C for up to eight hours (Figure 3.4H). However, upon incubation at 37 ^{o}C, the inhibitory competency of A211D is nearly fully lost within two hours (Figure 3.4H), while WT only lost approximately 25 % of its inhibitory potency within the same timeframe (Figure 3.4H). These results indicate that the heat-induced A211D assemblies cause a loss of inhibitory function in PKA R1α. Such loss is not simply caused by precipitation because UV absorbance at 280 nm indicates that the protein is still present in solution even after heat treatment. These data show that polymerization suppresses the inhibitor potency of A211D PKA R1α, suggesting a viable mechanism to explain the kinase over-activation typical of this CNC mutant. As a first step towards checking whether such mechanism of PKA C over-activation through mutation-induced PKA R1α polymerization applies also to other CNC mutants, we extended a similar comparative analysis of unfolding, aggregation and kinase inhibition to the CNC G287W mutant (Figure S3.6-S3.9; Table S3.4). Unlike A211D, the G287W mutation is situated in CBD-B (Figure 3.1), but similar to A211D it is paired to a cognate ACRDYS1 mutation at the same site (G287E), which serves as a benchmark term of comparison.

3.5 Discussion

PKA C Activation by PKA R Polymerization as a Viable Mechanism for CNC Mutations. The comparative analysis of the unfolding, aggregation and kinase inhibition profiles for wt PKA R1α and the CNC/ACRDYS1 mutant pair A211D/T reveals a previously unappreciated pathway for PKA C activation distinct from the classical allosteric cAMP-dependent dissociation of the R_2:C_2 complex, *i.e.* kinase activation through polymerization-induced losses of PKA R inhibitory function, as schematically summarized in Figure 5. The CNC mutations investigated here promote solvent exposure by lowering the binding affinity for cAMP and/or the free energy of unfolding of apo R (Figure 3.5, black vertical arrows), as consistently shown by CNC *vs.* wt enhancements in activation constants (10), urea unfolding (Figure 3.2A; Figure S3.1), computations (Table S3.1; Table S3.4), and HDX NMR (Figure 3.2B-E; Figure S3.2, and S3.7).

The HDX data show that unfolding is not confined to the CBD where the CNC mutation is located but extends also to the other CBD. The pervasive unfolding caused by the CNC mutations exposes to the solvent PKA R sites that are prone to aggregation, such as the αP helices in the two PBCs, thus promoting the formation of cross-β sheet-rich aggregates of PKA R (Figure 3.5). The propensity to aggregate in the A211D CNC mutant is consistently supported by fluorescence, NMR intensity losses, DLS and TEM (Figure 3.4 and Figure S3.4). Such aggregation of PKA R1α is distinct from degradation or haploinsufficiency altering the PKA R1α levels. The formation of PKA R1α polymers does not necessarily remove PKA R-subunits, but it shields from PKA C critical R1α sites needed to form a stable inhibitory R:C interface. Hence, upon aggregation, the PKA C inhibition competency of PKA R1α is compromised, as confirmed by kinase assays (Figure 3.4H).

The proposed model (Figure 3.5) shows that there are at least two viable pathways to activate PKA, one classical and one non-classical. The classical pathway is the well-known allosteric cAMP-dependent dissociation of the inhibitory R_2:C_2 complex (Figure 3.5, gray shaded area). The non-classical pathway proposed here pertains to the formation of inhibition-incompetent R polymers (Figure 3.5, blue shaded area). While R polymers can be formed also by wt R (Figure 3.4A,B,E, S3.4, S3.9A)(16), the classical activation pathway prevails in wt PKA. However, the non-classical activation pathway becomes more relevant for the CNC R mutants, as a result of the unfolding caused by the CNC mutations. Aggregation upon mutation-induced misfolding is a well-known process and applicable to proteins in general (33). However, here we show that this mechanism not only serves as a PKA C activation pathway, but it is also significantly more pronounced in CNC mutants relative to both wt and cognate ACRDYS1 variants.

The C-subunit stabilizes the R-subunit with respect to unfolding (Figure 3.5), since no major losses in the inhibitory potency of R were previously observed for the A211D and G287W CNC mutations (10). However, in the cell the PKA R-subunits are typically present at concentrations close to μM, in ~one-order of magnitude excess relative to PKA C (34), thus limiting the ability of PKA C to suppress the aggregation of PKA R. Substrate competition is another factor limiting the stabilization of R by C. In general, while it is clear that the *in vitro* conditions don't fully recapitulate cellular complexity, including chaperone binding, ubiquitination and degradation, the PKA C activation by PKA R polymerization model (Figure 3.5) offers a simple yet viable explanation for the over-activation typically reported for the CNC PKA variants relative to both wt and ACRDYS1 mutants. The PKA R1α-polymerization dependent pathway to activate PKA C is not necessarily exclusive, but it may synergetic with the cAMP-dependent activation of PKA C.

Synergies between Classical and Non-Classical PKA C Activation Pathways. The two viable pathways to activate the kinase function of PKA considered here, the canonical allosteric cAMP-dependent dissociation of the inhibitory complex and the non-canonical formation of R polymers (Figure 3.5), are not necessarily mutually exclusive. For example, cAMP maintains sufficient affinity for the non-mutated domain of A211D (10) to preserve largely unaltered the cAMP-dependent allosteric response of CBD-B. While the allosteric conformational transition of CBD-B alone is not sufficient to fully activate PKA C (35), it does significantly prime the R:C interface for dissociation, thus limiting the ability of PKA C to suppress the polymerization of PKA R (Figure 3.5). Hence, synergies are anticipated between the canonical and non-canonical pathways of PKA C activation and such synergies may explain the enhanced supra-basal activation upon stimulation with low cAMP doses in cell extracts expressing the A211D PKA R1α mutant (10).

The non-classical activation of PKA through formation of inhibition incompetent R polymers may be synergetic also with respect to the recently proposed cAMP compartmentalization through liquid-liquid phase separation (LLPS) of PKA R1α in crowded physiological conditions (36). Such PKA R1α condensates not only act as dynamic “sponges” that compartmentalize cAMP, but they also increase the local PKA R1α concentration. The increased PKA R1α levels in these dense droplets may provide additional pathways for PKA R1α fibril formation, which are alternative but nonexclusive to those that rely on nucleation in dilute conditions (37). Fibril formation causes losses of cAMP-sequestering R1α puncta, which in turn decreases cAMP buffering and compartmentalization. Loss of cAMP compartmentalization lead to spatial dysregulation of cAMP/PKA signaling, which is known to favor tumorigenesis (36), a phenotype also consistent with the Carney complex.

Multiple Concurrent Pathways of PKA C Activation in CNC. Although the activation of PKA C by PKA R polymerization appears to play a significant role for both CNC mutations studied here in spite of their clearly different locations (Figure 1), it is clear that this mechanism is not the only viable explanation for all CNC mutations escaping NMD. Alternative models may apply to other CNC mutants different from those investigated here. For example, the PKA R1α S145G and R144S CNC mutations have been proposed to perturb quaternary interactions, resulting in less cooperative cAMP-dependent activation and lower EC_{50} cAMP concentrations compared to wt PKA (15). The enhanced sensitivity to cAMP of the S145G and R144S CNC mutants is consistent with the PKA over-activation phenotype typical of CNC. However, poor solubility was reported for the S145N mutant (15), suggesting that PKA C activation by PKA R aggregation may play a role also for this CNC mutation. In addition, mutation-induced unfolding of CBD-A is more effective in destabilizing CBD-B than mutation-induced unfolding of CBD-B is in destabilizing CBD-A (38). This notion may explain, in the context of the proposed non-classical mechanism of PKA C activation by PKA R aggregation, why the majority of CNC PKA R1α mutations are found in CBD-A (13).

These conclusions highlight the importance of considering multiple concurrent mechanisms even when explaining the same disease related mutation. Furthermore, additional layers of complexity may need to be considered, as PKA R1α serves as a versatile sensor of specific sub-cellular metabolic, proteomic and redox environments (35). Nevertheless, the simple model of non-classical PKA C activation by PKA R polymerization proposed here (Figure 3.5) offers a viable mechanicistic explanation to reconcile the apparent discrepancy between the PKA C overactivation phenotype of CNC mutants and the decreased cAMP sensitivity of key CNC PKA R1α mutants.

3.6 Materials and Methods

Protein purification. Mutants were prepared by site-directed mutagenesis. All constructs were transformed in BL21(DE3) cells and overexpressed in LB broth for unlabeled 1-379 bPKA R1α constructs, and in ^{15}N-M9 media for uniformly ^{15}N-labeled 119-379 and 96-244 bPKA R1α constructs. Expression and purification were implemented based on previously published protocols (38–42). Further details are available as Supplementary Information.

Urea Unfolding. The assay was prepared in buffer C (50 mM MOPS buffer pH 7.0, 100 mM NaCl, 0.5 mM EDTA, 5 mM DTT) with 5 μM of the PKA R1α 1-379 or 96-244 construct and with or without100-fold excess of cAMP. The protein samples were incubated for three hours at room temperature with urea concentrations increasing from 0 to 8 M. Upon excitation at 293 nm, tryptophan emission was checked at 305-450 nm using a BioTek Cytation5 microplate reader. Unfolding was tracked by the ratio of fluorescence intensity at 353 nm / 340 nm and the fraction of unfolded protein as $X_U=(R-R_N)/(R_U-R_N)$, where R is the observed intensity's ratio at each urea concentration, and R_N is the R value of the fold protein at zero urea concentration, and R_U is the R value at 8 M urea concentration. The unfolding assays were performed in triplicate. Errors were estimated based on standard deviations at plateau or between triplicates

NMR Experiments. All NMR experiments were implemented on Bruker AV700 spectrometer. 1D ^{1}H NMR spectra for 8 μM R1α (1-379) were acquired at 298K in 20 mM phosphate buffer pH 7.4, 50 mM NaCl, 100 % D_2O in the presence of 80 μM excess cAMP with a spectral width of 16.23 ppm and 16K points. The repetition delay was 1 s. The number of scans was 512. Spectra were processed with a line broadening of 3.0 Hz. After 90 minutes of incubation at 60 °C (referred to here as mild heat treatment), 1D ^{1}H NMR spectra were reacquired. Unless otherwise specified, the ^{1}H,^{15}N-HSQC spectra of 100-200 μM R1α (119-379) were acquired in buffer D (50 mM MES buffer, pH 6.5, 100 mM NaCl, 2 mM EGTA, 2 mM EDTA, and 5 mM DTT) with 10 % D_2O and 0.7-1.2 mM excess cAMP at 306 K using 1024 and 128 complex t_2 and t_1 points, respectively, 8 scans and a 1.0 s recycle delay. The acquisition time was about 10 minutes for each HSQC. The H/D exchange samples were prepared based on previously published protocols (38). The H/D exchange buffer was the same as the HSQC buffer, but was prepared in 99% D_2O and 0.7 mM cAMP. The R1α (119-379) concentrations for the H/D exchange experiments were in the 140-260 μM range. The dead time for H/D exchange experiments was ~25 ± 5 minutes. The presence of excess cAMP and protein was monitored by 1D ^{1}H NMR spectra interleaved between the acquisition of the HSQC spectra for monitoring H/D exchange.

ThT and ANS Fluorescence, DLS, and TEM Data Acquisition. All the fluorescence data were acquired using BioTek Cytation5 plate reader. For these experiments we prepared 8 μM R1α (1-379) with ten-fold excess cAMP in buffer C with either 50 μM Thioflavin (ThT) or 200 μM 1-Anilino-8-Napthalene Sulfonate (ANS). The ANS fluorescence spectra were first recorded at 298K with excitation at 350 nm and emission range of 400-600 nm. Samples were then heated to 60 °C and the ThT fluorescence was monitored with excitation at 440 nm and emission at 482 nm every five minutes for a total of 14 hours. After 14 hours of incubation at 60 °C (referred to here as heat treatment), the ANS fluorescence spectra were re-acquired and the initial ANS fluorescence spectra subtracted. Triplicates spectra were acquired for each A211 mutant. For the G287 mutants, the error for the ThT fluorescence was assessed as the standard deviation of ten data points recorded at the end of the 13 hours and 20 minutes incubation period at 60 °C, while the error for the ANS fluorescence was computed as the standard error of two replicates. DLS data were acquired using the same sample utilized for the ThT experiments after 1:2 dilution with buffer C. Prior to DLS measurements, samples were centrifuged at 13,000 rpm for ten minutes. A Malvern ZEN3600 – Zetasizer Nano ZS with 1.5 mL cuvettes a 1 cm pathway was used for DLS data acquisition at 298K. The DLS profiles are the average of three technical replicates. The samples for the TEM images were prepared according to the same protocol used for the ThT experiments followed by 3:16 dilution with ultrapure water. 5 μL aliquots were loaded on carbon coated grids and after two minutes of incubation, the grids were washed with 100 μL ultrapure water and negatively stained with 1 % uranyl acetate for one minute. The TEM images were acquired at 80 kV on a JEOL 1200EX TEMSCAN. Negative control samples for DLS and TEM were not subject to heat treatment but incubated at 4 °C and contained 8 μM R1α (1–379) wt and mutant proteins with ten-fold excess cAMP.

PKA Inhibition Assay. The activation of bovine heart C-subunit PKA (Sigma-Aldrich P2645) was measured through the Kinase-Glo luminescent assay (Promega). After 30-minute incubation at room temperature of 4 nM C-subunit in the presence of 0-60 nM R1α (1-379), we added 4 µM ATP and 5 µM Kemptide. The final volume of the reaction mixture was 50 µL. The reaction was quenched after an hour incubation at room temperature by the addition of 50 µL of Ultra-Glo Luciferase reagent (Promega). After ten minutes at room temperature, the luminescence was recorded by a BioTek Cytation5 microplate reader. The buffer assay was Tris:HCl 40 mM pH 7.5, BSA 0.1 mg/ml, and $MgCl_2$ 20 mM and three biological replicates were acquired. Errors were estimated based on standard deviations among triplicate measurements. The R1α proteins were prepared by eluting with cGMP as described in the Supplementary Text. Unless otherwise specified, samples with oligomerized R1α were prepared by incubating at 37 °C for 2-8 hours 1 µM of natively folded R1α. Control samples from the same solution of 1 µM natively folded R1α were stored at 4 °C for 2-8 hours. Percentage inhibition was calculated relative to wt R1α at 4 °C for the two hours. Concentrations after incubation were monitored by a NanoDrop™ One/One^C Microvolume UV-Vis Spectrophotometer using three technical replicates.

3.7 References

1. A. Linglart, *et al.*, Recurrent PRKAR1A mutation in acrodysostosis with hormone resistance. *N. Engl. J. Med.* **364**, 2218–2226 (2011).
2. G. Mantovani, F. M. Elli, Multiple hormone resistance and alterations of G-protein-coupled receptors signaling. *Best Pract. Res. Clin. Endocrinol. Metab.* **32**, 141–154 (2018).
3. Y. S. Cho-Chung, S. Pepe, T. Clair, A. O. Budillon, M. Nesterova, cAMP-dependent protein kinase: role in normal and malignant growth. *Crit. Rev. Oncol. Hematol.* **21**, 33–61 (1995).
4. S. S. Taylor, R. Ilouz, P. Zhang, A. P. Kornev, Assembly of allosteric macromolecular switches: lessons from PKA. *Nat. Rev. Mol. cell Biol.* **13**, 646–658 (2012).
5. C. Kim, C. Y. Cheng, S. A. Saldanha, S. S. Taylor, PKA-I holoenzyme structure reveals a mechanism for cAMP-dependent activation. *Cell* **130**, 1032–1043 (2007).
6. L. S. Kirschner, *et al.*, Mutations of the gene encoding the protein kinase A type I-α regulatory subunit in patients with the Carney complex. *Nat. Genet.* **26**, 89–92 (2000).
7. P. Salpea, C. A. Stratakis, Carney complex and McCune Albright syndrome: an overview of clinical manifestations and human molecular genetics. *Mol. Cell. Endocrinol.* **386**, 85–91 (2014).
8. C. Kamilaris, F. Faucz, A. Voutetakis, C. Stratakis, Carney Complex. *Exp. Clin. Endocrinol. Diabetes* **127**, 156–164 (2019).
9. D. N. Carney, *et al.*, Establishment and identification of small cell lung cancer cell lines having classic and variant features. *Cancer Res.* **45**, 2913–2923 (1985).
10. Y. Rhayem, *et al.*, Functional characterization of PRKAR1A mutations reveals a unique molecular mechanism causing acrodysostosis but multiple mechanisms causing Carney complex. *J. Biol. Chem.* **290**, 27816–27828 (2015).
11. J. G. H. Bruystens, *et al.*, Structure of a PKA RIα recurrent acrodysostosis mutant explains defective cAMP-dependent activation. *J. Mol. Biol.* **428**, 4890–4904 (2016).
12. A. Horvath, *et al.*, Mutations and polymorphisms in the gene encoding regulatory subunit type 1-alpha of protein kinase A (PRKAR1A): an update. *Hum. Mutat.* **31**, 369–379 (2010).
13. A. Rothenbuhler, C. A. Stratakis, Clinical and molecular genetics of Carney complex. *Best Pract. Res. Clin. Endocrinol. Metab.* **24**, 389–399 (2010).
14. E. L. Greene, *et al.*, In vitro functional studies of naturally occurring pathogenic PRKAR1A mutations that are not subject to nonsense mRNA decay. *Hum. Mutat.* **29**,

633–639 (2008).

15. J. G. H. Bruystens, *et al.*, PKA RIα homodimer structure reveals an intermolecular interface with implications for cooperative cAMP binding and Carney complex disease. *Structure* **22**, 59–69 (2014).

16. K. K. Dao, *et al.*, The regulatory subunit of PKA-I remains partially structured and undergoes β-aggregation upon thermal denaturation. *PLoS One* **6**, e17602 (2011).

17. R. Das, M. Abu-Abed, G. Melacini, Mapping allostery through equilibrium perturbation NMR spectroscopy. *J. Am. Chem. Soc.* **128**, 8406–8407 (2006).

18. K. W. Tipping, P. van Oosten-Hawle, E. W. Hewitt, S. E. Radford, Amyloid fibres: inert end-stage aggregates or key players in disease? *Trends Biochem. Sci.* **40**, 719–727 (2015).

19. D. A. Leon, J. M. Canaves, S. S. Taylor, Probing the multidomain structure of the type I regulatory subunit of cAMP-dependent protein kinase using mutational analysis: role and environment of endogenous tryptophans. *Biochemistry* **39**, 5662–5671 (2000).

20. J. M. Cànaves, D. A. Leon, S. S. Taylor, Consequences of cAMP-binding site mutations on the structural stability of the type I regulatory subunit of cAMP-dependent protein kinase. *Biochemistry* **39**, 15022–15031 (2000).

21. S. Yin, F. Ding, N. V Dokholyan, Eris: an automated estimator of protein stability. *Nat. Methods* **4**, 466–467 (2007).

22. A.-M. Fernandez-Escamilla, F. Rousseau, J. Schymkowitz, L. Serrano, Prediction of sequence-dependent and mutational effects on the aggregation of peptides and proteins. *Nat. Biotechnol.* **22**, 1302–1306 (2004).

23. R. Linding, J. Schymkowitz, F. Rousseau, F. Diella, L. Serrano, A comparative study of the relationship between protein structure and β-aggregation in globular and intrinsically disordered proteins. *J. Mol. Biol.* **342**, 345–353 (2004).

24. J. Milojevic, A. Raditsis, G. Melacini, Human serum albumin inhibits Aβ fibrillization through a “monomer-competitor” mechanism. *Biophys. J.* **97**, 2585–2594 (2009).

25. J. Milojevic, V. Esposito, R. Das, G. Melacini, Understanding the molecular basis for the inhibition of the Alzheimer’s Aβ-peptide oligomerization by human serum albumin using saturation transfer difference and off-resonance relaxation NMR spectroscopy. *J. Am. Chem. Soc.* **129**, 4282–4290 (2007).

26. M. Algamal, J. Milojevic, N. Jafari, W. Zhang, G. Melacini, Mapping the Interactions between the Alzheimer’s Aβ-peptide and human serum albumin beyond domain resolution. *Biophys. J.* **105**, 1700–1709 (2013).

27. M. Algamal, *et al.*, Atomic-resolution map of the interactions between an amyloid inhibitor protein and amyloid β (Aβ) peptides in the monomer and protofibril states. *J. Biol. Chem.* **292**, 17158–17168 (2017).

28. M. Biancalana, S. Koide, Molecular mechanism of Thioflavin-T binding to amyloid fibrils. *Biochim. Biophys. Acta (BBA)-Proteins Proteomics* **1804**, 1405–1412 (2010).

29. O. K. Gasymov, B. J. Glasgow, ANS fluorescence: potential to augment the identification of the external binding sites of proteins. *Biochim. Biophys. Acta (BBA)-Proteins Proteomics* **1774**, 403–411 (2007).

30. A. J. Weids, S. Ibstedt, M. J. Tamás, C. M. Grant, Distinct stress conditions result in aggregation of proteins with similar properties. *Sci. Rep.* **6**, 24554 (2016).

31. F. Rousseau, J. Schymkowitz, L. Serrano, Protein aggregation and amyloidosis: confusion of the kinds? *Curr. Opin. Struct. Biol.* **16**, 118–126 (2006).

32. O. Conchillo-Solé, *et al.*, AGGRESCAN: a server for the prediction and evaluation of" hot spots" of aggregation in polypeptides. *BMC Bioinformatics* **8**, 65 (2007).

33. H. Garcia-Seisdedos, J. A. Villegas, E. D. Levy, Infinite assembly of folded proteins in evolution, disease, and engineering. *Angew. Chemie Int. Ed.* **58**, 5514–5531 (2019).

34. R. Walker-Gray, F. Stengel, M. G. Gold, Mechanisms for restraining cAMP-dependent protein kinase revealed by subunit quantitation and cross-linking approaches. *Proc. Natl. Acad. Sci.* **114**, 10414–10419 (2017).

35. J. A. Byun, *et al.*, Allosteric pluripotency as revealed by protein kinase A. *Sci. Adv.* **6**, eabb1250 (2020).

36. J. Z. Zhang, *et al.*, Phase separation of a PKA regulatory subunit controls cAMP compartmentation and oncogenic signaling. *Cell* **182**, 1531–1544 (2020).

37. C. Mathieu, R. V Pappu, J. P. Taylor, Beyond aggregation: Pathological phase transitions in neurodegenerative disease. *Science (80-.).* **370**, 56–60 (2020).

38. E. T. McNicholl, R. Das, S. SilDas, S. S. Taylor, G. Melacini, Communication between tandem cAMP binding domains in the regulatory subunit of protein kinase A-Iα as revealed by domain-silencing mutations. *J. Biol. Chem.* **285**, 15523–15537 (2010).

39. R. Das, *et al.*, Dynamically driven ligand selectivity in cyclic nucleotide binding domains. *J. Biol. Chem.* **284**, 23682–23696 (2009).

40. M. Akimoto, *et al.*, Signaling through dynamic linkers as revealed by PKA. *Proc. Natl. Acad. Sci.* **110**, 14231–14236 (2013).

41. K. J. Moleschi, M. Akimoto, G. Melacini, Measurement of state-specific association constants in allosteric sensors through molecular stapling and NMR. *J. Am. Chem. Soc.* **137**, 10777–10785 (2015).

42. M. Akimoto, *et al.*, Mapping the free energy landscape of PKA inhibition and activation: A double-conformational selection model for the tandem cAMP-binding domains of PKA RIα. *PLoS Biol.* **13**, e1002305 (2015).

43. Y. Su, *et al.*, Regulatory subunit of protein kinase A: structure of deletion mutant with cAMP binding domains. *Science (80-.).* **269**, 807–813 (1995).

44. K. K. Frousios, V. A. Iconomidou, C.-M. Karletidi, S. J. Hamodrakas, Amyloidogenic determinants are usually not buried. *BMC Struct. Biol.* **9**, 44 (2009).

45. S. Badireddy, *et al.*, Cyclic AMP analog blocks kinase activation by stabilizing inactive conformation: conformational selection highlights a new concept in allosteric inhibitor design. *Mol. Cell. Proteomics* **10** (2011).

46. T.-W. Lu, *et al.*, Two PKA RIα holoenzyme states define ATP as an isoform-specific orthosteric inhibitor that competes with the allosteric activator, cAMP. *Proc. Natl. Acad. Sci.* **116**, 16347–16356 (2019).

3.8 Figure Captions

Figure 3.1: *The PKA R1α System.* (A) Domain organization of PKA R1α with cAMP-binding domain A (CBD-A)'s secondary structure shown along its sequence. Red/gray areas in the sequence are binding or allosteric hot spots. The black star in CBD-A denotes Ala 211, which is mutated to Asp in CNC and to Thr in ACRDYS1 and in CBD-B denotes Gly 287, which is mutated to Trp in CNC and to Glu in ACRDYS1. In general, non haplo-insufficient CNC and ACRO mutants are indicated in green and red, respectively. (B) Structure of R1α in the cAMP-bound state (dark colors; PDB: 1RGS (43)) and C-subunit-bound state (light colors; PDB:2QCS (5)). CNC and ACRDYS1 mutation sites are highlighted with green and red spheres, while cAMP is shown with black sticks. The N3A and Phosphate Binding Cassette (PBC) are highlighted in red and yellow, respectively, while the rest of CBDs is in cyan. The insets show details of the cAMP-binding sites adjacent to the A211 and G287 mutations, with selected hydrogen bonds and capping interactions highlighted by dashed lines and surfaces.

Figure 3.2: *Destabilization Caused by CNC A211D Mutation on the Full Length and Tandem CBDs PKA RIα Based on the Urea Unfolding Profiles and HDX Monitored by NMR and Crystal Packing Interface.* (A) Urea unfolding profiles of full length PKA RIα. Urea unfolding profile monitored through intrinsic fluorescence for 5 μM of full-length PKA R1α (1-379) in the presence of 100-fold excess cAMP. The color codes are shown in the figure. Both mutants decrease the stability, but the effect of the CNC

mutations is more pronounced than that of the ACRO mutation. The $\Delta_{UF}G^{o}_{H2O}$ unfolding free energies decrease in the order wt > A211T > A211D (*i.e.* the free energy of unfolding extrapolated to pure aqueous buffer for wt, A211T and A211D PKA R1α are $\Delta_{UF}G^{o}_{H2O}$ = 10.7 ± 1.0 kcal/mol, 8.5 ± 0.8 kcal/mol, 5.4 ± 1.1 kcal/mol, respectively). (B-E) Residue-specific solvent exposure as gauged based on H/D exchange monitored by HSQC spectra for the PKA R1α (119-379) construct in the presence of 0.7 mM excess cAMP. Residues are categorized in three groups (Fig. S2): fully exposed, intermediate, and fully protected. The fully exposed residues exchange their backbone amide hydrogen within the first 20 minutes. The fully protected residues do not appreciably exchange during the duration of the H/D experiment (*i.e.* within 16 hours). The intermediate class captures the remaining residues that are neither fully exposed nor fully protected. (B) Frequency of occurrence for each exchange class based on the assigned residues. Vertical arrows show that the fraction of fully exposed residues increases in A211D compared to wt at the expense of losses in the other two classes. The cAMP-bound structure (PDB code: 1RGS (43)) is used for all HDX maps. Color codes are shown in the figure. (C) wt; (D) A211D mutant; (E) A211T mutant. In D and E, residues that are more solvent exposed than wt are marked by black arrows, while residues that are more protected than wt are highlighted by orange arrows. The black box in panel D means that CBD-A is fully solved exposed. Surfaces in panels C-E highlight AmyldPred consensus aggregation prone regions (Fig. S3).

Figure 3.3: *Chemical Shift Map of the Perturbations Caused by CNC and ACRDYS1 A211 Mutations on PKA R1α Tandem CBDs.* (A) Overlay of HSQCs spectra of A211D (blue)

and wt PKA R1α (119-379) (green) in the presence of 2 mM cAMP. (B) As A, but for the A211T mutation. (C) Map of residues with A211D-induced CCS changes above the average plus one standard deviation on the structure of the tandem PKA R1α CBDs bound to cAMP (PDB code: 1RGS (43)). Unassigned residues or broadened beyond detection are highlighted with a gray ribbon. (D) As C, but for the A211T mutation. (E) Correlation between the compounded chemical shifts (CCS) of A211D and wt PKA R1α (119-379) from the spectra in (A). (F) As E, but for the A211T mutation.

Figure 3.4: *Effect of CNC and ACRDYS1 A211 Mutations on PKA R1α Self-Association and Aggregation and Inhibition of the PKA C Kinase Activity*. (A) SEC profiles of full length wt, A211D and A211T PKA R1α prepared as for kinase inhibition assay. The intensity of the dimer peaks are normalized to one. Hence, the relative intensity of the >100 kDa oligomer peak reflects the extent of oligomerization of the PKA R1α dimer. (B) Aggregation probed through 1D ^{1}H NMR methyl intensity losses upon mild heat treatment of 8 μM PKA R1α in the presence of ten-fold excess cAMP. The methyl peak intensity of wt and A211T prior to mild heat treatment are normalized to the methyl intensity of A211D prior to mild heat treatment. The same normalization scaling constant is applied to the intensity of the mildly-heat-treated samples as well. Mild heat treatment leads to a ~70 % intensity loss for A211D, but only ~20% for wt and A211T. (C) Kinetics of cross β-sheet formation as monitored by normalized ThT fluorescence while incubating 8 μM PKA R1α at 60 °C in the presence of ten-fold excess cAMP. We included the ThT fluorescence profile

of the Aβ (1-40) peptide as a positive control for amyloid formation. (D) Difference of ANS fluorescence spectra of 8 μM R1α (1-379) with ten-fold cAMP excess before and after heat treatment. The enhanced ANS fluorescence intensity upon heat treatment points to increased exposure of hydrophobic residues. (E, F) TEM images of WT, A211D, and A211T PKA R1α assemblies in the presence of ten-fold excess cAMP before, before (E) and after (F) heat treatment. PKA R1α oligomers with sizes of the order of 100 nm are already present prior to heat treatment (orange arrows), suggesting that the heat treatment accelerates oligomerization processes intrinsic to PKA R1α. These observations apply to wt PKA R1α as well as the two A211 mutants. (G) Non-polymerized full-length PKA R1α inhibits the kinase activity of PKA C in a dose-dependent manner. This applies to both wt and A211D. (H) The PKA R1α polymers are incompetent to inhibit the kinase activity of PKA C, as shown by kinase inhibition assays of full-length wt and A211D PKA R1α. Thick horizontal lines (shaded rectangles) denote the average (standard deviations) of all time points measured for the A211D or WT samples at each incubation temperature. The inhibitory potency at saturation of PKA C was measured for full-length PKA R1α incubated at 1 μM and 4 ^{o}C or 37 ^{o}C in the time range 2-8 hours. Color codes are indicated in each panel.

Figure 3.5: *Proposed Mechanism for the CNC PKA R1α Mutations A211D and G287W.* Simplified free energy landscape diagram for PKA C activation and inhibition by wt (black) and CNC A211D and G287W (blue) PKA R1α, denoted here simply as R. Abbreviations: A, CBD-A of R; B, CBD-B of R; F, Folded native structure of R; U, ensemble of unfolded

and partially unfolded states of R (a single free energy level is shown to simplify the scheme); $R_{2\ polymer}$, polymerized form of the R dimer; G, Gibbs free energy; $\Delta_{UF}G_{apo}$, unfolding free energy of apo R; $\Delta_{UF}G_{cAMP}$, unfolding free energy of R in the presence of cAMP; $\Delta_{Binding}G_{cAMP}$, free energy of cAMP binding to R; $\Delta_{Binding}G_{C}$, free energy of C binding to R. cAMP is shown as a circle. In the case of the CNC mutants, the circle is deformed to indicate that cAMP occupancies may change compared to wt. The roughened edges in the cartoon of the CNC aggregates (blue) indicate that these assemblies are formed by unfolded or partially unfolded forms of CNC PKA R1α. The specific mutant *vs.* wt free energy differences for apo U and apo F are unknown. In the CNC mutants the $\Delta_{UF}G_{apo}$ and/or $\Delta_{Binding}G_{cAMP}$ free energies decrease relative to wt, resulting in higher populations of unfolded and/or partially unfolded conformers with exposed hydrophobic surfaces and aggregation prone sites. Dashed arrows indicate processes that enhance PKA C activation by R polymerization, which shields loci necessary for C binding and inhibition.

3.9 Figures

Figure 3.1

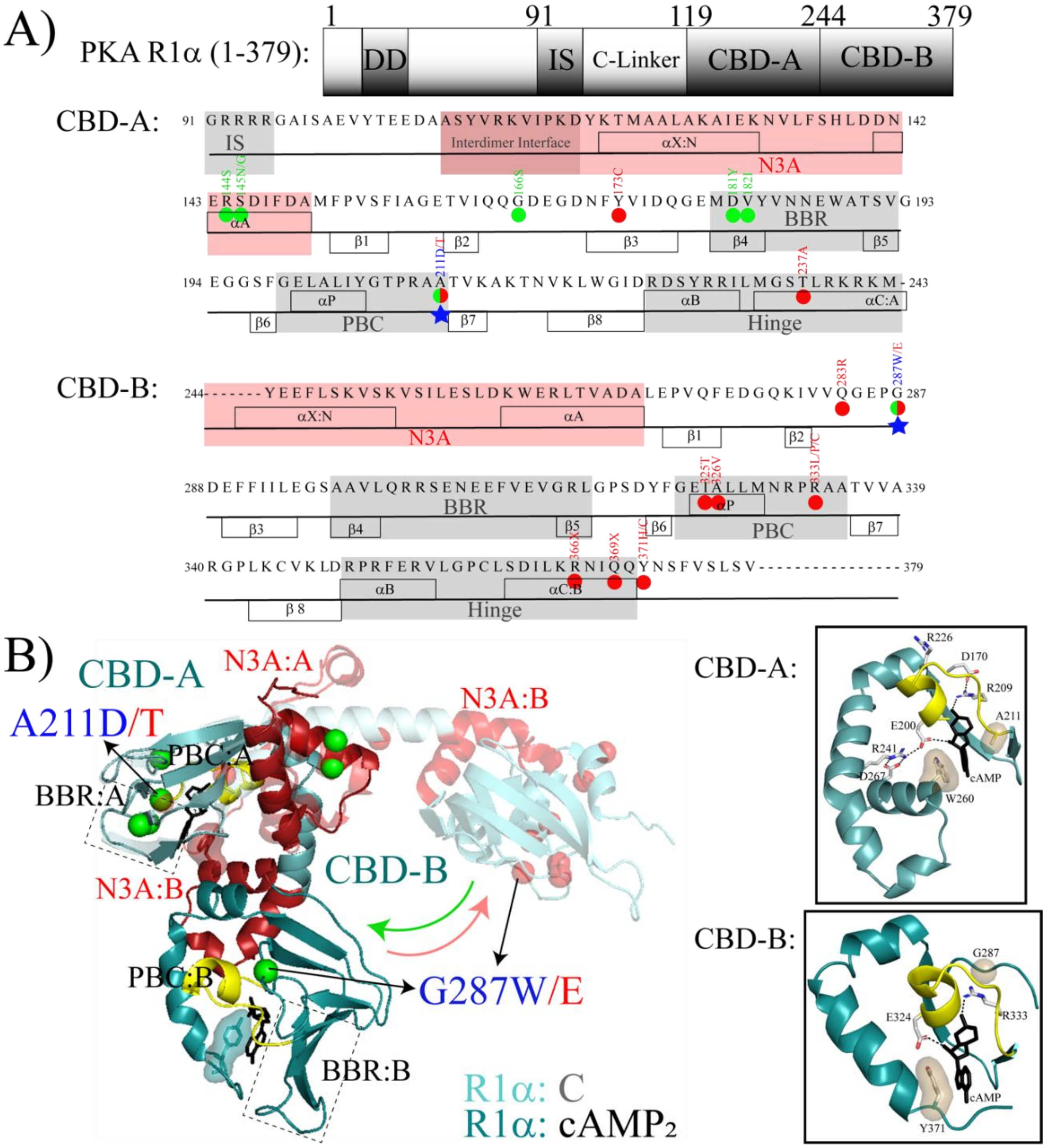

Figure 3.2

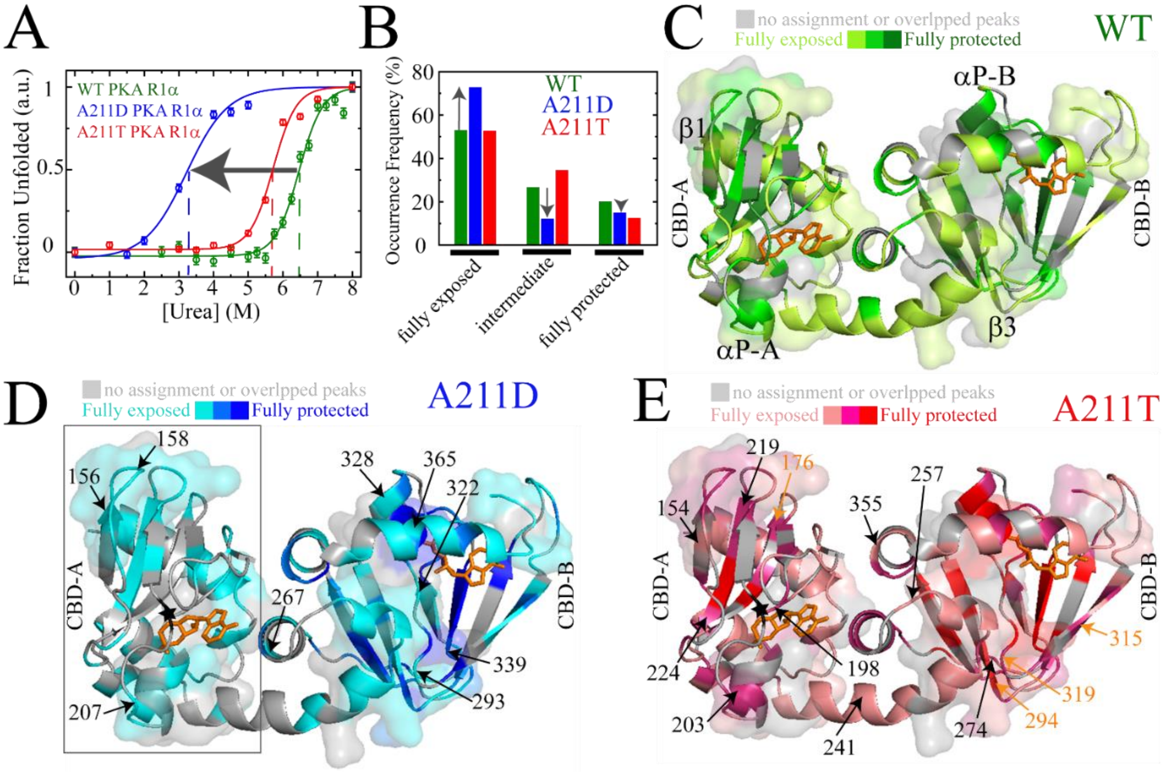
A
WT PKA R1α
A211D PKA R1α
A211T PKA R1α
Fraction Unfolded (a.u.)
1
0.5
0
0 1 2 3 4 5 6 7 8
[Urea] (M)
B
Occurrence Frequency (%)
80
60
40
20
0
WT
A211D
A211T
fully exposed
intermediate
fully protected
C
no assignment or overlpped peaks
Fully exposed
Fully protected
WT
β1
αP-B
CBD-A
CBD-B
αP-A
β3
D
no assignment or overlpped peaks
Fully exposed
Fully protected
A211D
158
156
CBD-A
207
328
365
322
267
339
293
CBD-B
E
no assignment or overlpped peaks
Fully exposed
Fully protected
A211T
219
176
154
CBD-A
224
203
198
241
257
355
274
294
319
315
CBD-B

Figure 3.3

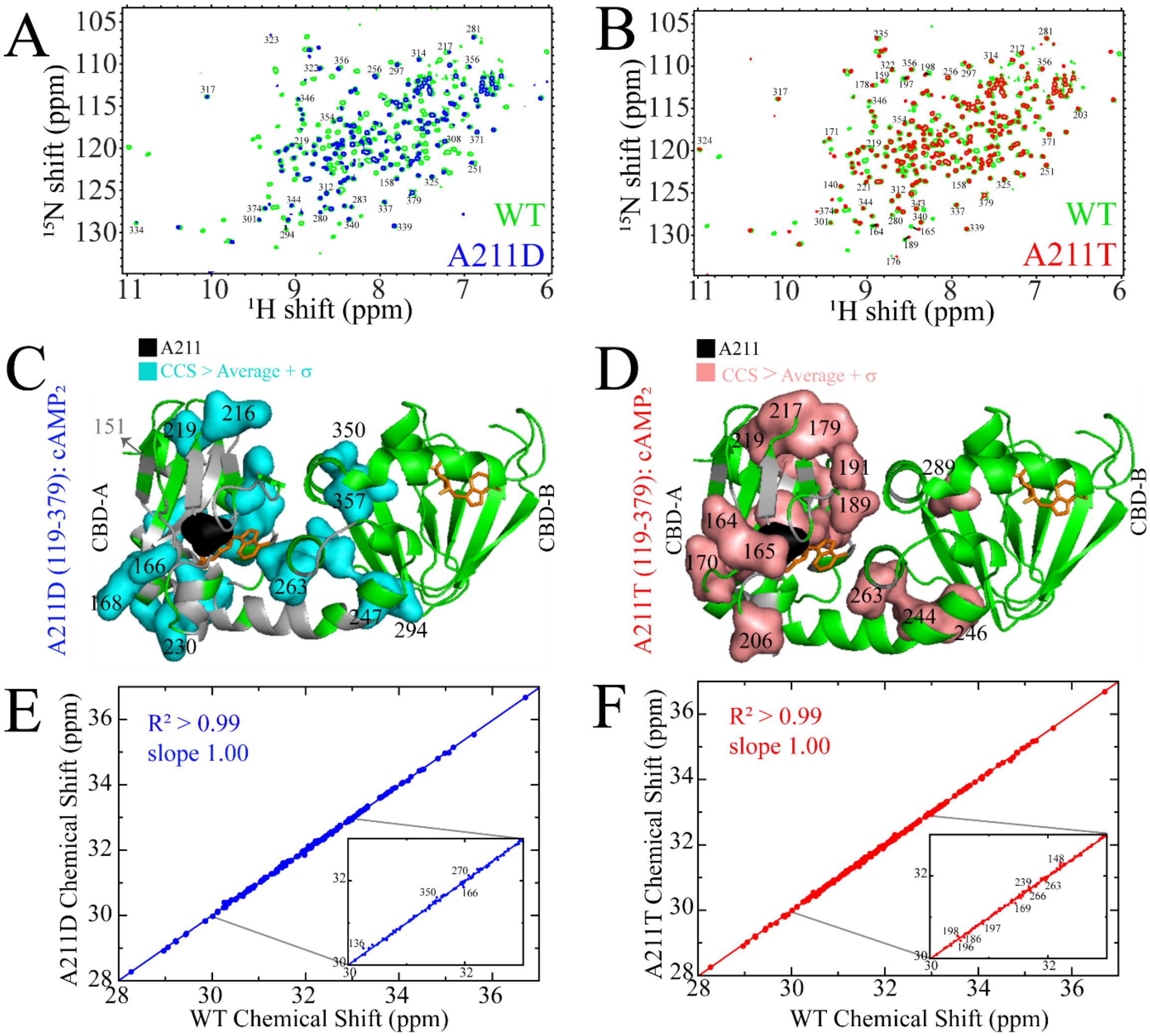
A
B
C
D
E
F
^{15}N shift (ppm)
^{1}H shift (ppm)
WT
A211D
A211T
A211
CCS > Average + σ
A211D (119-379): cAMP$_2$
A211T (119-379): cAMP$_2$
CBD-A
CBD-B
151
219
216
350
357
166
168
263
247
294
230
217
179
191
189
164
165
170
289
263
244
246
206
R² > 0.99
slope 1.00
A211D Chemical Shift (ppm)
A211T Chemical Shift (ppm)
WT Chemical Shift (ppm)

Figure 3.4

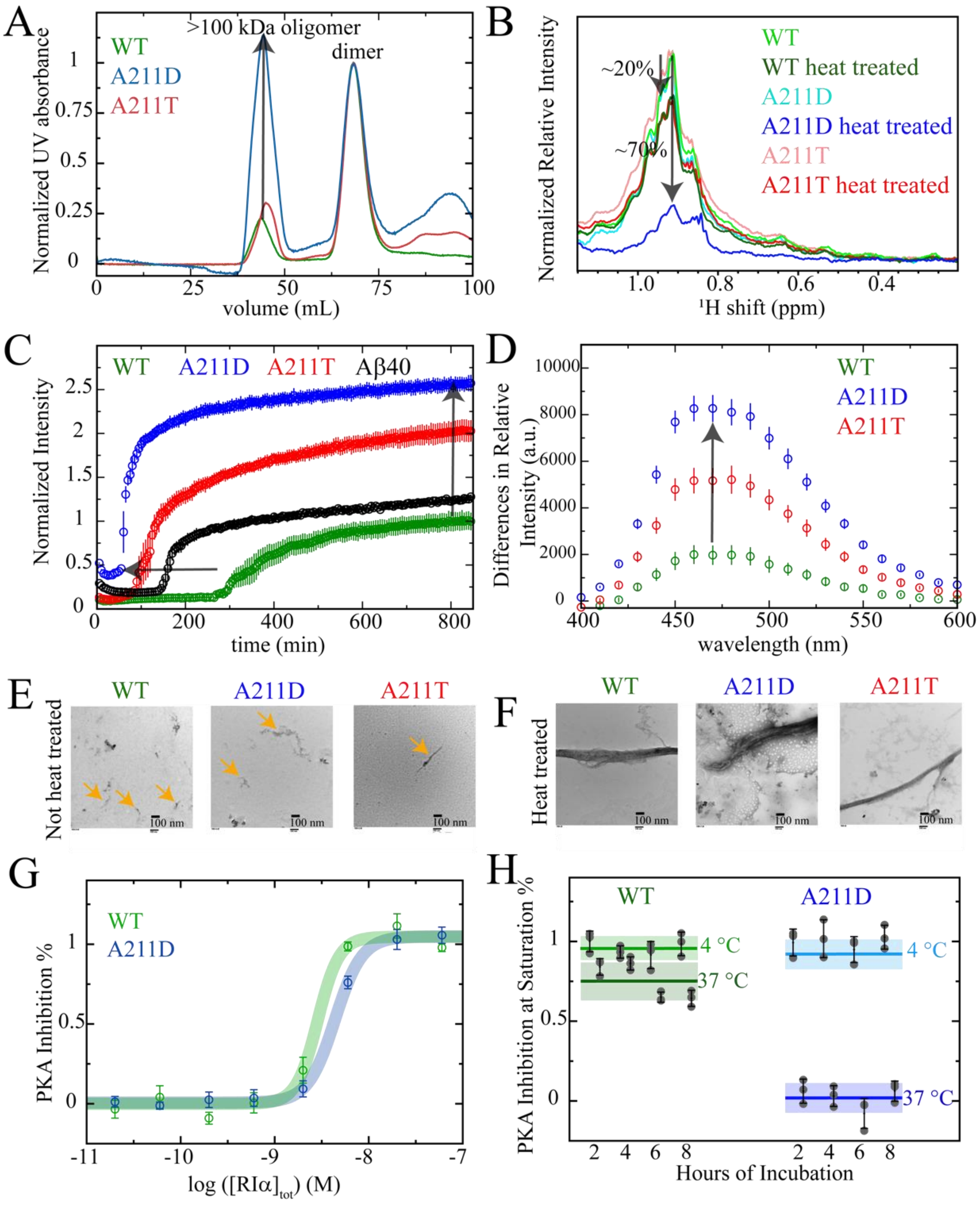
A
>100 kDa oligomer
dimer
WT
A211D
A211T
Normalized UV absorbance
volume (mL)
B
~20%
~70%
WT
WT heat treated
A211D
A211D heat treated
A211T
A211T heat treated
Normalized Relative Intensity
¹H shift (ppm)
C
WT A211D A211T Aβ40
Normalized Intensity
time (min)
D
WT
A211D
A211T
Differences in Relative Intensity (a.u.)
wavelength (nm)
E
Not heat treated
WT
A211D
A211T
100 nm
F
Heat treated
WT
A211D
A211T
100 nm
G
WT
A211D
PKA Inhibition %
log ([RIα]tot) (M)
H
WT
A211D
4 °C
37 °C
PKA Inhibition at Saturation %
Hours of Incubation

Figure 3.5

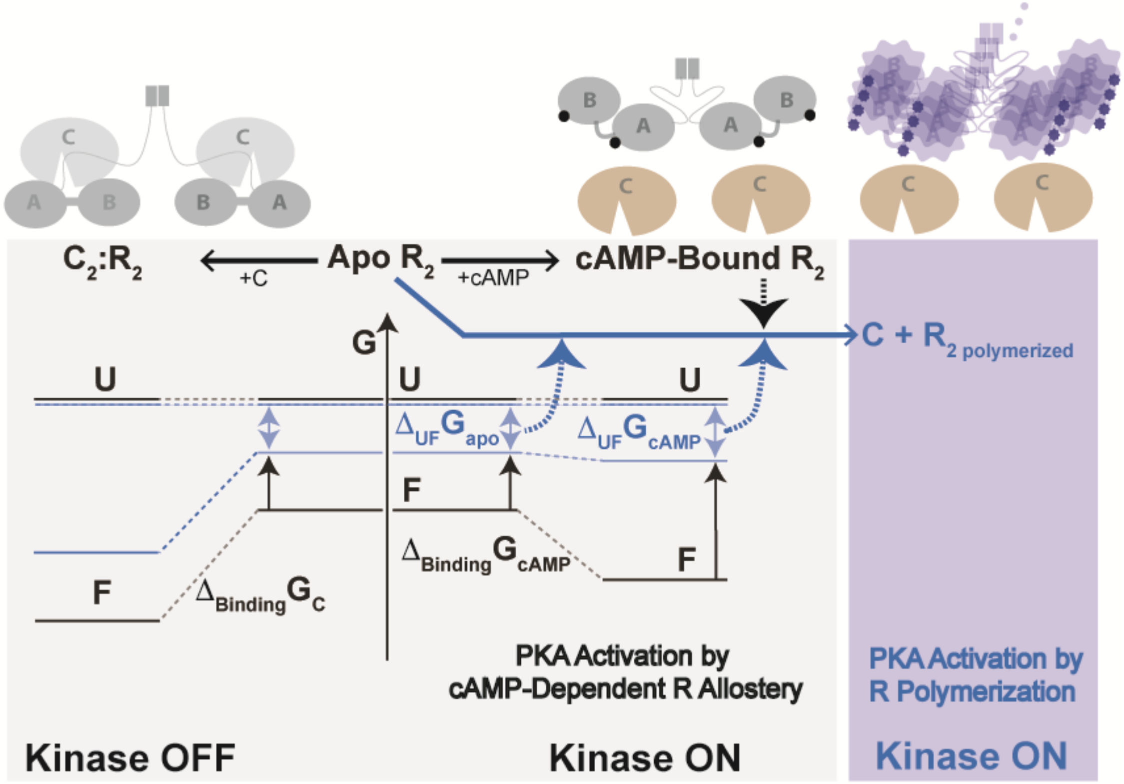
C
A
B
C_2:R_2
+C
Apo R_2
+cAMP
cAMP-Bound R_2
C + $R_{2\ polymerized}$
G
U
F
$\Delta_{UF}G_{apo}$
$\Delta_{UF}G_{cAMP}$
$\Delta_{Binding}G_{C}$
$\Delta_{Binding}G_{cAMP}$
PKA Activation by cAMP-Dependent R Allostery
PKA Activation by R Polymerization
Kinase OFF
Kinase ON
Kinase ON

3.10 Supplementary Material for Non-Classical Protein Kinase A Activation by Polymerization of the PKA R-Subunits as a Mechanism of Inherited Carney Complex Mutations

3.10.1 Supplementary Materials and Methods

Protein Purification. Cells were grown at 37 °C up until the optical density at 600 nm reached 0.6 – 0.7 and then they were induced with 0.5 mM isopropyl-1-thio-β-D-galactopyranoside for 17 hours at 18 °C. Cells were then resuspended in 20 mM MES buffer, pH 6.5 and 100 mM NaCl (buffer A) and disrupted with a protein homogenizer operating at 20 psi. The cell debris was removed through centrifugation (one hour at 14,000 rpm). After gradual fractionation with 40 % ammonium sulfate, the protein was resuspended in buffer A with 2 mM EGTA, 2 mM EDTA, and 5 mM DTT (buffer B) and incubated with the cAMP-Sepharose resin overnight at 4 °C. The resin-bound protein was washed with buffer B, buffer B with 700 mM NaCl, and buffer B at room temperature. Then PKA R1α was eluted by using 25 – 40 mM cAMP or 20 mM cGMP depending of the purpose of the experiment. The cGMP eluted protein was dialysed extensively against 50 mM MOPS buffer pH 7.0, 100 mM NaCl, 0.5 mM EDTA, 5 mM DTT (buffer C) prior to gel filtration. Further purification was obtained through gel filtration on a HiLoad 16/600 Superdex 200 pg column, which had been pre-equilibrated with buffer C for the 1-379 construct and with 50 mM MES buffer, pH 6.5, 100 mM NaCl, 2 mM EGTA, 2 mM EDTA, and 5 mM DTT (buffer D) for the 119-379 constructs. In the SEC profiles, the concentration of A211D and A211T were 0.7 and 1.8, respectively, relative to WT PKA R1α. Purification of the 96-244 PKA R1α fusion construct with a His$_6$-small ubiquitin-related modifier (SUMO) tag was based on nickel-NTA (nitrilotriacetic acid) affinity chromatography with 50 mM MOPS buffer pH 7.0 and 100 mM NaCl. After cleavage of the His$_6$-SUMO tag with a His$_6$-tagged tobacco etch virus (TEV) protease, a second nickel-NTA column was utilized to remove the cleaved His$_6$-SUMO and TEV. The apo 96-244 construct was prepared by unfolding with 8 M urea and refolding by gradual decrease of urea concentration when protein was bound to the first nickel column. Further purification of the 96-244 construct was implemented through gel filtration on a Superdex 75 column pre equilibrated with 50 mM MOPS buffer pH 7.0, 100 mM NaCl, and 10 mM $MgCl_2$. Protein concentrations were measured through the Bradford assay using bovine serum albumin as standard protein.

3.10.2 supplementary Figures and Tables

Figure S 3.1

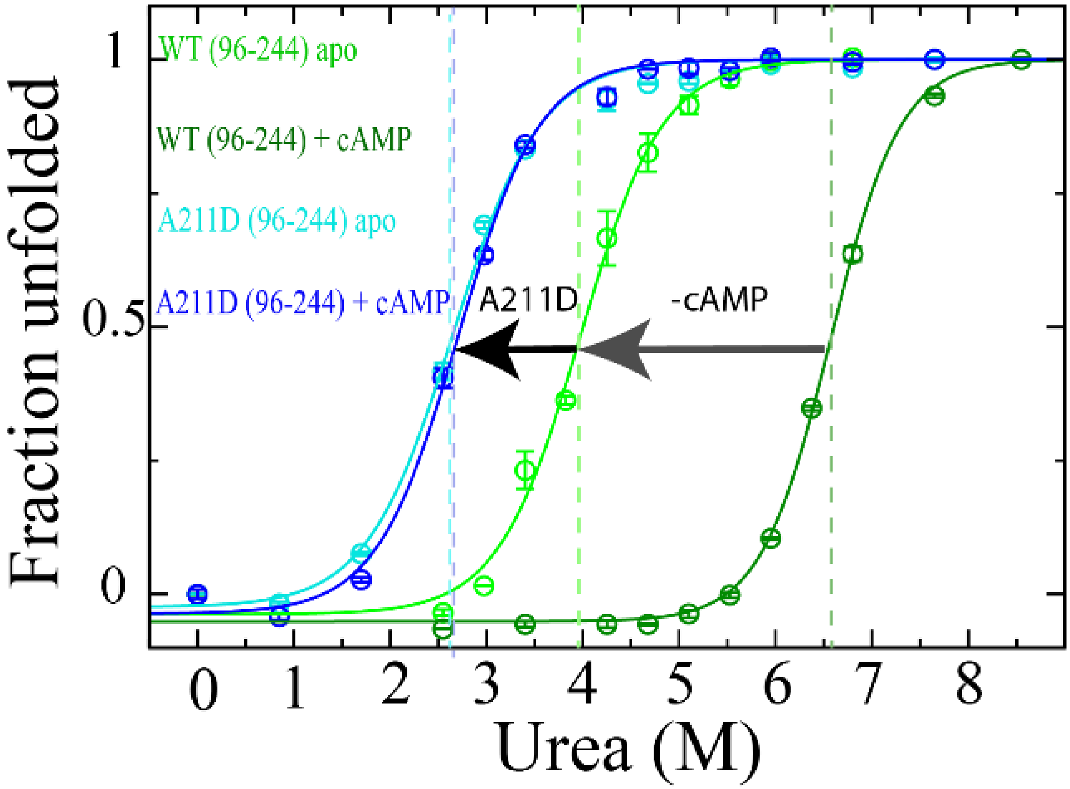

Figure S3.1: *Effect of the A211D Mutation on the Stability of PKA R1α CBD-A.* Urea unfolding profiles of 5 μM wt and A211D PKA R1α (96-244) spanning CBD-A in the absence and presence of 100-fold excess cAMP. The color code is shown in the figure. The vertical dashed lines indicate the urea concentrations needed for half-maximal unfolding (C_m).

Figure S 3.2

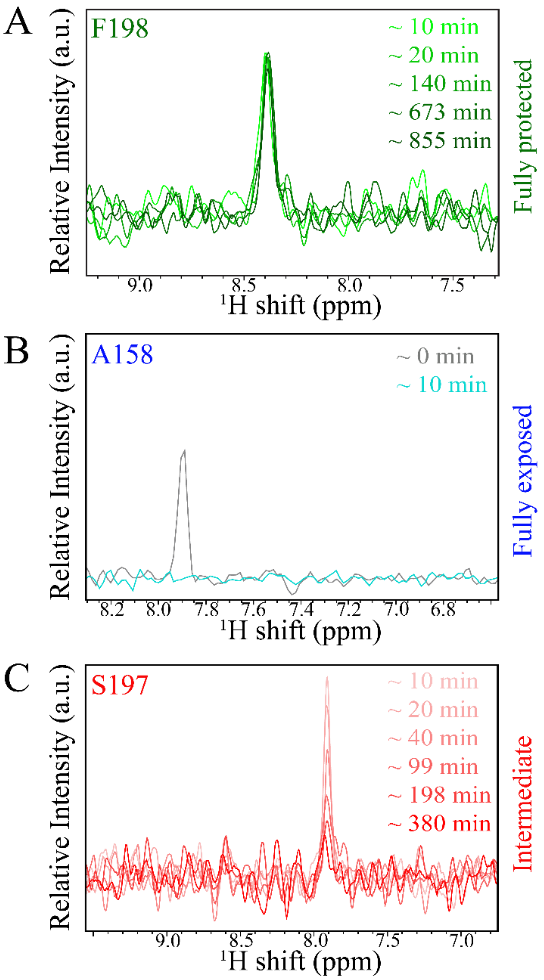

Figure S3.2: 1D cross-sections from peaks in HSQC spectra acquired during the hydrogen-deuterium exchange (HDX) experiments for the wt and the A211 and G287 mutants of PKA R1α (119-379). The panels illustrate representative cases of residues that are fully protected (A) (*e.g.* F198 in wt), fully exposed (B) (*e.g.* A158 in A211D) or subject to intermediate exchange (C) (*e.g.* S197 of A211T). Fully protected residues are defined as those that do not appreciably exchange during the course of the H/D experiments (~14 hours). Fully exposed residues are defined as those for which H/D exchange is complete within the second HSQC acquisition after the dead time of the experiment. Intermediate exchange applies to the residues falling between the fully exposed and fully protected cases. In (B), the first 1D cross-section (gray) is from the control HSQC acquired using the H_2O buffer. In the other panels, lighter shades correspond to 1D cross-section from HSQC spectra recorded at earlier times, while darker shades represent later time points.

Figure S 3.3

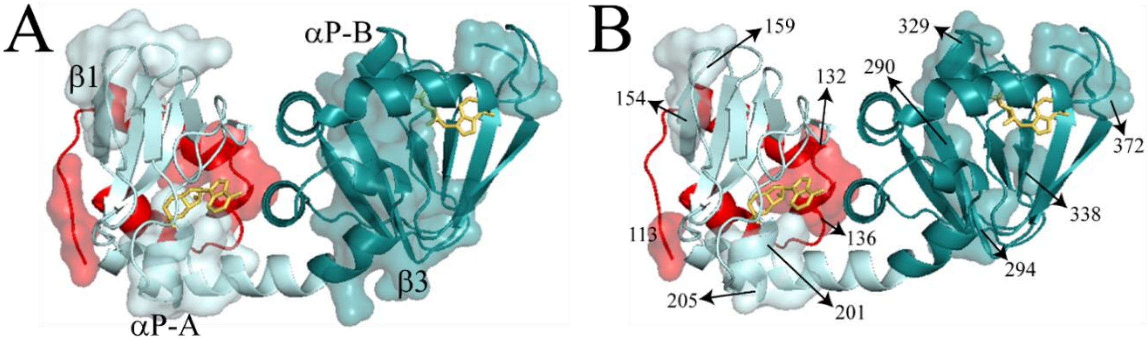

Figure S3.3: Aggregation prone sites of wt PKA R1α based on AGGRESCAN (A) (32) and AmylPred (B) (44) predictions mapped on the surface of the 1RGS structure, in which N3A-A is highlighted in red and the rest of CBD-A is light teal, while CBD-B is in dark teal, and cAMP is shown as yellow sticks. Amylpred reports a consensus map among multiple multiple amyloid propensity prediction algorithms, including not only AGGRESCAN but also Amyloidogenic Pattern, Average Packing Density, Beta-strand contiguity, Hexapeptide Conf. Energy, Pafig, SecStr and TANGO. The AmylPred consensus sites are: 34 (not shown), 112-114, 132-137, 154-159, 201-205, 290-294, 325-329, 337-338 and 372-376. Panel B here shows surfaces similar to those shown in Fig. 2 and Fig. S6 albeit with a different color code and it is included here for the convenience of comparison with panel S3A.

Figure S 3.4

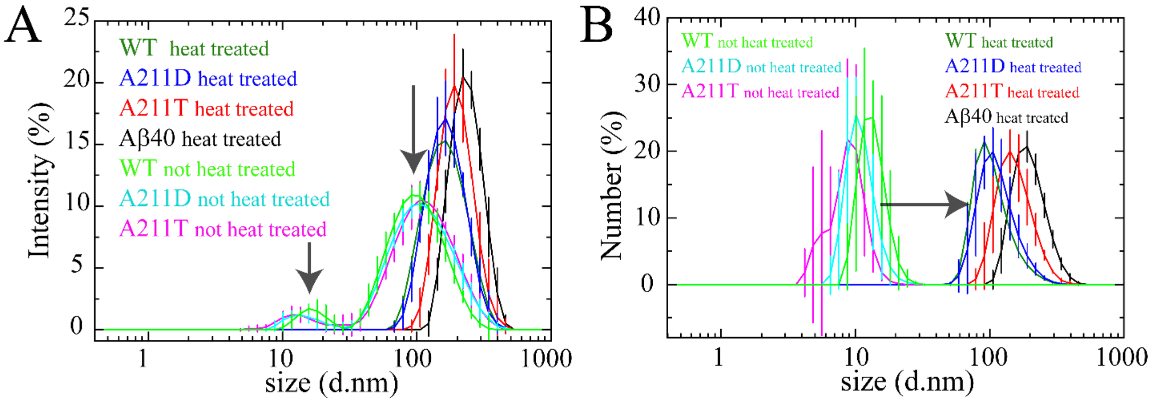

Figure S3.4: *Dynamic Light Scattering (DLS) Profiles of wt, A211D and A211T PKA R1α Before and After Heat Treatment.* (A) Intensity plot for PKA R1α (8 μM, ten-fold cAMP excess). The negative control samples with no heat treatment exhibit two peaks above 10 nm and at 100 nm. However, after heat-treatment, a single peak is observed corresponding to an average size above 100 nm but slightly below the Aβ(1-40) oligomer size, which serves as a positive control. (B) Relative number plot for PKA R1α (8 μM, ten-fold cAMP excess), showing that most particles in the control samples exhibit a size just above 10 nm. Color codes are shown in the panels.

Table S3.1

Table S3.1. *Estimation of A211 Mutants vs. WT PKA R1α Stability (ΔΔG)* [a]

State	**PDB Code Construct**	**Disease**	**Mutant**	**ΔΔG (kcal/mol)** [b]	**RMSD (Å)** [c]
cAMP bound	1RGS [d] 91-379 (43)	CNC	A211D	2.04 [g]	0.515
		ACRDYS1	A211T	-10.50	0.661
	3PNA [d] 91-244 (45)	CNC	A211D	3.77	0.232
		ACRDYS1	A211T	0.60	0.230
C-sub bound	6NO7 [e, f] 1-379 (46)	CNC	A211D	1.12	1.310
		ACRDYS1	A211T	-2.77	1.189
	2QCS [f] 91-379 (5)	CNC	A211D	> 10	0.357
		ACRDYS1	A211T	5.33	0.507

[a] Based on the ERIS software implemented with flexible backbone and pre-relaxation.(21) [b] Positive (negative) ΔΔG (kcal/ mol) values indicate that the mutant destabilizes (stabilizes) the structure. [c] The RMSD of the predicted structure compared to the initial WT structure. [d] The cAMP ligands were removed from the PDB file before submission to ERIS. [e] One R1α protomer were removed from the PDB file utilized as ERIS input. [f] The C-subunit was removed from the PDB file for ERIS input. [g] This value increases to 7.98 kcal/mol for the 1-379 construct in the 4MX3 structure.

3.11 Appendix

Figure S 3.5

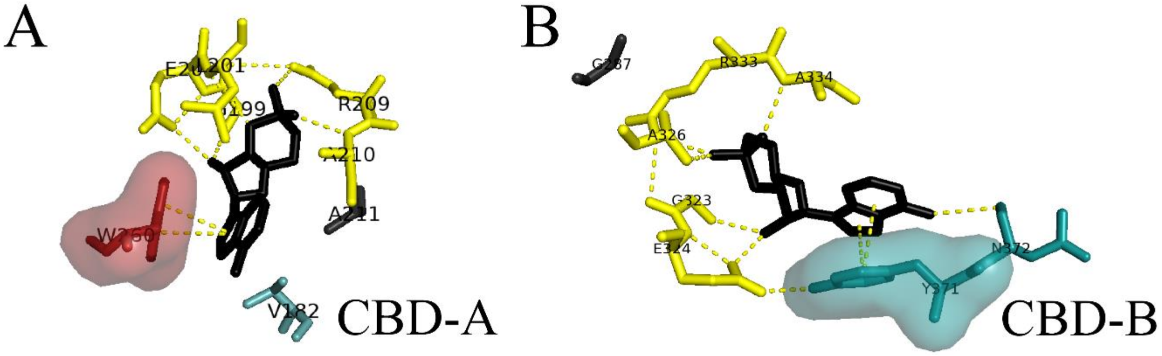

Figure S3.5: The binding pockets of PKA R1α. A and B present CBD-A's and CBD-B's cAMP binding pockets, respectively. Hydrogen bound are shown as dashed lines and pi stacking residues are represented as surfaces.

Figure S 3.6

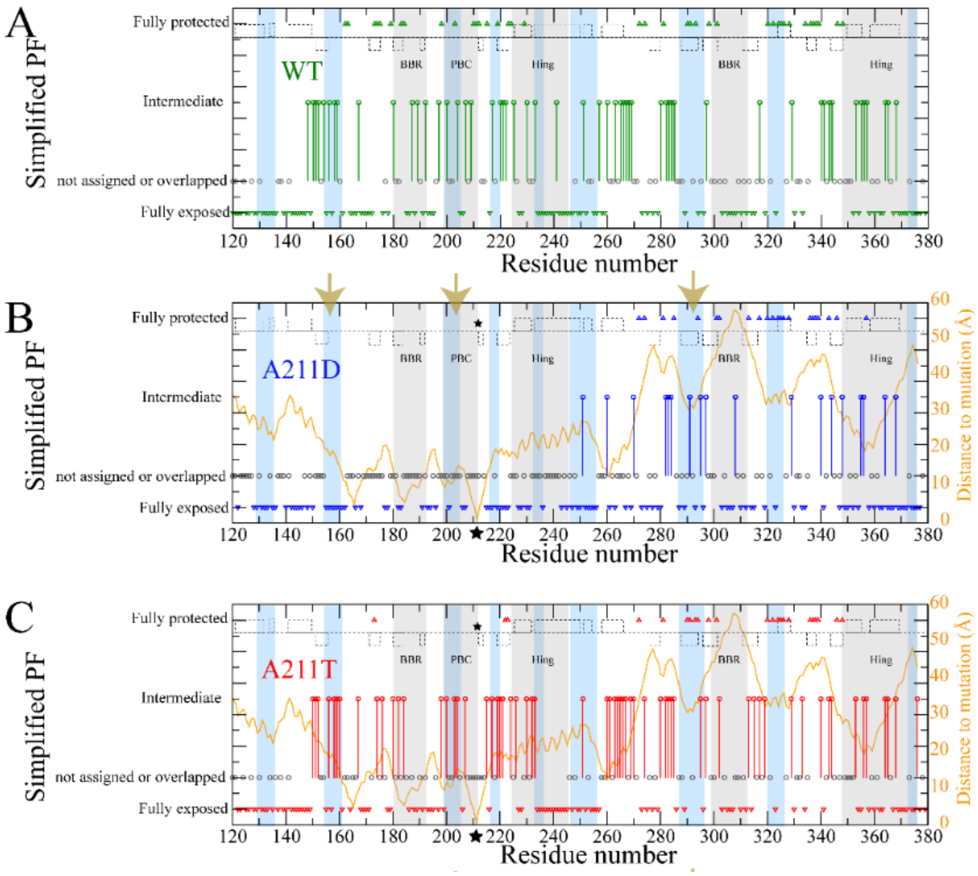

Figure S3.6: *The protection factor category of residues is based on hydrogen-deuterium exchange (HDX) experiments for the wt and the A211 mutants of PKA R1α (119-379) with 0.7 mM excess cAMP.* The black stars are the mutation points, and the orange line is the distance from the mutation point. The gray circles highlighted the residues with no assignment or residues for which peaks overlap with other peaks in the HSQC spectra. The gray area highlighted allosteric hot spots, and the blue area highlighted the aggregation-prone sites detected by AGGRESCAN. The yellow arrows highlight aggregation-prone sites that are more exposed in the CNC mutants than WT.

Figure S 3.7

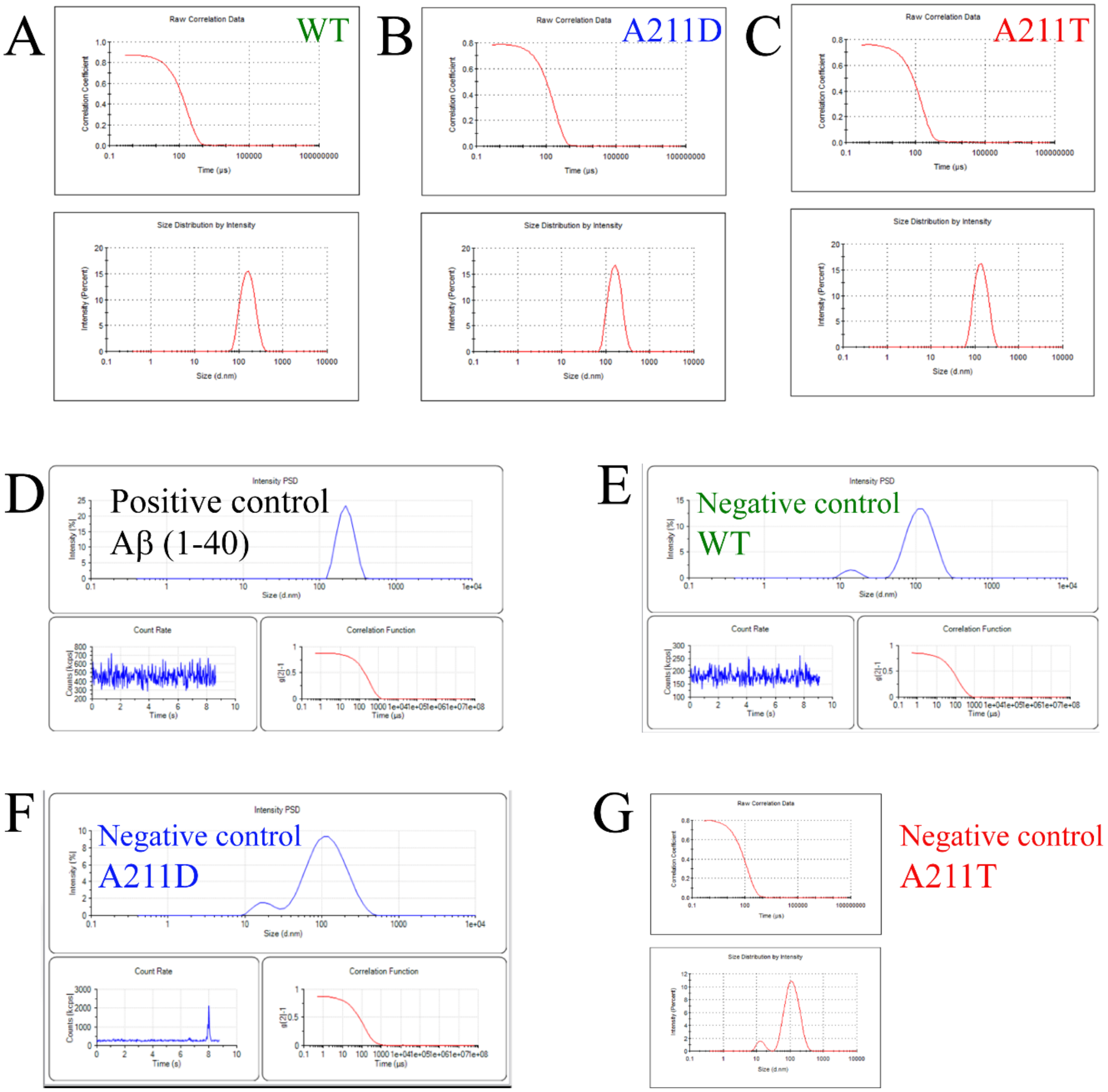

Figure S3.7: *The correlation functions from Dynamic Light Scattering (DLS) data of full-length PKA R1α.* A-C are correlation function data of heat-treated wt, A211D and A211T PKA R1α. D is the correlation function of the positive control which is heat-treated Aβ (1-40). E-G are correlation function data of negative controls which are not heat-treated wt, A211D and A211T PKA R1α. The negative controls were incubated below room temperature.

Chapter 4 Non-Canonical Protein Kinase A Activation by Polymerization of Regulatory Subunits as Revealed by Inherited Carney Complex Mutation G287W

4.1 Author's Preface

The presented work in this chapter along with the previous chapter data is part of an ongoing manuscript. Authors and their affiliation are as follow:

"Naeimeh Jafari[1], Jason Del Rio[2], Madoka Akimoto[1], Jung Ah Byun[3], Stephen Boulton[3], Kody Moleschi[1], Yousif Al Sayyed[1], Pascale Swanson[3], Jinfeng Huang[1], Karla Martinez Pomier[1], Chi Lee, Jian Wu[2], Susan S. Taylor[2,4], Giuseppe Melacini[1,3*]

[1]Department of Chemistry and Chemical Biology, McMaster University, 1280 Main St. W. Hamilton, Canada; [2]Department Pharmacology, University of California San Diego, La Jolla, CA 92093-0653, USA; [3]Department of Biochemistry and Biomedical Sciences, McMaster University, 1280 Main St. W. Hamilton, Canada; [4]Departments of Chemistry and Biochemistry, University of California San Diego, La Jolla, CA 92093-0653, USA"

I acquired most of the experiments of the manuscript and analyzed the data. Jason Del Rio acquired and analyzed the crystal structure of full-length A211D R1α with support from Dr. Jian Wu. Jung Ah Byun acquired one domain urea unfolding data with support from Kody Moleschi. Stephen Boulton, Yousif Al Sayyed, Pascale Swanson, Jinfeng Huang, Karla Martinez Pomier, and Chi Lee helped for plasmid preparation and protein purification and we had useful discussion. I designed the research with Dr. Susan S. Taylor and Dr. Giuseppe Melacini. I co-wrote the manuscript with Dr. Madoka Akimoto, Dr. Susan S. Taylor, and Dr. Giuseppe Melacini.

4.1.1 Acknowledgements

We are grateful to Marcia Reid for assistance with the acquisition of TEM images and, together with Dr. R. Maillard, Dr. G. Veglia, and Dr. Rashik Ahmed for helpful discussions.

4.1.2 Funding

Funding was provided by the Canadian Institutes of Health Research Grant 389522 (to G. M.), the Natural Sciences and Engineering Research Council of Canada Grant RGPIN-2019-05990 (to G. M.) and NIH grant R35-GM130389 (to S.S.T.).

4.1 Abstract

The regulatory subunit of Protein kinase A (PKA) R1α is the site of familial mutations including the Carney complex (CNC), which is linked to spotty skin pigmentation, and a wide range of tumors and myxomas, including cardiac and breast myxomas, pancreatic and liver cancer. CNC mutations are related to PKA over-activation, but the underlying molecular mechanism is not completely understood for all CNC mutations, especially the ones that cause a decrease in cAMP sensitivity such as A211D and G287W. Here, we examine G287W through comparative analyses of unfolding, aggregation, and kinase inhibition of G287W *vs.* wt PKA R1α. Since acrodysostosis type 1 (ACRDYS1) mutations exhibit a decreased PKA activity phenotype contrary to CNC mutations, we also used a cognate ACRDYS1 mutant, G287E, in our comparisons. Through different methods such as intrinsic and extrinsic fluorescence, HDX NMR, SEC, NMR intensity losses, TEM, and kinase assay, we show that the increased PKA C activation is caused by G287W PKA R polymerization similar to A211D located in cyclic nucleotide binding domain (CBD) A. Overall, our data suggest that the G287W mutation not only perturbs the canonical cAMP-dependant activation pathway but also enhances the non-canonical activation pathway, which is based on the loss of PKA R1α inhibitory potency through G287W induced polymerization.

4.2 Introduction

For general introduction to PKA, CNC, and ACRDYS1 we refer to chapter 1 and 3. Here, to investigate if our proposed non-canonical mechanism is specific of A211D or extendable to other CNC mutants, here we study G287W, which is located in CBD-B contrary to the other CNC mutations and also is accompanied by an ACRDYS1 cognate mutant. The frequency of mutations at G287 points to its importance in understanding the PKA system and gives the opportunity of having a disease-related control with opposite phenotype. Since the classical cAMP dependant mechanism of PKA C activation fails to explain the G287W CNC phenotype, we hypothesize that a possible mechanism is the activation of PKA C through losses of G287W PKA R1a due to its self-association, similar to the A211D CNC mutant over-activation mechanism. The reduced cAMP affinity and destabilization of G287W PKA R1α makes the protein more prone to unfold [15] and, consequently, more prone to polymerization [16]. Bioinformatics analyses suggest that PKA R1α exhibits an intrinsic propensity of polymerization, and the inhibitory hot spot of R_2:C_2 complex is not accessible in polymerized PKA R1α [17]. Since the hot spot of holoenzyme complex is not accessible for PKA C after polymerization, the inhibitory potency of the G287W R1α reduces upon its polymerization; thus, polymerized G287W explains the CNC's overactivation. To test this hypothesis, here we present a comparative analysis of G287W and wt PKA R1α's unfolding, polymerization, and inhibition. We also used the cognate ACRDYS1 mutation, G287E, as a mutational control pair for our study.

To investigate the mutant's folding, we used bioinformatics, full-length urea unfolding by intrinsic tryptophan fluorescence, chemical shift analysis, and hydrogen/deuterium exchange (HDX) monitored by NMR at the residue level. For the polymerization section, we compared size-exclusion chromatography (SEC) profiles, binding of extrinsic fluorophores (ThT and ANS), NMR intensity losses, and transmission electron microscopy (TEM). Luminescence-based kinase inhibition assays tested the mutant's compatibility for PKA C binding and regulation. Our results show that the G287W CBDs' unfolding is more pronounced than wt and the cognate ACRDYS1 mutant, so the formation of the cross-β structure increases in this CNC mutant. The polymerized G287W lost its inhibitory function for PKA C. Overall, our data confirm our original A211D-based hypothesis that the non-classical PKA C activation through PKA R polymerization is also applicable to the kinase over-activation of the G287W CNC mutation, suggesting that the proposed non-canonical mechanism of PKA C activation through PKA R polymerization is more general than anticipated uniquely based on the A211D results in the previous chapter.

4.3 Results

The Destabilization Effect of the CNC Mutation G287W on the PKA R1α Fold is Significantly Greater than its Cognate G287E ACRDYS1 Mutant. To evaluate the G287 mutations' impact on the structure of PKA R1α, we first checked the stability ($\Delta\Delta G$) compared to wt through the structure-based Eris software (Table 4.1) [18]. A positive (negative) $\Delta\Delta G$ value reflects the structural destabilization (stabilization) effect of a mutant [18]. As illustrated in Table 1, the calculated $\Delta\Delta G$ values for the G287W mutant in all PKA R1α input constructs are higher than those computed for the G287E mutant. Our Eris input constructs are adapted from the cAMP- or C-binding PKA R1α structures to assess whether this destabilization impact is conformational specific or not (Table 4.1). Our computational data indicate that the CNC G287 mutation leads to a larger folding instability in PKA R1α than the cognate ACRDYS1 G287 mutant irrespective of which initial conformation is chosen. To test our computational data, we used urea unfolding monitored through intrinsic Trp fluorescence of wt, G287W, and G287E PKA R1α [19,20] (Figure 4.2). The urea unfolding of both mutations shows that they unfold at slightly lower urea concentrations than wt. Under our conditions, the C_m of wt PKA R1α is ~6.4 M, while the C_m values of the G287E and G287W mutants slightly decrease to ~6.3 M and ~5.9 M, respectively (Figure 4.2).

The urea unfolding data in Figure 2 shows that G287W is the less stable mutant than G287E, as predicted by the Eris. Since the loss of cAMP binding affinity is more dramatic for the ACRDYS1 mutant than the CNC mutant [9], the CNC destabilization compared to the ACRDYS1 is likely to arise from an intrinsic destabilization of PKA R1α structure. However, since the unfolding data acquired through intrinsic Trp fluorescence could also be affected by the CNC mutation to Trp, we confirmed this CNC destabilization through another method. Therefore, we monitored the effect of the G287 mutations through NMR chemical shifts (Figure 4.3) and hydrogen-deuterium exchange (HDX; Figure 4) of the PKA R1α CBDs structure. NMR not only offers a residue-resolution map of the perturbation induced by the G287 mutations, but it also directly probes both CBDs, something that was entirely impossible using intrinsic fluorescence as the endogenous Trp residues of PKA R1α are primarily located in CBD-A.

The G287 Mutations Mainly Perturb the PKA R1α Ground Folded State Locally Without any Major Changes in the Global Fold. To obtain residue-specific data by NMR, we used the 119-379 construct of PKA R1α, which contains both tandem CBDs. We acquired $^{1}H^{15}N$-HSQC spectra of the wt as well as G287W and G287E PKA R1α (Figure 4.3A,B). The G287W mutation causes significant intensity losses and chemical shift changes compared to wt PKA R1α (Figure 4.3A). The G287E mutation also leads to chemical shift changes relative to wt PKA R1α (Figure 4.3B). The most significant chemical shift changes for both ACRDYS1 and CNC mutations are localized around G287 in CBD-B and part of the CBD-A/B interface (Figure 4.3C,D). However, the overall chemical shifts of the G287 mutants are quite comparable to those of wt (Figure 4.3E,F), indicating that the ground state conformation of the ensemble sampled by both the G287 mutants preserved a global fold similar to wt PKA R1α. This result confirms the Eris computations, which show that both G287 mutations cause minor structural changes in PKA R1α, as calculated through the mutant *vs.* wt RMSD values (Table 4.1). However, based on the urea unfolding data (Figure 4.2) and the Eris stability predictions, we anticipate more accessible unfolded and/or partially unfolded excited states for the G287W compared to wt and G287E. Therefore, we expect to observe more solvent-exposed residues for the G287W mutant relative to wt and G287E mutant. To evaluate this prediction, we assessed the residue-specific solvent exposure of PKA R1α through HDX monitored in real-time by NMR (Figure 4.4).

*Under Native conditions, The Solvent Exposure of Both CBDs Increases for the G287W Mutation Compared to Wt and the G287E Mutation.*We used a semi-quantitative protocol similar to chapter 3 for the measurement of solvent exposure through H/D exchange (examples of exchange categories are presented in Figure S4.1). We mapped the results of our HDX experiments for wt, G287W, and G287E PKA R1α on the PKA R1α CBDs' structure of 1RGS (Figure 4.4). The darker shade of colors represents the fully protected category, and the lighter color shade is for the fully exposed group.

The G287W mutant results in a loss of fully protected and intermediate residues (Figure 4.4A). The drops in full protection and intermediate categories in the G287W are compensated by a higher frequency of residues with full exposure (Figure 4.4A). The loss of fully protected residues and the enhancement of the fully exposed residues indicates that the overall global fold of CBDs is destabilized. For the cognate ACRDYS1 mutant, the G287E, we observed only a slight increase in the occurrence of residues with full protection, with a slight decrease in the occurrence of the fully exposed category (Figure 4.4A). So, the order of the overall solvent exposure appears to be wt ≤ G287E < G287W, which confirms the urea unfolding data and the computations of mutant stability for the G287 mutants (Figure 4.2 and Table 4.1).

Contrary to the chemical shift map, the G287 mutations cause changes in solvent exposure in both domains (Figure 4.4B-D). The fully protected and intermediate residues of G287W decreased, while the fully exposed residues elevated compare to wt (Figure 4.4A). Contrary, G287E shoes a slight increase in the fully protected residues and a slight decrease in fully exposed residues (Figure 4.4A). In both G287 mutations, several residues from both CBDs become more solvent-exposed than wt (Figure 4.4C,D; black arrows). Both mutants also include residues with a gain of protection (Figure 4.4C,D; orange arrows) in both CBDs. These results agree with the Eris predictions and with the notion that the overall solvent exposure in G287W is enhanced compared to both G287E and wt PKA R1α. Notably, only the CNC mutant increases the exposure of the αP helixes in Phosphate Binding Cassette (PBC) of the CBDs, which are aggregation-prone sites (highlighted as surface on structure in Figure 4.4B-D) [21,22]. Therefore, our HDX results indicate that the probability of polymerization is expected to be higher for the G287W mutant relative to wt and G287E PKA R1α. To examine this hypothesis, we investigated self-association and amyloid formation of the G287W PKA R1α through SEC (Figure S4.2A), SEC-MALS

(Figure S4.3), NMR intensity losses (Figure S4.2B), ThT and ANS fluorescence (Figure 4.5), as well as TEM (Figure S4.4).

The G287W Mutant is More Prone to Self-associate than the G287E Mutant and wt PKA R1α. We tested the extent of PKA R1α polymerization through multiple techniques. First, the gel filtration elution of wt and G287W PKA R1α profiles exhibit two peaks at around 44 mL and 68 mL (Figure S4.2A). According to the SEC-MALS data (Figure S4.3), the first peak corresponds to oligomers larger than 100 kDa, while the second peak corresponds to dimeric PKA R1α (Figure S4.2A). Interestingly, the relative oligomer *vs.* dimer intensity increases about twice of wt one in G287W PKA R1α (Figure S4.2A). Therefore, the G287W mutant self-associates more than wt, even below room temperature. To further support these data, we monitored the self-association of PKA R1α through 1D ^{1}H NMR methyl intensity loss [23–26] upon heat treatment (Figure S4.2B). For wt, such losses is ~20 % (Chapter 3), but they increase to ~80 % for G287W, corroborating our hypothesis that the G287W's polymerization propensity is increased compared to wt PKA R1α.

The Cross-β Sheet and Exposed Hydrophobic Sites Content Is Higher in the G287W Oligomers than than G287E and Wt PKA R1α. We examined the nature of the polymerized wt, G287W, and G287E R1α, through binding of polymerized R1α to ThT and ANS extrinsic fluorophores, which report on cross-β sheets [23,27] and hydrophobic exposure [28,29] content, respectively (Figure 4.5A,B). After 14 hours of incubation at 60 ^{o}C, which results in the formation of PKA R1α oligomers for both G287 mutants and wt, ThT fluorescence of PKA R1α was checked (Figure 4.5A). TEM images also confirm PKA R1α's oligomerization after a 14-hour incubation period at 60 ^{o}C (Figure S4.4). The presence of the developed assemblies before the heat treatment, together with our SEC data (Figure S4.2A), indicates that self-association is an intrinsic property of PKA R1α, which heat treatment amplifies (Figure S4.4).

The ThT fluorescence of wt, G287W, and G287E PKA R1α shows that G287W exhibits the highest cross-β assemblies among the three (Figure 4.5A). The ANS fluorescence of wt, G287W, and G287E PKA R1α reveals a significant increase for G287W compare to the wt and G287E, reflecting its most significant growth of hydrophobic exposure upon 14-hour incubation at 60 ^{o}C (Figure 4.5B). Overall, the order of cross-β formation and enhancement of hydrophobic exposure propensity are G287W > G287E > wt (Figure 4.5A,B). These results are in agreement with computational stability, urea unfolding, and HDX of G287 mutations. Since there is some overlap between the aggregation-prone sites in PKA R1α [21,22,30,31] and the critical sites for PKA R:C complex formation, *e.g.* the CBD-A's αP helix, we hypothesize that the polymerized G287W mutant decreases the PKA R1α's inhibitory potency for the PKA C. This hypothesis was tested through the kinase inhibition assay of the CNC mutant (Figure 4.5C).

The polymerization of G287W leads to a loss of PKA C inhibition (Figure 4.5C). The inhibition competency of the G287W PKA R1α for PKA C before heat treatment shows that under our experimental conditions the G287W PKA R1α mutant fully inhibits PKA C similar to wt PKA R1α, which serves as our positive control. However, the G287W

PKA R1α completely lost its inhibitory potency for PKA C after its heat-treated polymerization (Figure 4.5C). The loss of inhibitory function is not due to the precipitation, as UV absorbance at 280 nm demonstrates the presence of the protein in solution even after heat treatment. Therefore, our data validate the hypothesis that the over-activation of PKA C in CNC mutants can be explained through a mechanism of suppressed inhibitory capacity due mutation-induced polymerization of G287W, similar to A211D.

4.4 Discussion

One of the PKA C Activation Mechanisms for the G287W PKA R CNC mutant is through PKA R Polymerization. As the canonical cAMP-dependent allosteric response starts from CBD-B and the affinity for cAMP decreases relative to wt PKA R1α in the CBD-B of G287W [9], explaining the CNC over-activation phenotype for G287W in the context of the canonical \ cAMP dependant pathway is challenging. The non-canonical PKA C activation pathway is confirmed through the comparative analysis of the unfolding, aggregation, and kinase inhibition profiles for wt PKA R1α and the G287 CNC/ACRDYS1 mutants. This new polymerization-induced activation mechanism is schematically shown in chapter three in the blue shaded area. The G287W mutant increases solvent exposure through the reduced binding affinity for cAMP and/or the diminished free energy of unfolding of apo R. The rise of the solvent exposed residues in G287W is in agreement with the increased activation constant [9], computations (Table 4.1), urea unfolding (Figure 4.2), and HDX NMR (Figure 4.4; and Figure S4.1).

The HDX data show that unfolding is not localized to the mutation point and CBD-B, but also observed in the CBD-A. This extensive unfolding of G287W R leads to the exposure of aggregation-prone sites, such as the αP helices in the two PBCs of PKA R1α, to the solvent. The accessible aggregation-prone motives increase the probability to form cross-β sheet-rich oligomers of PKA R1α, as supported by ThT fluorescence, NMR intensity losses, and TEM (Figure 4.5A,B and Figure S4.2- S4.4). Consequently, the polymerized PKA R1α shields critical sites needed for a stable R:C complex, which in turn leads to a loss in the inhibitory potency of the polymerized PKA R1α for PKA C under our experimental conditions, as confirmed by kinase assays (Figure 4.5C).

The G287W-induced unfolding is not as destabilizing as the CBD-A mutation (*i.e.* A211D), as expected because CBD-B is not as efficient in unfolding CBD-A, as CBD-A is in unfolding CBD-B [33]. These CBD-B *vs.* CBD-A differences in destabilization and the proposed polymerization-induced activation model offer a viable explanation for why most of the CNC mutations are found in CBD-A [12]. It is also notable that the G287W mutations appears to be more efficient than its cognate ACRDYS1 counterpart (*i.e.* G287E) in destabilizing PKA R1α and inducing the formation of PKA inhibition incompetent polymers. These unfolding/aggregation difference may explain the CNC *vs.* ACRDYS1 differential between the two G287 mutants and further illustrate the specific link between CNC and the non-canonical PKA activation by R1α polymerization.

In conclusion, the inconsistency between the CNC over-activation phenotype with the decreased cAMP affinity of the G287W mutant is explained here through the non-classical activation mechanism of PKA C by PKA R polymerization. So, the polymerization-based model is not only explaining the CNC mutation A211D, but also the CNC mutation G287W, which is located in CBD-B. While the non-classical model is not the only explanation for these CNC mutants, it may play a role in the other CNC mutations. This model could be useful also for other disease-related mutations in other kinase systems as well.

4.5 Materials and Methods

The methods utilized to characterize the G287 PKA R1α mutants in this chapter are similar to those used for the A211 mutants in Chapter 3. In addition, for the G287W mutant it was possible to acquire Size Exclusion Chromatography with Multi Angle Light Scattering (SEC-MALS) data. For this purpose, purified G287W (1-379) through HiLoad 16/600 Superdex 200 pg was concentrated to 50 μM through Amicon ultrafiltration and stored in the fridge for two months. After 10 minutes centrifugation at at 12,000 rpm, the G287W PKA R1α (1-379) mutant was loaded on a Superdex 200 increase analytical SEC column, preequilibrated with 50 mM MOPS buffer pH 7.0, 100 mM NaCl, and 5 mM DTT in an AKTA (pure) chromatography system coupled with MALS detectors (Wyatt, Inc.).

4.6 References

1 S. S. Taylor, R. Ilouz, P. Zhang, A. P. Kornev Assembly of allosteric macromolecular switches: lessons from PKA. (2012) *Nat. Rev. Mol. Cell Biol.* **13**, 646–658.

2 Y. S. Cho-Chung, S. Pepe, T. Clair, A. O. Budillon, M. Nesterova cAMP-dependent protein kinase: role in normal and malignant growth. (1995) *Crit. Rev. Oncol. Hematol.* **21**, 33–61.

3 G. Mantovani, F. M. Elli Multiple hormone resistance and alterations of G-protein-coupled receptors signaling. (2018) *Best Pract. Res. Clin. Endocrinol. Metab.* **32**, 141–154.

4 A. Linglart, C. Menguy, A. Couvineau, C. Auzan, Y. Gunes, M. Cancel, et al. Recurrent PRKAR1A mutation in acrodysostosis with hormone resistance. (2011) *N. Engl. J. Med.* **364**, 2218–2226.

5 D. N. Carney, A. F. Gazdar, G. Bepler, J. G. Guccion, P. J. Marangos, T. W. Moody, et al. Establishment and identification of small cell lung cancer cell lines having classic and variant features. (1985) *Cancer Res.* **45**, 2913–2923.

6 L. S. Kirschner, J. A. Carney, S. D. Pack, S. E. Taymans, C. Giatzakis, Y. S. Cho, et al. Mutations of the gene encoding the protein kinase A type I-α regulatory subunit in patients with the Carney complex. (2000) *Nat. Genet.* **26**, 89–92.

7 P. Salpea, C. A. Stratakis Carney complex and McCune Albright syndrome: an overview of clinical manifestations and human molecular genetics. (2014) *Mol. Cell. Endocrinol.* **386**, 85–91.

8 C. Kamilaris, F. Faucz, A. Voutetakis, C. Stratakis Carney Complex. (2019) *Exp. Clin. Endocrinol. Diabetes*. **127**, 156–164.

9 Y. Rhayem, C. Le Stunff, W. A. Khalek, C. Auzan, J. Bertherat, A. Linglart, et al. Functional characterization of PRKAR1A mutations reveals a unique molecular mechanism causing acrodysostosis but multiple mechanisms causing Carney complex. (2015) *J. Biol. Chem.* **290**, 27816–27828.

10 J. G. H. Bruystens, J. Wu, A. Fortezzo, J. Del Rio, C. Nielsen, D. K. Blumenthal, et al. Structure of a PKA RIα recurrent acrodysostosis mutant explains defective cAMP-dependent activation. (2016) *J. Mol. Biol.* **428**, 4890–4904.

11 A. Horvath, J. Bertherat, L. Groussin, M. Guillaud-Bataille, K. Tsang, L. Cazabat, et al. Mutations and polymorphisms in the gene encoding regulatory subunit type 1-alpha of protein kinase A (PRKAR1A): an update. (2010) *Hum. Mutat.* **31**, 369–379.

12 A. Rothenbuhler, C. A. Stratakis Clinical and molecular genetics of Carney complex. (2010) *Best Pract. Res. Clin. Endocrinol. Metab.* **24**, 389–399.

13 E. L. Greene, A. D. Horvath, M. Nesterova, C. Giatzakis, I. Bossis, C. A. Stratakis In vitro

functional studies of naturally occurring pathogenic PRKAR1A mutations that are not subject to nonsense mRNA decay. (2008) *Hum. Mutat.* **29**, 633–639.

14 J. G. H. Bruystens, J. Wu, A. Fortezzo, A. P. Kornev, D. K. Blumenthal, S. S. Taylor PKA RIα homodimer structure reveals an intermolecular interface with implications for cooperative cAMP binding and Carney complex disease. (2014) *Structure*. **22**, 59–69.

15 R. Das, M. Abu-Abed, G. Melacini Mapping allostery through equilibrium perturbation NMR spectroscopy. (2006) *J. Am. Chem. Soc.* **128**, 8406–8407.

16 K. W. Tipping, P. van Oosten-Hawle, E. W. Hewitt, S. E. Radford Amyloid fibres: inert end-stage aggregates or key players in disease? (2015) *Trends Biochem. Sci.* **40**, 719–727.

17 K. K. Dao, A. L. Pey, A. U. Gjerde, K. Teigen, I.-J. L. Byeon, S. O. Døskeland, et al. The regulatory subunit of PKA-I remains partially structured and undergoes β-aggregation upon thermal denaturation. (2011) *PLoS One*. **6**, e17602.

18 S. Yin, F. Ding, N. V Dokholyan Eris: an automated estimator of protein stability. (2007) *Nat. Methods*. **4**, 466–467.

19 J. M. Cànaves, D. A. Leon, S. S. Taylor Consequences of cAMP-binding site mutations on the structural stability of the type I regulatory subunit of cAMP-dependent protein kinase. (2000) *Biochemistry*. **39**, 15022–15031.

20 D. A. Leon, J. M. Canaves, S. S. Taylor Probing the multidomain structure of the type I regulatory subunit of cAMP-dependent protein kinase using mutational analysis: role and environment of endogenous tryptophans. (2000) *Biochemistry*. **39**, 5662–5671.

21 R. Linding, J. Schymkowitz, F. Rousseau, F. Diella, L. Serrano A comparative study of the relationship between protein structure and β-aggregation in globular and intrinsically disordered proteins. (2004) *J. Mol. Biol.* **342**, 345–353.

22 A.-M. Fernandez-Escamilla, F. Rousseau, J. Schymkowitz, L. Serrano Prediction of sequence-dependent and mutational effects on the aggregation of peptides and proteins. (2004) *Nat. Biotechnol.* **22**, 1302–1306.

23 J. Milojevic, A. Raditsis, G. Melacini Human serum albumin inhibits Aβ fibrillization through a “monomer-competitor” mechanism. (2009) *Biophys. J.* **97**, 2585–2594.

24 J. Milojevic, V. Esposito, R. Das, G. Melacini Understanding the molecular basis for the inhibition of the Alzheimer’s Aβ-peptide oligomerization by human serum albumin using saturation transfer difference and off-resonance relaxation NMR spectroscopy. (2007) *J. Am. Chem. Soc.* **129**, 4282–4290.

25 M. Algamal, J. Milojevic, N. Jafari, W. Zhang, G. Melacini Mapping the Interactions between the Alzheimer’s Aβ-peptide and human serum albumin beyond domain resolution. (2013) *Biophys. J.* **105**, 1700–1709.

26 M. Algamal, R. Ahmed, N. Jafari, B. Ahsan, J. Ortega, G. Melacini Atomic-resolution map

of the interactions between an amyloid inhibitor protein and amyloid β (Aβ) peptides in the monomer and protofibril states. (2017) *J. Biol. Chem.* **292**, 17158–17168.

27 M. Biancalana, S. Koide Molecular mechanism of Thioflavin-T binding to amyloid fibrils. (2010) *Biochim. Biophys. Acta (BBA)-Proteins Proteomics*. **1804**, 1405–1412.

28 O. K. Gasymov, B. J. Glasgow ANS fluorescence: potential to augment the identification of the external binding sites of proteins. (2007) *Biochim. Biophys. Acta (BBA)-Proteins Proteomics*. **1774**, 403–411.

29 A. J. Weids, S. Ibstedt, M. J. Tamás, C. M. Grant Distinct stress conditions result in aggregation of proteins with similar properties. (2016) *Sci. Rep.* **6**, 24554.

30 F. Rousseau, J. Schymkowitz, L. Serrano Protein aggregation and amyloidosis: confusion of the kinds? (2006) *Curr. Opin. Struct. Biol.* **16**, 118–126.

31 O. Conchillo-Solé, N. S. de Groot, F. X. Avilés, J. Vendrell, X. Daura, S. Ventura AGGRESCAN: a server for the prediction and evaluation of" hot spots" of aggregation in polypeptides. (2007) *BMC Bioinformatics*. **8**, 65.

32 R. Walker-Gray, F. Stengel, M. G. Gold Mechanisms for restraining cAMP-dependent protein kinase revealed by subunit quantitation and cross-linking approaches. (2017) *Proc. Natl. Acad. Sci.* **114**, 10414–10419.

33 E. T. McNicholl, R. Das, S. SilDas, S. S. Taylor, G. Melacini Communication between tandem cAMP binding domains in the regulatory subunit of protein kinase A-Iα as revealed by domain-silencing mutations. (2010) *J. Biol. Chem.* **285**, 15523–15537.

34 Y. Su, W. R. Dostmann, F. W. Herberg, K. Durick, N. H. Xuong, L. Ten Eyck, et al. Regulatory subunit of protein kinase A: structure of deletion mutant with cAMP binding domains. (1995) *Science (80-.).* **269**, 807–813.

35 J. Wu, S. Brown, N.-H. Xuong, S. S. Taylor RIα subunit of PKA: a cAMP-free structure reveals a hydrophobic capping mechanism for docking cAMP into site B. (2004) *Structure*. **12**, 1057–1065.

36 T.-W. Lu, J. Wu, P. C. Aoto, J.-H. Weng, L. G. Ahuja, N. Sun, et al. Two PKA RIα holoenzyme states define ATP as an isoform-specific orthosteric inhibitor that competes with the allosteric activator, cAMP. (2019) *Proc. Natl. Acad. Sci.* **116**, 16347–16356.

37 C. Kim, C. Y. Cheng, S. A. Saldanha, S. S. Taylor PKA-I holoenzyme structure reveals a mechanism for cAMP-dependent activation. (2007) *Cell*. **130**, 1032–1043.

4.7 Figure and Tables

Table 4.1

Table 4.1. *Estimation of G287 Mutants vs. WT PKA R1α Stability (ΔΔG)* [a]

State	**PDB and construct**	**Disease**	**Mutant**	**ΔΔG (kcal/mol)** [b]	**RMSD (Å)** [c]
cAMP bound	4MX3 [d] 1-379 (15)	CNC	G287W	> 10	0.945
		ACRDYS1	G287E	6.98	1.114
	1RGS [d] 91-379 (46)	CNC	G287W	> 10	0.528
		ACRDYS1	G287E	0.81	0.535
C-sub bound	6NO7 [e, f] 1-379 (38)	CNC	G287W	> 10	1.299
		ACRDYS1	G287E	-3.47	1.230
	2QCS [f] 91-379 (5)	CNC	G287W	> 10	0.589
		ACRDYS1	G287E	-3.30	0.725

[a] Based on the ERIS software implemented with flexible backbone and pre-relaxation.(19) [b] Positive (negative) ΔΔG (kcal/ mol) values indicate that the mutant destabilizes (stabilizes) the structure. [c] The RMSD of the predicted structure compared to the initial WT structure. [d] The cAMP ligands were removed from the PDB file before submission to ERIS. [e] One R1α protomer was removed from the PDB file utilized as ERIS input. [f] The C-subunit was removed from the PDB file for ERIS input.

Figure 4.1

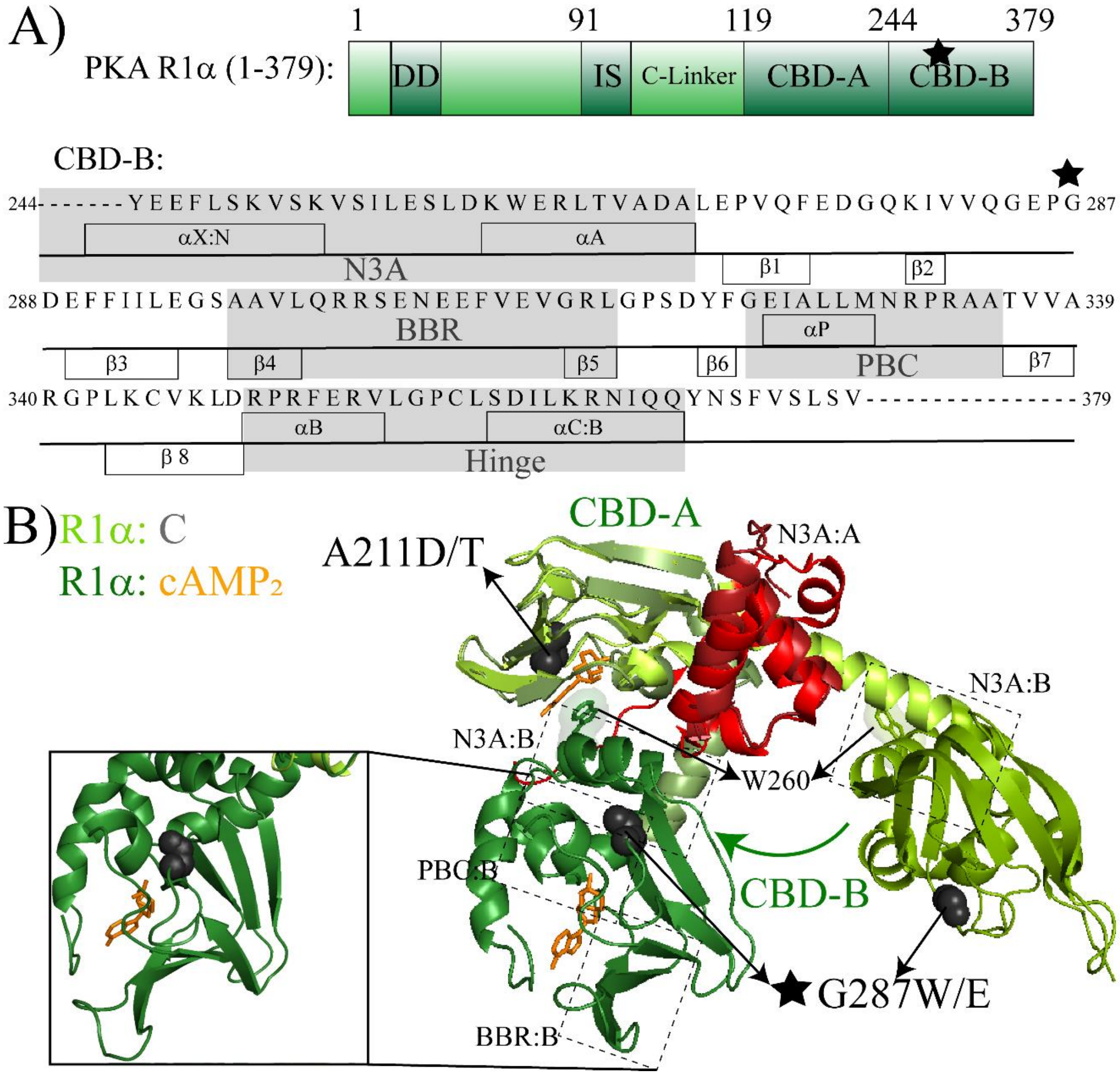

Figure 4.1: *The PKA R1α G287 Mutations.* (A) Domain organization of PKA R1α and CBD-B secondary structure shown along its sequence. Gray areas are allosteric hot spots. The black star is Gly 287, which is mutated to Trp in CNC and to Glu in ACRO. (B) Structure of PKA R1α cAMP-binding domains in the cAMP-bound state (dark green; PDB: 1RGS [34]) and C-subunit-bound state (lime; PDB:2QCS [37]). Mutation sites, Gly287 and Ala211 are highlighted in black spheres and cAMP is presented with orange sticks.

Figure 4.2

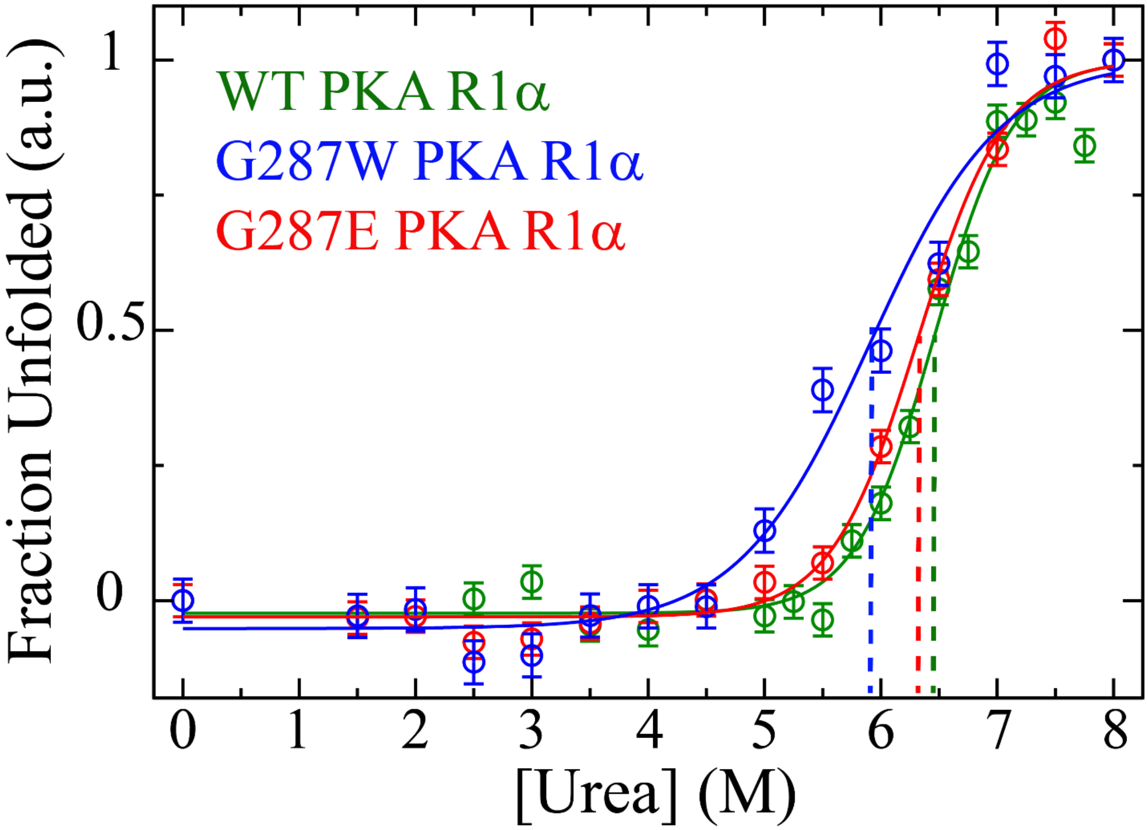

Figure 4.2: *Urea Unfolding Profiles of Full Length wt, G287W and G287E PKA RIα.* Urea unfolding profiles monitored through intrinsic fluorescence for 5 μM of full-length PKA R1α (1-379) in the presence of 100-fold excess cAMP. The color code is shown in the figure. Both mutants decrease the stability, but the effect of the CNC mutations is more pronounced than that of the ACRO mutation.

Figure 4.3

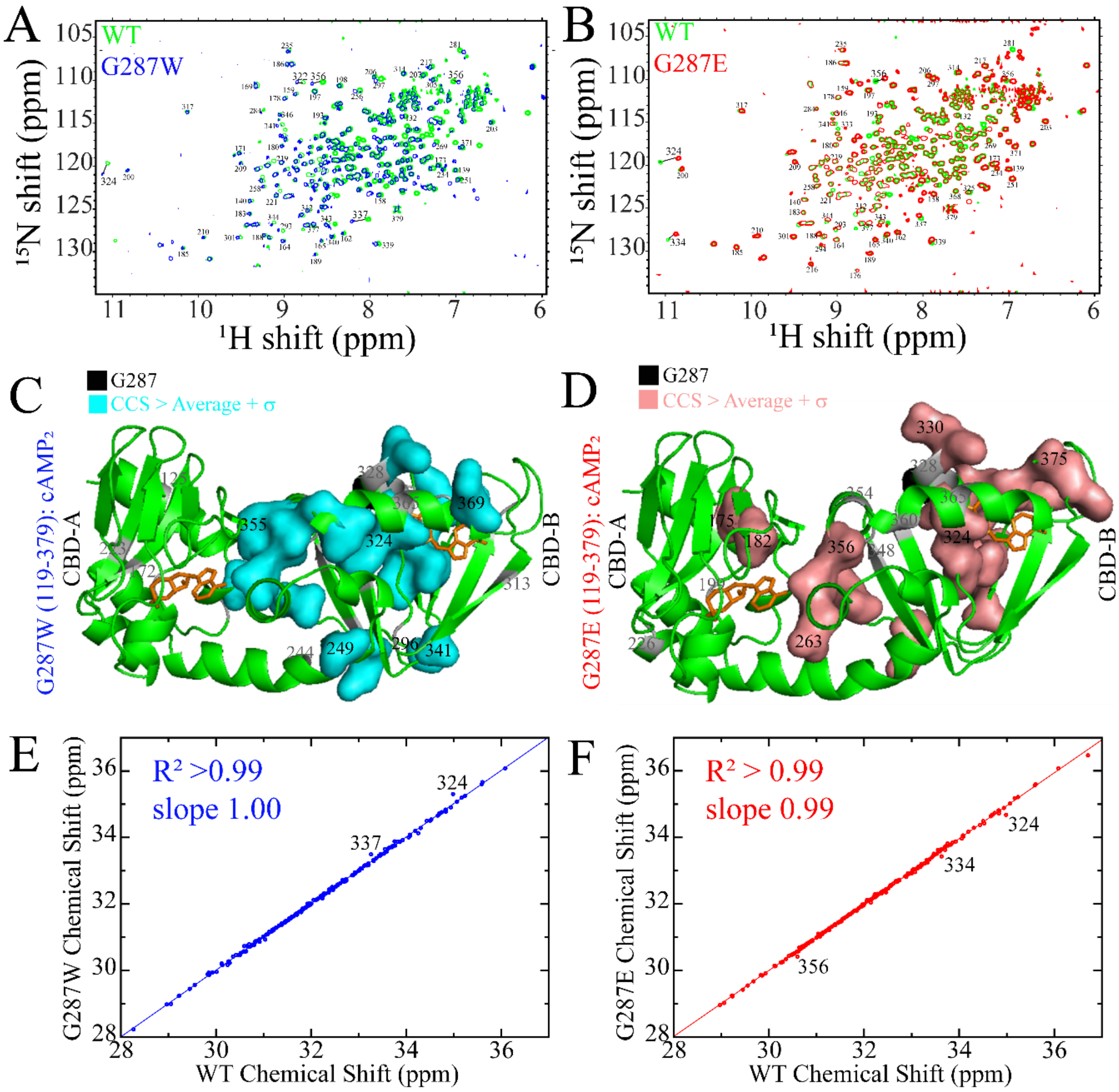

Figure 4.3: *Chemical Shift Map of the Perturbations Caused by CNC and ACRO G287 Mutations on PKA R1α Tandem CBDs.* (A) Overlay of HSQCs spectra of G287W (blue) and wt PKA R1α (119-379) (green) in the presence of 1.2 mM cAMP. Selected residue numbers are shown in black. (B) As A, but for the G287E mutation. (C) Map of the residues with the largest G287W-induced CCS changes on the structure of the tandem PKA R1α CBDs bound to cAMP (PDB code: 1RGS [34]). Unassigned or broadened beyond detection residues are highlighted with a gray ribbon. (D) As C, but for the G287E mutation. (E) Correlation between the compounded chemical shifts (CCS) of G287W and wt PKA R1α (119-379) from the spectra in (A). (F) As E, but for the G287E mutation.

Figure 4.4

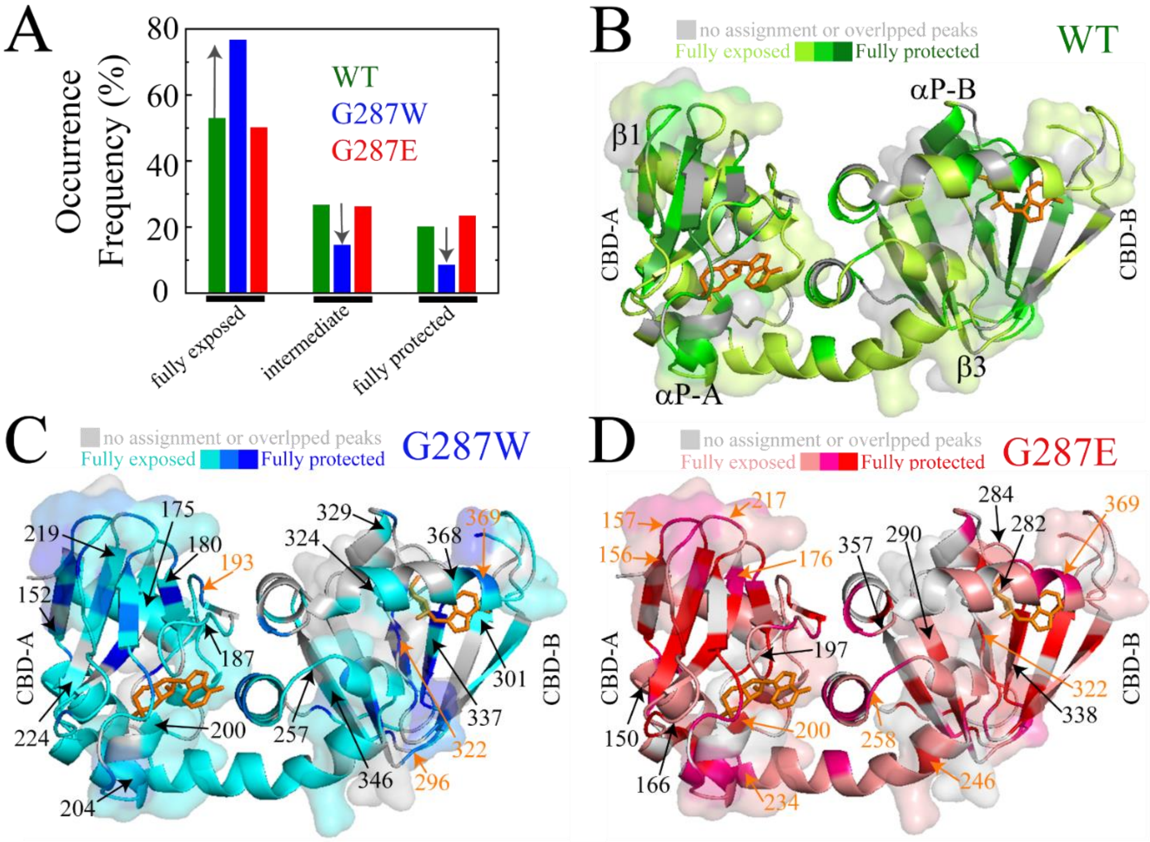

Figure 4.4: *HDX Map of the Perturbations Caused by CNC and ACRDYS1 G287 Mutations on the PKA R1α Tandem CBDs.* Residue-specific solvent exposure as gauged based on H/D exchange monitored by HSQC spectra for the PKA R1α (119-379) construct in the presence of 0.7 mM excess cAMP. Residues are categorized in three groups (Figure S1), as in Chapter 3: fully exposed, intermediate, and fully protected. The cAMP-bound structure (PDB code: 1RGS (46)) is used for all HDX maps. Color codes are shown in the figure. (A) Frequency of occurrence for each exchange class based on the assigned residues. Vertical arrows show the G287W *vs.* wt frequency changes. (B) wt, as in Chapter 3, included here as well for the convenience of comparison. (C) G287W mutant. (D) G287E mutant. Black and orange arrows have the same meaning as in Chapter 3. Surfaces in B-D highlight AmylPred consensus aggregation prone regions.

Figure 4.5

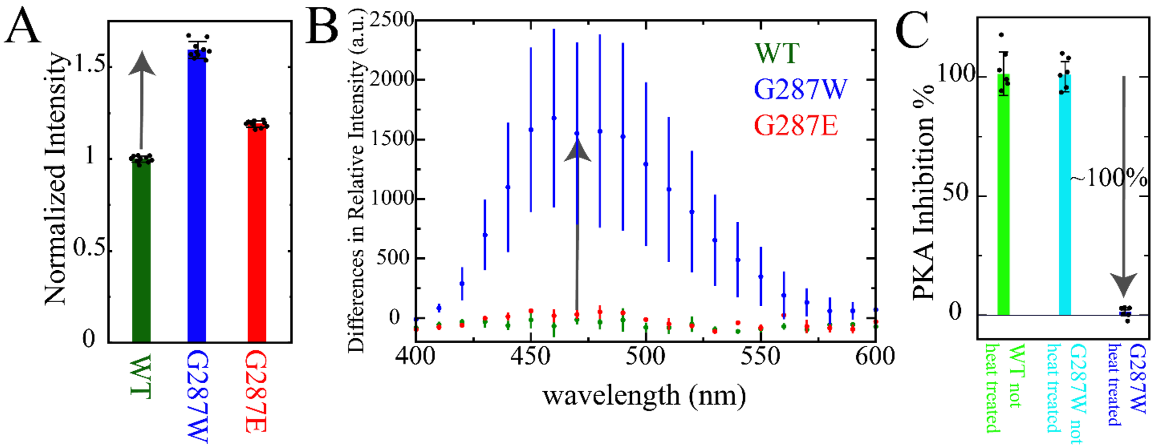

Figure 4.5: *PKA C Activation by PKA G287W R1α Aggregation.* (A) Normalized ThT fluorescence of 8 µM wt, G287W and G287E PKA R1α measured in the presence of 143 µM cAMP after 16 hours of incubation at 60 °C. (B) Heat treatment induced ANS fluorescence intensity difference. (C) Maximum kinase inhibition by G287W PKA R1α before (cyan) and after (blue) heat treatment (60 °C for 90 minutes) at 1 µM G287W PKA R1α, prior to dilution for the kinase assay. The UV absorbance at 280 nm indicates that protein is still present in solution even after heat treatment, hence the loss of PKA inhibition occurring upon heat treatment is not simply the result of precipitation. The wt PKA R1α inhibitory potency (green) is included as a positive control.

4.8 Supplementary Figures

Figure S 4.1

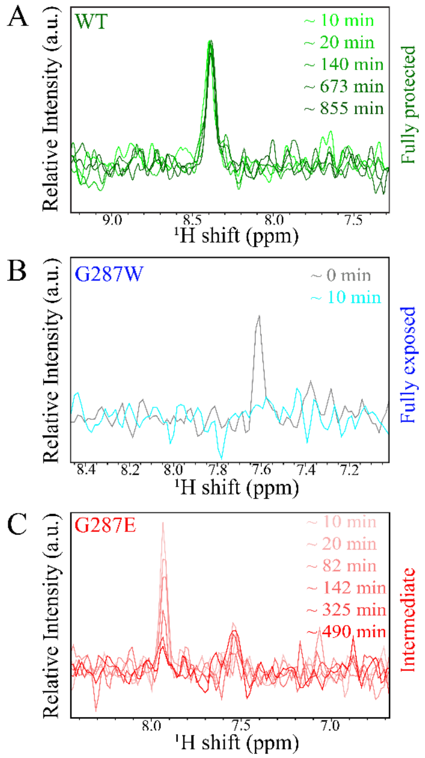

Figure S4.1: 1D cross-sections from peaks in HSQC spectra acquired during the hydrogen-deuterium exchange (HDX) experiments for the wt and G287 mutants of PKA R1α (119-379). The panels illustrate representative cases of residues that are fully protected (A), fully exposed (B) or subject to intermediate exchange (C). Fully exposed residues are defined as those for which H/D exchange is complete within the second HSQC acquisition after the dead time of the experiment. Fully protected residues are defined as those do not appreciably exchange during the course of the H/D experiments (up to 16 hours). Intermediate exchange applies to the residues falling between the fully exposed and fully protected cases. For G287W (B), the first 1D cross-section (gray) is from the control HSQC acquired using the H_2O buffer. In the other panels, lighter shades correspond to 1D cross-section from HSQC spectra recorded at earlier times, while darker shades represent later time points. Residue F198 offers an example of a fully protected residue in wt (A), G314 is a fully exposed residue in G287W (B), and A158 is a residue of G287E exhibiting intermediate exchange (C). Panel A is as in Figure S3A of Chapter 3, but it is reproduced here for the convenience of comparison with the other two panels.

Figure S 4.2

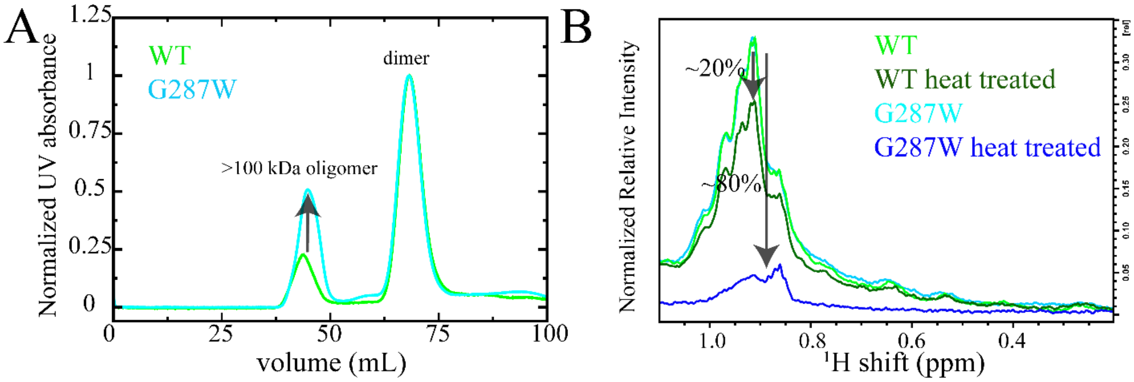

Figure S4.2: *Effect of CNC and ACRO G287 Mutations on PKA R1α Self-Association and Aggregation.* (A) SEC profiles of full length wt, and G287W PKA R1α in the absence of excess cAMP. The intensity of the dimer peak is normalized to one. Hence, the relative intensity of the >100 kDa oligomer peak reflects the extent of oligomerization of the PKA R1α dimer. The wt traces is as in Chapter 3, but it is shown here as well for the convenience of the comparison. (B) Aggregation probed through 1D ^{1}H NMR methyl intensity losses upon mild heat treatment (90 minutes incubation at 60 °C) of 8 μM PKA R1α in the presence of ten-fold excess cAMP. The methyl peak intensity of wt prior to heat treatment is normalized to the methyl intensity of G287W prior to heat treatment. The same normalization scaling constant is applied to the intensity of the heat-treated sample as well. Heat treatment leads to a ~80 % intensity loss for G287W, but only ~20% for wt.

Figure S 4.3

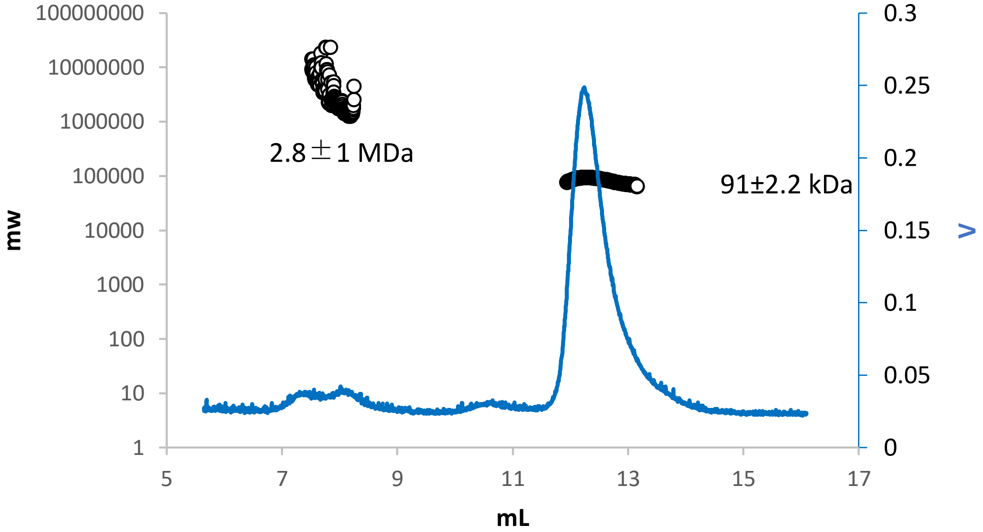

Figure S4.3: *SEC-MALS of G287W PKA RIα full length*. G287W was separated and analyzed using a Superdex 200 increase analytical SEC column and subsequently with MALS. The chromatograms display the light scattering voltage at 90° angle (blue) together with the molar mass of each peak calculated by MALS (circles).

Figure S 4.4

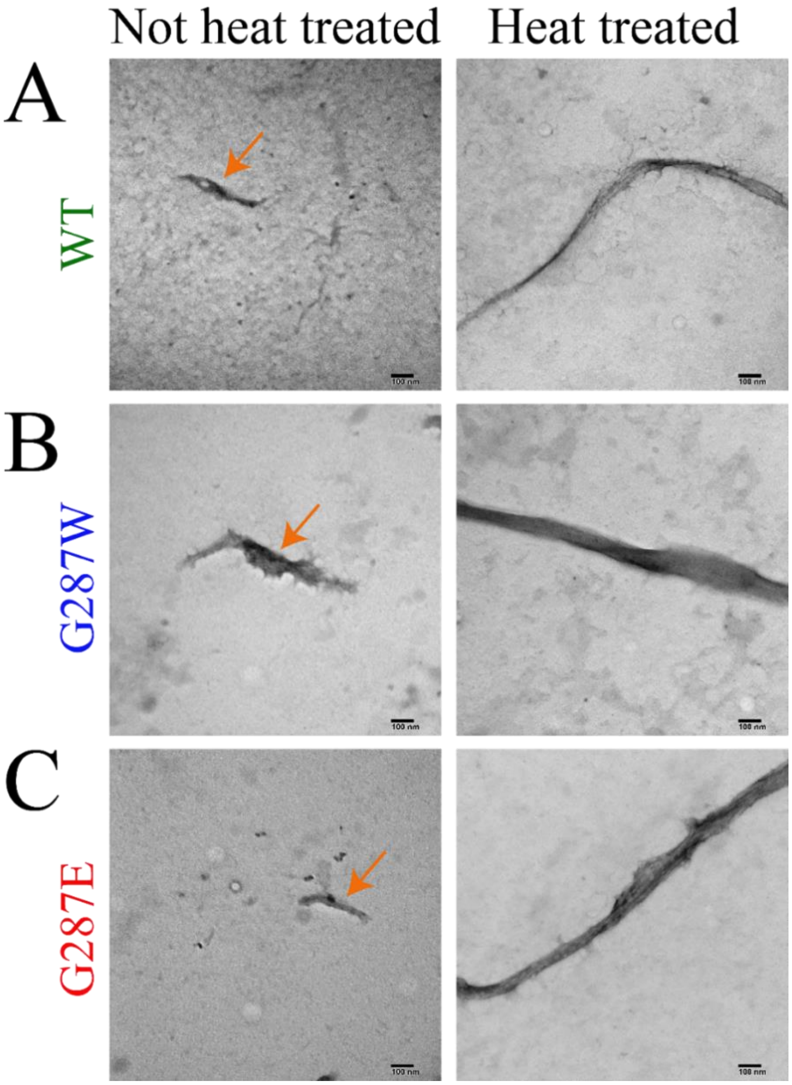

Figure S4.4: *Morphology of wt, G287W and G287E PKA R1α Assemblies Before and After Heat Treatment.* TEM images of PKA R1α in the presence of ten-fold excess cAMP before and after heat treatment (60 °C for 16 hours). Horizontal 100 nm bars are indicated in each panel. PKA R1α oligomers with sizes of the order of 100 nm are already present prior to heat treatment (orange arrows), indicating that the heat treatment accelerates oligomerization processes intrinsic to PKA R1α. These observations apply to wt PKA R1α as well as the two G287 mutants. The wt PKA R1α sample used here is different from that in Chapter 3, showing that aggregate formation is indeed quite reproducible.

4.9 Appendix

Figure S 4.5

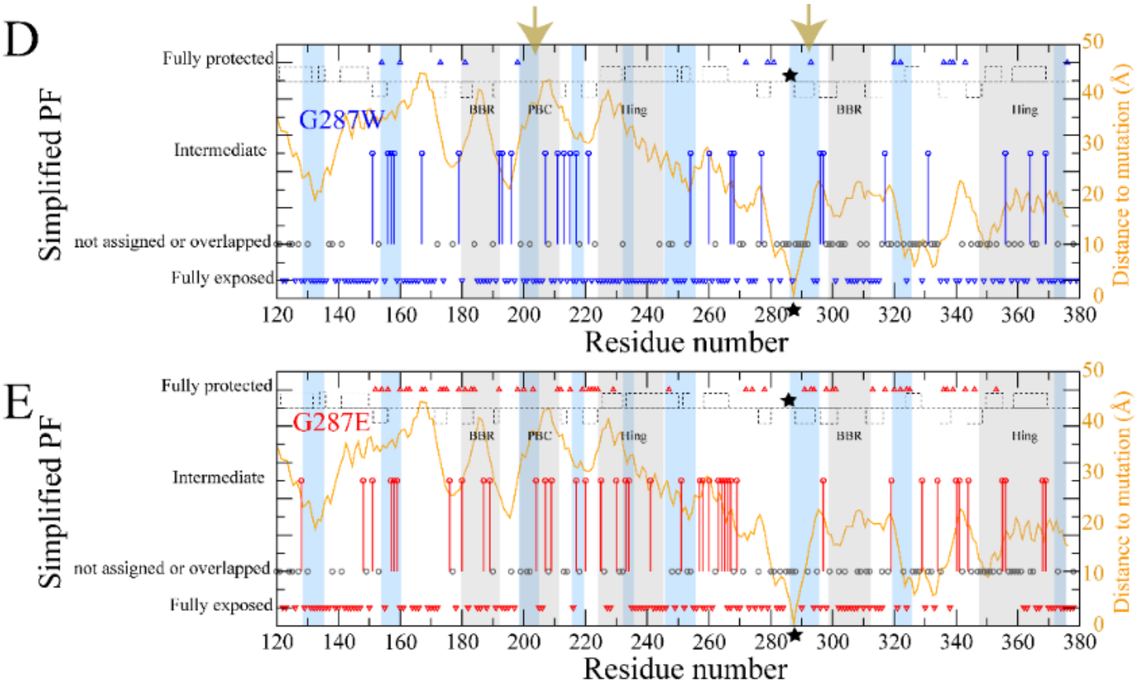

Figure S4.5: *The protection factor category of residues is based on hydrogen-deuterium exchange (HDX) experiments for the wt and the G287 mutants of PKA R1α (119-379) with 0.7 mM excess cAMP*. The black stars are the mutation points, and the orange line is the distance from the mutation point. The gray circles highlighted the residues with no assignment or residues for which peaks overlap with other peaks in the HSQC spectra. The gray area highlighted allosteric hot spots, and the blue area highlighted the aggregation-prone sites detected by AGGRESCAN. The yellow arrows highlight aggregation-prone sites that are more exposed in the CNC mutants than WT.

Chapter 5 Future Directions

In this thesis, we focused on the interdisciplinary research areas at the intersection of the signaling and amyloid fields. In Chapter 2, we present a method we developed for quantifying the amount of long-chain fatty acids bound to human serum albumin (HSA) by considering the allosteric effect of fatty acid (FA) binding, which is a concept imported primarily from signaling. In chapters 3 and 4, we identified a new activation mechanism for protein kinase A (PKA), which is amplified by at least two Carney complex (CNC) disease mutations, A211D and G287W. This non-canonical activation mechanism is through polymerization of the regulatory subunit 1α (R1α) into assemblies that incompetent to inhibit the kinase function of the C-subunit of PKA. Aggregation and self-association are concepts originally central to the amyloid field, but here we show their relevance for signaling as well. These examples are just two starting points to illustrate the fruitful synergies between signaling and amyloids. Here, we discuss possible avenues for future developments of such synergies.

5.1- Future Developments for the CONFA Method

The significance of the CONFA method proposed in Chapter 2 can be appreciated by considering the multiple functions of Human Serum Albumin (HSA). HSA plays different physiological roles, including metal ion chelation, fatty acid (FA) and growth factors carrier, pharmacokinetics modulation (1). HSA also has bacteriostatic effects, promotes proliferation, activates neutrophils, scavenges free radicals, acts as a buffer, and supports tissue remodeling (1). Since HSA serves many other roles beyond the circulation of fatty acids, CONFA is not just a method to determine the amount of long-chain fatty acid bound to HSA, but it can also be used as a tool to map HSA's interactions with other proteins or ligands. In other words, it may apply to many other HSA interaction systems such as metal ions, drugs, and other proteins or peptides. It can also be served as a model to other albumin systems, or it can be used to map HSA's allosteric effects (2). Here, we illustrate some examples of CONFA applications beyond its original FA-binding quantification purpose.

5.1.1- Applications of CONFA in Drug Research

The specific interactions of HSA with drugs can be investigated through the ^{13}C-OA CONFA assay. HSA is the main plasma protein that carries drugs and includes two main drug binding pockets, known as Sudlow sites 1 and 2. These two sites overlap with oleic acid (OA) binding sites, so the competitive binding of drug and OA can be used as a tool to probe the interaction of drugs and HSA. For instance, polymyxin is an antibiotic lipopeptide used to treat gram-negative bacteria (3). Investigation on the pharmacological and pharmacokinetic profile of this group of antibiotics with HSA as a carrier drug is critical (3). This interaction could be examined quantitatively and qualitatively to ensure the drug's effectiveness and possible side effect through the ^{13}C-OA CONFA assay. The drug affinity could be measured through titration of the drug into the HSA pre-saturated by ^{13}C-OA. Also, the allosteric impact of drug binding could be sensed by ^{13}C-OA fingerprint spectra.

Non-specific binding of drugs could also be probed by the CONFA ^{13}C-OA assay. Organic drugs often exhibit limited solubility in aqueous media and they are prone to aggregation. Aggregated drugs often interact non-specifically with enzymes and cause unfolding and false positive results in inhibition assays (4). Albumins are typically used to decrease non-specific interactions. Reportedly, HSA prevents these non-specific interactions by inhibiting drug self-association (4). The interaction between HSA and aggregating drugs can be investigated through competition with ^{13}C-OA, and the CONFA protocol, as drug binding can lead to changes in the peak intensity of HC-HSQC spectra (4). One example of this application pertains to HSA inhibiting self-association of the EPAC-selective inhibitor 09 (ESI-09). The HSA's affinity for ESI-09 was measured based on the ^{13}C-OA assay, which is related to CONFA (4).

Last but not least, the interaction of drug carriers with HSA can also be examined by CONFA and related ^{13}C-OA assays. Drug carriers such as poly(ethylene glycol) nanoparticles interact with plasma proteins (5). The biological and biomedical application of nanoparticles depends on the protein corona, a protein coating layer around the nanoparticle, and affects nanoparticle distribution and toxicity (6). Therefore, investigating the interaction of nanoparticle and HSA is critical in biomedical and biotechnological applications. The ^{13}C-OA CONFA assay is a useful tool that reports if nanoparticle binding leads to an allosteric conformational change. It can also report on the binding kinetics and the effect of binding on fatty acid and other drugs binding. For instance, the biological impact of Nano-Diamonds (NDs), a drug carrier nontoxic only in the presence of serum albumin, is critical for exploiting its biomedical applications (7). The ^{13}C-OA method can be used to investigate the interaction of NDs and HSA and also the effect of other ligands such as metal ions and FAs on the HSA:ND interaction. Compared to standard low-resolution methods, the ^{13}C-OA CONFA assay provides details on all the OA binding pockets, which are distributed through the three HSA domains.

5.1.2- Applications of CONFA to Enhance the Therapeutic Use of HSA

HSA serves multiple therapeutic functions. For example, HSA binds to the Aβ peptide and inhibits Aβ self-association into toxic Aβ oligomers linked to Alzheimer's disease (8–15). Fatty acids compete with Aβ in binding to HSA (9, 10), so the ^{13}C-OA assay could give some insight on HSA:Aβ interaction. Similarly, HSA inhibits the oligomerization of α-synuclein, linked to Parkinson's disease, through binding with sub-μM affinity to αS oligomers, remodeling αS oligomers to less toxic intermediates, and preventing the interaction between membrane and the N-terminal and central regions of αS (16). The HSA binding pockets for αS were probed through ^{13}C-OA assays and competitive binding with ANS and Dan F, showing that they are different from the drug-binding Sudlow sites 1 and 2 (16). Also, binding of αS monomers imposes conformational changes on HSA, leading to changes in the chemical shifts and intensities of ^{13}C-OA HC-HSQC cross-peaks (16).

HSA also supports the remodeling of functional tissues. For instance, the rise of the local concentration of HSA accelerates bone healing (1). HSA bone growth elevation is associated with stem cells recruitment (1, 17), since the population of stem cells attached to the surface of the demineralized bone increases in the presence of albumin. The interaction between stem cells and HSA may be investigated through ^{13}C-OA assay and competitive binding with ^{13}C-OA. Hence, the HSA therapeutic potential in regenerative medicine might be better understood by considering allostery and competitive binding.

5.1.3- Applications of CONFA to Map Interactions with Endogenous HSA Ligands

HSA transports essential metal ions such as Cu^{2+} and Zn^{2+}. Zinc is necessary for enzymatic activity and transcription factors (18, 19). Free fatty acid concentrations are elevated in some conditions, including diabetes, cancer, obesity, and pregnancy (18). Under physiological conditions, free fatty acid fluctuations affects the affinities of HSA for other ligand, such as metals (18). Therefore, the concentration of free fatty acid modifies zinc's distribution (18, 19). The ^{13}C-OA assay could identify or at least narrow down the binding sites of endogenous or exogenous ligands and probe HSA conformational changes upon binding to these ligands.

5.1.4- Applications of CONFA to Monitor HSA Modifications

HSA modifications are related to some disease conditions. For example, misfolded albumin is associated with AD (20). Upon albumin misfolding, phospholipid degradation increases in fluid bilayer membranes, and HSA concentration in cerebrospinal fluid (CSF) decreases. In addition, the fatty acid binding capacity of CSF albumin is decreased in a female AD group (20), suggesting that the pre-bound fatty acid may prevent further fatty acid binding, since fatty acid binding cause allosteric conformational changes that change albumin's binding capacity (20). The effect of pre-bound fatty acids can be tested through CONFA and ^{13}C-OA assays. Also, ischemia-modified albumin (IMA) rises in myocardial ischemia (MI) (21). It has recently been shown that the high IMA in MI is the consequence of high levels of free fatty acids in plasma (21). This indicates that modifications of albumin correlates with fatty acid binding and could be investigated by the ^{13}C-OA assay. Moreover, in some conditions such as hepatocellular carcinoma, nephrosis, and cardiovascular diseases, the HSA concentration increases, and such increase correlates with high fibrinogen levels involved in the hemostatic system (22). Since CONFA is only minimally dependent of the HSA concentration, it may assist the accurate quantification of long chain fatty acid that bind to HSA even under these pathological conditions. So, the CONFA approach emerges as a method with significant diagnostic and therapeutic relevance.

5.1.5- Applications of CONFA in Metabolomics

HSA and free fatty acids are central to metabolomic studies as well. Although metabolomics studies mostly rely on fatty acid extraction and mass spectrometry methods such as MSI-NACE-MS (23) or GC-MS (24), in some cases, ^{13}C-OA assays may be utilized as a complementary experiment for metabolomic data analysis and interpretation. For instance, changes in albumin concentration in response to pathological conditions, such as inflammation, affects the concentration of free fatty acids in plasma and fecal fatty acid concentration (25). The CONFA method could be used to investigate the correlation between free fatty acid concentration in plasma and fecal short-chain fatty acids. In general, gives its large abundance in plasma, serves as a repository that binds several blood metabolites that may remain hidden in traditional metabolomic extraction-based studies. The CONFA approach may assist the characterisation of this otherwise 'dark' plasma metabolome. In summary, HSA plays multiple physiological, pathological, and pharmacological roles, and allostery is critical for such functions (2). The CONFA and ^{13}C-OA assays are useful to probe the HSA's interactions underlying the numerous functions of HSA. The CONFA applications can range from control experiments in metabolomic data analyses to quantification of binding of ligands, from metal ions to drugs, or proteins such as αS.

5.2 Non-canonical Kinase Activation by Polymerization of Inhibitory Proteins: Significance and Future Studies

Chapters three and four of this thesis address a long-outstanding question in the field of disease-related mutants of Protein Kinase A (PKA). Inherited mutations in one of the most ubiquitous isoforms of the PKA regulatory subunit (R1α) are known to cause a generalized cancer predisposition, which is referred to as Carney Complex (or CNC in short). The molecular phenotype of CNC mutants is typically over-activation of PKA. For several CNC-related mutations, the over-activation of PKA is rationalized in terms of mRNA nonsense-mediated decay (NMD) and R1α haploinsufficiency. However, some of the most harmful CNC mutants, such PKA R1α A211D and G287W, escape NMD and still result in losses of PKA inhibition. Explaining PKA overactivation for these CNC mutations in the context of the classical cAMP-dependent activation of PKA is challenging. These CNC mutants exhibit reduced affinity for cAMP compared to wt, while their affinity for the C-subunit does not change significantly, leading to a stable and poorly cAMP-sensitive inhibited holoenzyme.

Here, we have proposed a simple but viable solution for this CNC paradox. We propose the hypothesis that CNC mutations cause partial unfolding and self-association of R1α in assemblies that are incompetent to inhibit the C-subunit of PKA. We tested this hypothesis through the comparative analysis of structure, unfolding, aggregation and kinase inhibition for wt, two PKA R1α CNC mutants (A211D and G287W) as well as their cognate acrodysostosis type 1 mutants (A211T and G287E). The latter are known to exhibit a molecular phenotype of reduced PKA activation, *i.e.* opposite of CNC, and therefore serve as internal controls in our experimental design. Our comparative analyses relied on an extensive set of integrated experimental techniques to probe PKA R1α at different length scales and resolutions, including intrinsic and extrinsic fluorescence, HDX NMR, SEC, DLS, TEM and kinase assays.

Through our multidisciplinary approach, we surprisingly find that the PKA CNC mutations investigated here induce the formation of inhibition incompetent R1α polymers to a significantly higher extent compared to their counterpart acrodysostosis type 1 mutants. This unexpected finding not only offers a simple but effective mechanism of action to explain the overactivation CNC phenotype, but it also defines a previously unanticipated non-classical activation pathway for PKA, which is clearly distinct from the classical cAMP-dependent PKA activation. Our data reveal that the non-classical activation of PKA by R1α polymerization occurs for wt R1α as well, albeit to a reduced extent compared to the CNC mutants, and provide an unprecedented view of the key homotypic interfaces that drive the self-assembly of R1α into open-ended agglomerates. We could show that there is significant overlap between the R1α sites that drive self-association and those necessary for inhibition of the PKA C-subunit, thus explaining why R1α polymers are inhibition incompetent. The far-reaching implication of these findings is that PKA regulation should be revisited in light of R1α polymerization, which not only explains CNC etiology but also modulates the classical cAMP-dependent activation of PKA. Furthermore, the novelty of this contribution is that it integrates concepts from PKA signaling and amyloid formation, two fields that have traditionally evolved quite separately but that in this thesis converge.

5.3 References

1. D. B. Horváthy, *et al.*, Serum albumin as a local therapeutic agent in cell therapy and tissue engineering. *BioFactors* **43**, 315–330 (2017).
2. B. VanSchouwen, G. Melacini, Cracking the allosteric code of NMR chemical shifts. *Proc. Natl. Acad. Sci.* **113**, 9407–9409 (2016).
3. A. Poursoleiman, *et al.*, Polymyxins interaction to the human serum albumin: A thermodynamic and computational study. *Spectrochim. Acta Part A Mol. Biomol. Spectrosc.* **217**, 155–163 (2019).
4. S. Boulton, *et al.*, Mechanisms of specific versus nonspecific interactions of aggregation-prone inhibitors and attenuators. *J. Med. Chem.* **62**, 5063–5079 (2019).
5. J. Wu, Z. Wang, W. Lin, S. Chen, Investigation of the interaction between poly (ethylene glycol) and protein molecules using low field nuclear magnetic resonance. *Acta Biomater.* **9**, 6414–6420 (2013).
6. S. Tenzer, *et al.*, Rapid formation of plasma protein corona critically affects nanoparticle pathophysiology. *Nat. Nanotechnol.* **8**, 772–781 (2013).
7. M. Chen, *et al.*, Investigating the Interaction of Nanodiamonds with Human Serum Albumin and Induced Cytotoxicity. *J. Spectrosc.* **2019** (2019).
8. R. Ahmed, G. Melacini, A solution NMR toolset to probe the molecular mechanisms of amyloid inhibitors. *Chem. Commun.* **54**, 4644–4652 (2018).
9. M. Algamal, *et al.*, Atomic-resolution map of the interactions between an amyloid inhibitor protein and amyloid β (Aβ) peptides in the monomer and protofibril states. *J. Biol. Chem.* **292**, 17158–17168 (2017).
10. M. Algamal, J. Milojevic, N. Jafari, W. Zhang, G. Melacini, Mapping the Interactions between the Alzheimer's Aβ-peptide and human serum albumin beyond domain resolution. *Biophys. J.* **105**, 1700–1709 (2013).
11. J. Milojevic, A. Raditsis, G. Melacini, Human serum albumin inhibits Aβ fibrillization through a "monomer-competitor" mechanism. *Biophys. J.* **97**, 2585–2594 (2009).
12. J. Milojevic, V. Esposito, R. Das, G. Melacini, Analysis and parametric optimization of 1H off-resonance relaxation NMR experiments designed to map polypeptide self-recognition and other noncovalent interactions. *J. Phys. Chem. B* **110**, 20664–20670 (2006).
13. J. Milojevic, M. Costa, A. M. Ortiz, J. I. Jorquera, G. Melacini, In vitro amyloid-β binding and inhibition of amyloid-β self-association by therapeutic albumin. *J. Alzheimer's Dis.* **38**, 753–765 (2014).
14. J. Milojevic, G. Melacini, Stoichiometry and affinity of the human serum albumin-Alzheimer's Aβ peptide interactions. *Biophys. J.* **100**, 183–192 (2011).

15. B. VanSchouwen, R. Ahmed, J. Milojevic, G. Melacini, Functional dynamics in cyclic nucleotide signaling and amyloid inhibition. *Biochim. Biophys. Acta (BBA)-Proteins Proteomics* **1865**, 1529–1543 (2017).

16. R. Ahmed, *et al.*, Molecular Mechanism for the Suppression of Alpha Synuclein Membrane Toxicity by an Unconventional Extracellular Chaperone. *J. Am. Chem. Soc.* (2020).

17. D. B. Horváthy, *et al.*, Serum albumin-coated bone allograft (BoneAlbumin) results in fasterboneformationandmechanicallystrongerboneinagingrats (2019).

18. S. Al-Harthi, J. I. Lachowicz, M. E. Nowakowski, M. Jaremko, Ł. Jaremko, Towards the functional high-resolution coordination chemistry of blood plasma human serum albumin. *J. Inorg. Biochem.* **198**, 110716 (2019).

19. S. Al-Harthi, Investigation of Zinc Interactions to Human Serum Albumin and Their Modulation by Fatty Acids (2019).

20. F. H. C. Tsao, J. N. Barnes, A. Amessoudji, Z. Li, K. C. Meyer, Aging-Related and Gender Specific Albumin Misfolding in Alzheimer's Disease. *J. Alzheimer's Dis. Reports* **4**, 67–77 (2020).

21. J. P. C. Coverdale, *et al.*, Ischemia-modified albumin: Crosstalk between fatty acid and cobalt binding. *Prostaglandins, Leukot. Essent. Fat. Acids* **135**, 147–157 (2018).

22. D. Chen, *et al.*, Two-step separation-free quantitative detection of HSA and FIB in human blood plasma by a pentaphenylpyyrrole derivative with aggregation-enhanced emission properties. *Sensors Actuators B Chem.* **255**, 854–861 (2018).

23. S. Azab, R. Ly, P. Britz-McKibbin, Robust Method for High-Throughput Screening of Fatty Acids by Multisegment Injection-Nonaqueous Capillary Electrophoresis–Mass Spectrometry with Stringent Quality Control. *Anal. Chem.* **91**, 2329–2336 (2018).

24. N. Wellington, *et al.*, Metabolic trajectories following contrasting prudent and western diets from food provisions: identifying robust biomarkers of short-term changes in habitual diet. *Nutrients* **11**, 2407 (2019).

25. L. D. N. Marcon, L. F. S. Moraes, B. C. S. Cruz, M. D. O. Teixeira, A. F. F. Gomides, Yacon (Smallanthus Sonchifolius)-Based Product Increases Fecal Short-Chain Fatty Acids Concentration and Up-Regulates T-Bet Expression in the Colon of BALB/c Mice During Colorectal Carcinogenesis. *J Food Sci Nutr* **6**, 69 (2020).